

**UNIVERSITÀ DEGLI STUDI DI NAPOLI
FEDERICO II**



Dottorato di Ricerca in Ingegneria Industriale
XXXI Ciclo

**Experiments and Simulations of Hybrid
Rocket Internal Flows and Material
Behaviour**

Coordinatore:
Prof. Michele Grassi

Tutor:
Prof. Raffaele Savino

Co-tutor:
Dott. Carmine Carmicino

Candidato:
Ing. Di Martino Giuseppe
Daniele

TABLE OF CONTENTS

Table of Contents.....	I
List of Figures.....	V
List of Tables.....	IX
Abstract.....	X
CHAPTER 1. Hybrid Rocket Propulsion: state of the art	1
1.1 Introduction to hybrid rocket engines.....	1
1.1.1 Advantages of hybrid rockets	2
1.1.2 Historical perspective and potential applications of hybrid rocket propulsion technology.....	4
1.2 Hybrid rocket combustion mechanism	7
1.2.1 The model of Marxman and Gilbert	7
1.2.2 Combustion of liquefying fuels.....	9
1.3 CFD modelling of hybrid rocket internal ballistics	11
1.4 Summary of original contributions of the present dissertation on hybrid rocket internal ballistics modelling.....	13
CHAPTER 2. Low erosion materials for propulsion application.....	15
2.1 Rocket nozzle operating conditions.....	15
2.2 Materials for rocket nozzle applications.....	17
2.3 The C ³ HARME research project for development and testing of UHTCMC materials.....	19
2.4 Summary of the contributions of the present dissertation on advanced materials for propulsion application	21
CHAPTER 3. Experimental setup and firing test cases.....	23

3.1	Experimental facilities	23
3.1.1	The lab-scale motors	23
3.1.2	Feeding line.....	25
3.1.3	Signal measurements and data acquisition system	26
3.2	Firing data reduction technique	28
3.3	Experimental firing test	30
3.3.1	Test cases with polymeric fuels	30
3.3.2	Test cases with paraffin-based fuel grain.....	34
CHAPTER 4. Modelling of hybrid rockets internal ballistics.....		36
4.1	Introduction to the definition of the numerical model for hybrid rockets simulation.....	36
4.2	Physical and numerical models for gaseous flowfield simulation.....	37
4.2.1	Turbulence model	38
4.2.2	Combustion model.....	40
4.2.3	Thermodynamic and transport properties	42
4.3	Computational domain and boundary conditions	43
4.4	Gas/fuel surface interface modelling	44
4.4.1	The case of polymeric fuels	45
4.4.2	The case of liquefying fuels	49
4.5	Port diameter update with time for the transient simulation of the fuel grain consumption.....	53
CHAPTER 5. Numerical results of hybrid rockets internal ballistics simulation		55
5.1	Numerical results in the case of polymeric fuels.....	55
5.1.1	Steady simulations	55
5.1.2	Grid sensitivity analysis	60
5.1.3	Transient simulation.....	62

5.2	Numerical results in the case of liquefying fuels.....	69
5.2.1	Effect of the additional entrainment regression rate component ..	69
5.2.2	Grid sensitivity analysis	73
5.2.3	Effect of vaporization temperature and entrainment parameter ...	75
5.2.4	Comparison between numerical results and experimental data	78
CHAPTER 6. Characterization of UHTCMC in hybrid rocket propulsion environment		81
6.1	Design of prototypes and experimental setup.....	81
6.1.1	Experimental setup for free-jet test.....	81
6.1.2	Setup for test of nozzle throat inserts.....	83
6.2	Numerical models for the characterization of the flowfield around test articles.....	84
6.2.1	One-dimensional model for chamber and nozzle conditions simulation.....	85
6.2.2	CFD model for the simulation of the flow field around test articles	86
6.3	Experimental characterization of UHTCMC samples in free jet conditions	89
6.3.1	UHTCMC samples.....	89
6.3.2	Test conditions	90
6.3.3	Experimental results.....	94
6.4	Experimental characterization of UHTCMC nozzle throat insert	102
6.4.1	UHTCMC samples.....	102
6.4.2	Test conditions	103
6.4.3	Experimental results.....	105
Conclusions.....		109

Table of Contents

Acknowledgments	111
Bibliography	112

LIST OF FIGURES

Figure 1.1. Schematic of classical hybrid rocket engine.	1
Figure 1.2. Boundary layer combustion mechanism for hybrid rockets.....	8
Figure 1.3. Liquid layer instability and droplet entrainment mechanism (Ref. [28]).	10
Figure 2.1. Molar fractions of the combustion products in rockets with different propellants [44].	16
Figure 2.2. (a) Segmented nozzle (after removal of the converging outer element), (b) ceramic throat, (c) details of the ceramic throat showing radial cracks [45].	19
Figure 2.3. Design of the test articles for C ³ HARME experimental campaign for characterization of UHTCMCs in propulsion application [59].	20
Figure 3.1. 200 N-class hybrid rocket engine schematic.	23
Figure 3.2. 1 kN-class hybrid rocket engine layout.	25
Figure 3.3. Test feeding lines schematic.....	26
Figure 3.4. Tescom ER3000 pressure controller scheme.	26
Figure 3.5. Rocket exhaust plume (Test HDPE-1).	31
Figure 3.6. Sequence of pictures of the hybrid rocket exhaust nozzle after the firing test (Test HDPE-1).	31
Figure 3.7. Operating pressures vs time.	32
Figure 3.8. Rocket exhaust plume (Test P-4)	35
Figure 4.1. An example of the computational grid for the 200 N-class engine.....	44
Figure 4.2. Schematic representation of the i-th node displacement components.....	54
Figure 5.1. Results of the steady-state numerical simulation in the case of Test HDPE-1.	56
Figure 5.2. Results of the steady-state numerical simulation in the case of Test ABS-1.	57
Figure 5.3. Regression rate distributions evolution in the firing with the axial-nozzle injector.	59
Figure 5.4. Numerical regression rate profiles calculated with different refined computational grids (Test HDPE-1).	61

Figure 5.5. Temperature contour plot with overlapped streamlines (top half) and mixture fractions isolines (bottom half) at different times.	64
Figure 5.6. Regression rate distributions evolution in the firing test.....	65
Figure 5.7. Fuel-grain port local diameter evolution in the firing test.....	66
Figure 5.8. Comparison between the measured and calculated local regression rate for Test HDPE-2.....	68
Figure 5.9. Comparison between the results with and without considering the entrainment.	70
Figure 5.10 Numerical results in the case of paraffin fuel.....	72
Figure 5.11. Numerical results in the case of HDPE fuel.....	73
Figure 5.12. Numerical error versus grid size.	74
Figure 5.13. Effect of the vaporization temperature on the axial profiles of the regression rate and its components.	76
Figure 5.14. Effect of the entrainment parameter on the axial profiles of the regression rate and its components.....	77
Figure 5.15. Regression rate axial profile (Test 4): comparison between numerical results and experimental data.....	78
Figure 5.16. Comparison between numerical results and experimental data in terms of average regression rate as a function of the oxidizer mass flux.	80
Figure 6.1. Nominal design of UHTCMC samples for free jet tests. Dimensions are in mm.	82
Figure 6.2. Set-up for free-jet test. The area within the red circle in the left picture is zoomed in the right picture.	82
Figure 6.3. Design of segmented nozzle with UHTCMC nozzle throat insert. Dimensions are in mm.	84
Figure 6.4. Computational grid for the simulation of the free reacting jet exiting from the rocket nozzle.	88
Figure 6.5. Computational grid for the simulation of the flow through the rocket nozzle.	89
Figure 6.6. Temperature distribution in the free-jet test.	92
Figure 6.7. O ₂ mass fraction distributions in the free jet tests.	93

Figure 6.8. Erosion rates of UHTCMC samples in free jet test: comparison between Ti_3SiC_2 based samples and ZrB_2/SiC based samples.....	94
Figure 6.9. Pictures of sample TSC-SF-1 before (top) and after (bottom) the test. ..	95
Figure 6.10. Pictures of sample ZBSC-LF-1 before (top) and after (bottom) the test.	96
Figure 6.11. Pictures of sample TSC-SF-2 after the test.	96
Figure 6.12. Pictures of sample ZBSC-LF-2 after the test.	96
Figure 6.13. Thermal histories of the samples TSC-SF-1 and ZBSC-LF-1 tested in Test condition 1FJ.....	97
Figure 6.14. Pictures of test on TSC-SF-1 sample, at beginning (left) and end (right) of the test (Test Condition 1FJ).	98
Figure 6.15. Pictures of test on ZBSC-LF-1 sample, at beginning (left) and end (right) of the test (Test Condition 1FJ).	98
Figure 6.16. IR thermal images of TSC-SF-1 sample, taken every 0.5 s, starting from immediately before the temperature jump.	99
Figure 6.17. Temperature radial profiles, measured by the thermo-camera, on sample TSC-SF-1 front surface at different time instants, around the temperature jump.	99
Figure 6.18. Thermal histories of the TSC-SF-2 and ZBSC-LF-2 samples tested in Test condition 2FJ.....	100
Figure 6.19. Thermographic images of sample ZBSC-LF-2.	100
Figure 6.20. Erosion rates of UHTCMC samples in free jet test: comparison between short-fibers-based and long-fibers-based samples.	101
Figure 6.21. Thermal histories of the ZBSC-LF-2 and ZBSC-SF-1 samples tested in Test condition 2FJ.....	102
Figure 6.22. Temperature distribution through rocket nozzle.	105
Figure 6.23. O_2 mass fraction distributions through rocket nozzle.	105
Figure 6.24. Nozzle throat erosion rates.	106
Figure 6.25. Microscopic pictures of graphite nozzle throat.	107
Figure 6.26. Microscopic pictures of ZBSC-SF-TI.	107
Figure 6.27. Microscopic pictures of ZBSC-LF-TI.	107

Figure 6.28. Theoretical and measured chamber pressures vs operating time for tests
in conditions 2TI..... 108

LIST OF TABLES

Table 2.1. Solid and hybrid rocket nozzle operating conditions [44].	15
Table 3.1. Experimental data of firing test cases with polymeric fuels.	33
Table 3.2. Experimental data of firing test cases with paraffin-based fuel grains performed with the 200 N-class hybrid rocket.	34
Table 4.1. Values of SST model constants [67].	40
Table 4.2. Computational domain dimensions.	44
Table 4.3. Solid fuels properties and rate constants.	47
Table 4.4. Paraffin fuel properties.	50
Table 5.1. Computed average pressure in the aft-mixing chamber and deviation with experimental data.	60
Table 5.2. Results of grid sensitivity analysis on the spatially averaged regression rate.	62
Table 5.3. Computed averaged parameters and deviation with respect to experimental data.	67
Table 5.4. Results of grid sensitivity analysis on the spatially averaged regression rate components.	74
Table 5.5. Vaporization temperature and entrainment parameter effect on the average regression rate.	77
Table 5.6. Computed regression rate deviations from experimental data.	80
Table 6.1. C ₂ H ₄ – O ₂ reaction system.	87
Table 6.2. UHTCMC samples for free jet test.	90
Table 6.3. Nominal test conditions for free jet tests.	90
Table 6.4. Conditions at sample location estimated with the CFD simulations of the free-jet test.	91
Table 6.5. UHTCMC nozzle throat inserts.	103
Table 6.6. Nominal test conditions throat insert testing.	103
Table 6.7. Conditions at nozzle throat estimated with the CFD simulations.	104

ABSTRACT

In the last decade a significant and ever growing interest has been addressed towards hybrid rocket propulsion, which offers the best-of-both-worlds by leveraging the favourable aspect of both traditional solid and liquid systems. Among the numerous advantages which characterize hybrid rockets, the most attractive ones are the re-ignition and throttling capabilities combined with the possibility of embedding environmentally sustainable propellants and, of the utmost importance, their intrinsic safety and lower operational costs. Moreover, hybrid rockets yield a better specific impulse than solid propellant rockets and a higher density impulse than liquids, which make them a promising technology in a number of space missions.

The widely recognized potentialities of the hybrid rocket warrant the renewed research efforts that are being devoted to its development, but the state-of-the-art of this technology still presents a number of challenging issues to be solved.

A first fundamental task is the definition of suitable models for the prediction of the motor internal ballistics and performance. In particular, rocket performance is governed by the rate at which the fuel is gasified, i.e. by the fuel regression rate, as this latter determines the total mass flow rate and the overall oxidizer-to-fuel mixture ratio, which, for a given chamber pressure, control the motor thrust and the ideal specific impulse. For a given fuel, regression rate is basically limited by the heat flux input to the solid grain, which mainly depends on the thermo-fluid-dynamics in the combustion chamber. This latter is significantly influenced by several geometrical parameters, such as, for example, the oxidizer injection configuration or the grain port shape. Furthermore, the recent efforts aimed at overcoming the main drawback of the hybrid rockets, which is the low regression rate of conventional polymeric fuels, have been focused on the development of new paraffin-based fuels, characterized by a consumption mechanism presenting additional complex phenomena compared to that of conventional polymers. Their intrinsic characteristic is the onset of a thin liquid layer on the fuel grain surface, which may become unstable, leading to the lift-off and entrainment of fuel liquid droplets into the main gas stream, increasing the fuel mass

transfer rate. This phenomenon is strongly susceptible to the fuel composition, its manufacturing process and the obtained thermo-mechanical properties as well as to the engine operating conditions, which makes the prediction of the regression rate and combustion chamber internal ballistics even harder than in the case of a pure polymer. In this framework, computational fluid dynamics of hybrid rocket internal ballistics is becoming a key tool for reducing the engine operation uncertainties and development cost, but its application still presents numerous challenges due to the complexity of modelling the phenomena involved in the fuel consumption mechanism and the interaction with the reacting flowfield, for both the cases of classical polymeric and liquefying paraffin-based fuels. A research effort is therefore of major importance in order to cover the lacking aspects and obtain quantitatively accurate results.

Another challenge for the hybrid rocket technology development is the optimization of the design of thermal insulations. The inner surface of the exhaust nozzle, through which the flow is accelerated to supersonic conditions producing the required thrust, is the most critical in this sense, as it is subjected to the highest shear stress and heat fluxes in a chemically aggressive environment. These severe conditions usually lead to removal of surface material due to heterogeneous reactions between oxidizing species in the hot gas and the solid wall. Because of the material erosion, there is an enlargement of the nozzle throat section and a consequent decrease of rocket thrust, with detrimental effects over the motor operation. Thus, the requirement that dimensional stability of the nozzle throat should be maintained makes the selection of suitable rocket nozzle materials extremely hard. In recent years, Ultra-High-Temperature Ceramics (UHTC) and Ultra-High-Temperature Ceramic Matrix Composites are the subject of considerable interest as innovative materials for rocket application, but still need to be properly characterized. Experimental testing along with computational fluid dynamic (CFD) simulations are, thus, both needed to improve the design and the current performance prediction capabilities of such propulsion systems. In this framework, the University of Naples is involved in the European project C³HARME – Next Generation Ceramic Composites for Combustion Harsh Environment and Space, in collaboration with other research centres, universities and

industries, which aims at the design, manufacturing and testing of new-class high-performance UHTCMC for near-zero erosion rocket nozzles.

In the present work, the above-mentioned challenges are dealt with taking a combined experimental/numerical approach to improve understanding of the interaction between the gaseous combusting flow typical of hybrid rocket engines and the surface of solid materials involved in their operation, with a special focus to the fuel grain present in the combustion chamber, with the aim of predicting its consumption mechanism, and the exhaust nozzle inner surface, with the aim of identifying and validating new-class UHTCMC materials with improved erosion and structural resistance to the severe conditions experienced in particular in the throat region.

In particular, the first main objective of the present work is the definition of proper computational thermo-fluid-dynamic models of the hybrid rocket internal ballistics, including a dedicated gas/surface interface treatment based on local mass, energy and mean mixture fraction balances as well as proper turbulence boundary conditions, which can properly model the physical fuel consumption mechanism in both the cases of polymeric and liquefying fuels. For the validation of the computational models, a number of experimental test cases, obtained from static firing of laboratory scale rockets, have been performed at the Aerospace Propulsion Laboratory of University of Naples “Federico II” and successively numerically reconstructed. The comparison between the numerical results and the corresponding experimental data allowed validating the adopted model and identifying possible future improvements.

Then, the research activities for the characterization of new-class UHTCMC materials are presented and discussed. This part of the work was mainly focused on an extensive experimental campaign for the characterization of new-class UHTCMC materials. In particular, first preliminary tests on small samples exposed to the supersonic exhaust jet of a 200N-class hybrid rocket operated with gaseous oxygen burning cylindrical port High-Density PolyEthylene (HDPE) fuel grains have been carried out for a fast characterization and a preliminary screening of the best candidates for the final applications. After that UHTCMC nozzle throat inserts has been manufactured and experimentally tested to verify the erosion resistance and evaluate

the effects on the rocket performance by comparison with those obtained in similar operating conditions employing a graphite nozzle. The experimental activities are supported by simplified low-computational-cost numerical simulations, whose main objectives has been the prediction of the complex flow field in the hybrid rocket combustion chamber and the thermo-fluid dynamic conditions on the material. Future research activities will be then focused to the further development of the numerical models with the extension of the treatment for the gaseous flow/solid surface interaction in order to get a deeper insight on the new materials behaviour.

CHAPTER 1. HYBRID ROCKET PROPULSION: STATE OF THE ART

1.1 Introduction to hybrid rocket engines

Hybrid rockets are chemical propulsion engines whose concept has been known since the early 20th century [1], in which fuel and oxidizer are separated in different physical states. In the classical system configuration (see Figure 1.1), hybrid rockets usually accommodate a prechamber ahead of the fuel grain, and an aft-mixing chamber, downstream of it; fuel is stored in the combustion chamber in the solid state, and a liquid or gaseous oxidizer is injected into one or multiple ports obtained in the solid fuel grain. The latter is usually made by simple classical polymers, such as high density polyethylene (HDPE), hydroxyl-terminated polybutadiene (HTPB), and polymethylmethacrylate (PMMA), polymers with metal additives to improve the density impulse, or, more recently, paraffin waxes.

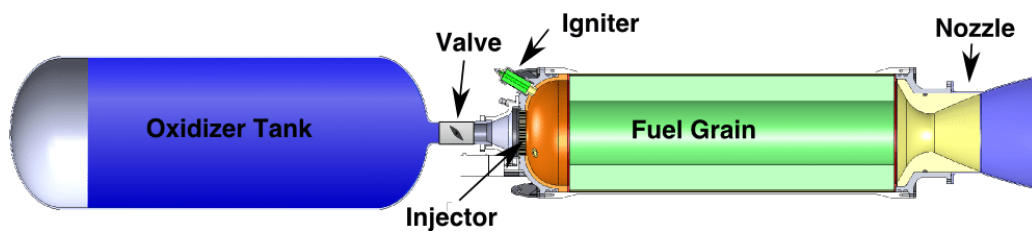


Figure 1.1. Schematic of classical hybrid rocket engine.

When the two propellants are ignited, a diffusive flame is formed in the boundary layer developing in the grain port, relatively far from the fuel surface, and it is fed, from the outer side, by the oxidizer, which is transported from the free stream by turbulent diffusion mechanisms, and, from the inner side, by the products of fuel pyrolysis that is sustained by the flame itself; the combusted mixture then expands through an exhaust nozzle generating the required thrust.

Performance of these engines is governed by the rate at which the fuel is gasified, i.e. by the fuel regression rate \dot{r} , as this latter determines the total mass flow rate and overall oxidizer-to-fuel mixture ratio OF , which, for a given chamber pressure, control the motor thrust and the ideal specific impulse I_{sp} .

1.1.1 Advantages of hybrid rockets

In the last decade a significant and ever growing interest has been addressed towards hybrid rocket propulsion thanks to its numerous advantages [2] compared to traditional solid and liquid systems.

1.1.1.1 Safety

The primary reason for interest in hybrid is the non-explosive nature of the design, which lead to safety in both operation and manufacture [3, 4]. In fact, in liquid bipropellant rockets, a pump leak or tank rupture can bring the oxidizer and the fuel together in an uncontrolled way resulting in a large explosion, while, in solid propellant rockets, the fuel and oxidizer are already mixed and held together in a polymer binder, so that cracks or imperfections can cause uncontrolled combustion and explosion. In hybrid propellant rockets the fuel and oxidizer are intimately separated and the design is less susceptible to chemical explosion. The fuel can be fabricated at any conventional commercial site, realizing a large cost saving.

1.1.1.2 Re-ignition and throttling capability

One of the critical issues of solid fuel rockets is the impossibility of shut down and re-ignition, i.e. once the engine is ignited there is no possibility to control or to stop the ignition, until the fuel grain is completely burned. On the contrary hybrid rocket engines can be throttled by modulating the oxidizer flow rate, to optimize the trajectory during atmospheric launch and orbit injection, and thrust termination/restart is simply accomplished by turning off and on the oxidizer flow rate.

With respect to liquid bipropellant rockets, hybrid rockets require one rather than two liquid containment and delivery systems, reducing the complexity and improving the reliability of the system. Throttling control is simpler because it alleviates the

requirement to match the momenta of the dual propellant streams during the throttling operation.

1.1.1.3 Environmental sustainability

Oxidizers and fuels used in hybrid rocket engines produce usually less threat to health and environmental safety. For example Hydrazine and its derivatives, which are widely used as propellants in liquid rockets, are highly corrosive, toxic and carcinogens.

The products of combustion in hybrid rockets are environmentally benign compared with conventional solids that generally use perchlorate-based oxidizers. In fact, solid rocket combustion products contain acid-forming gases such as hydrogen chloride (HCl). In addition, there are concerns about the effects of low levels of environmental perchlorate.

1.1.1.4 Theoretical specific and density impulse

Hybrid rockets yield a higher specific impulse than solid propellant rockets. In fact, the theoretical specific impulse of a hybrid rocket is more appropriately compared to a bipropellant liquid than a solid. This is because the oxidizers are the same and the solid fuels are hydrocarbons with energy content similar to kerosene.

However, hybrid solid fuel density are typically 15-20% greater than the density of liquid kerosene, so hybrid rockets yields higher density impulse than liquids. Furthermore, the fact that the fuel is in the solid phase makes it very easy to add performance-modifying materials. For example, the addition of aluminium powder produces a substantial increase in fuel density, increases the theoretical I_{sp} and shifts the peak I_{sp} to lower values of the oxidizer-to-fuel ratio. This leads to a reduced liquid feed system and tank size, producing better performance.

In conclusion, the above discussed features make hybrid engines a promising technology in a number of space missions, opening to safer and more flexible space vehicle launching and manoeuvring [5, 6, 7].

1.1.2 Historical perspective and potential applications of hybrid rocket propulsion technology

The hybrid rocket concept has been around for more than eighty years. The first liquid propellant rocket launched by the Soviet Union was actually a hybrid that used liquid oxygen (LOX) and gelled gasoline. The rocket was designed by Mikhail Tikhonravov in 1933 and built by a team from the Group for the Study of Reaction Motors (GRID) that was headed by the famous Sergei Korolev. The first flight reached an altitude of 1500 m using a 500 N class motor that burned for 15 s.

The earliest effort in the U.S. occurred at the Pacific Rocket Society and at General Electric, beginning in the late 1940s and continuing up to 1956. But early hybrid rocket development began in earnest when flight test programs were initiated both in Europe and in the U.S. in the 1960s. European programs in France and in Sweden involved small sounding rockets, whereas the American flight programs, largely sponsored by the U.S. Military Force, were target drones that required supersonic flight in the upper atmosphere for up to 5 minutes. Furthermore, in the late 1960s the small size hybrid rockets started to be scaled to large size motors by the Chemical Systems Division of United Technologies, which investigated motor designs that could produce the high thrust required for space launch vehicles. Anyway, although several successful firings were performed during those years, it was recognized that the volumetric fuel loading efficiency was too low mainly because of the low regression rate.

Interest in the hybrid was revived again in the late 1970s, when concerns aroused about safety storage and handling of the large solid propellant segments of the Shuttle booster. Then, beginning in the late 1980s, two significant hybrid efforts occurred. One was the formation of the American Rocket Company (AMROC), an entrepreneurial industrial company entirely devoted to the development of large hybrid boosters based on LOX and HTPB. The second, with encouragement from NASA, was the formation of the Hybrid Propulsion Industry Action Group (HPIAG), composed of both system and propulsion companies devoted to exploring the possible use of hybrids for launch booster applications. Again, both efforts ran into technical stumbling blocks, caused by the low regression rate of HTPB fuel.

Several hybrid propulsion programs were initiated also in the late 1980s and in the 1990s. The most remarkable one was the Hybrid Propulsion Demonstration Program (HPDP), whose main objective was the design and fabrication of a 250000 lb thrust test bed.

The most successful flight of a hybrid rocket occurred in 2004 when the reusable manned spaceplane SpaceShipOne reached an altitude of 100 km for the second time in a 1-week period, using a four-port HTPB fuelled motor and nitrous oxide (N₂O) oxidizer.

Throughout this history, the fundamental issue of low regression rate inherent in polymeric fuels was the main drawback for the hybrid rocket development, but it was clear that if a significantly higher burning rate could be realized for the hybrid motor, the difficulties mentioned above could be greatly reduced and a smaller, more efficient motor could be designed. This deficiency was recognized early on, and many attempts were made to increase the regression rate.

In particular, the research activities carried out at Stanford University, beginning in 1997, led in the mid-2000s to the development of a class of liquefying fuels, including paraffin-based fuels, characterized by very high regression rate, ensuring good performance at low cost, availability, low environmental impact. These results renewed the interest in hybrid rocket technology as a promising propulsive solution for important innovative missions.

Several market studies, starting from early 2000 allowed performing trade-off analyses for the identification of the most suitable space/aerospace application for hybrid rockets, with a particular interest in the framework of mass access to space. Four main markets can be identified for such technology, each one with different requirements in terms of performance and cost, which are listed in the following.

- *Sub-orbital flight vehicles* can be seen as the first enabling building block. In particular, large growth potential for *space tourism* as a business concept (Ref. [8, 9]) suggests the need for improvement in propulsion technologies, which would reduce the service price. Therefore, strategies for space propulsion cost reduction rely essentially on two approaches. The first approach is based on the use of lower cost and higher performance rocket engines, like hybrid rocket

engines. The second approach involves the use of innovative high performance fuels, such as paraffin-based fuels. The interest of hybrid rocket applications in sub-orbital systems is increasing in both commercial and public funded projects. Commercial vehicles include Virgin Galactic SpaceShipTwo, Copenhagen Suborbitals Tycho Brahe and Whittinghill Aerospace mCLS: these are or will be powered by hybrid rocket motors [10].

- *Launch vehicles upper stages* could represent an effective market entrance of hybrid propulsion system, since this application is characterized by relatively low barrier and several potential advantages would derive from hybrid technology. An example of public effort in this direction involves the HYPROGEO EU-Funded project in the Horizon 2020 framework, related to the development of an hybrid rocket for launch vehicles upper stages, under the leadership of Airbus Defence and Space SAS.
- *Nano/microsatellite launch vehicles*. Considering the 2013 nano/ microsatellite launch services report [11], it is possible to assume that nano/microsatellites launch is a growing market. Furthermore, the historical analysis suggests that the current launch vehicle capacity will not be able to satisfy the future demand, in particular considering the increasing number of requests for micro/nanosatellites. In order to exploit the increase in market demand, it will be of great importance to put in place specific strategies. In this scenario, hybrid launch vehicles for small payloads can be effectively developed using the knowledge established with sub-orbital applications. This is an important step in the direction of overcoming the historical perspective of nano/microsatellites as secondary payload only. The advantages of such dedicated launch systems are: low cost, flexibility, low environmental impact and orbit/time specificity.
- *Launch vehicles lower stages/boosters*. The application of hybrid rocket motors to launch vehicles lower stages and boosters is the most challenging scenario. Lower launch vehicles stages are characterized by very high thrust (magnitude order of several MN), required to reach escape velocity and lift-off of the launch vehicle. This extreme performance level requires a very large system. In such geometries, scale-up combustion phenomena can occur, which

can significantly affect the engine behaviour. Low-scale to large-scale effects involve combustion stability, fuel grain mechanical resistance and non-homogeneous fuel consumption issues.

1.2 Hybrid rocket combustion mechanism

One of the fundamental problem in the design of a hybrid rocket is to accurately predict the fuel regression-rate, as a function of time and position along the surface of grain, since, as mentioned before, this is the main parameter governing the engine performance. Of course, this problem can be addressed only by a proper modelling of the hybrid rocket internal ballistics, which depend on different complex and interacting physical phenomena, on the engine configuration and on the fuel and oxidizer physical nature.

Many theories have been developed over the years in order to describe the hybrid combustion mechanism, but often they lack some important aspects or failed in the prediction of experimental results [12, 13, 14].

1.2.1 The model of Marxman and Gilbert

The most reliable hybrid combustion model for classical polymeric fuels was developed in 1963 by Marxman and Gilbert [15, 16] and it is still the starting point of design calculations and experimental comparisons. This model is based on the concept of diffusion flame, anticipated before, according to which the combustion reaction occurs in a thin region inside the developing boundary layer through diffusive mixing between vaporized oxidizer flowing through the port and fuel evaporating from the solid surface. Thus, the flame zone can be considered as temperature and mixture composition discontinuity (see Figure 1.2). Typically the chemical kinetics in the reaction zone are much faster than the relatively slow diffusion processes which provides the fuel and the oxidizer to the flame, thus the flame is said to be diffusion-limited.

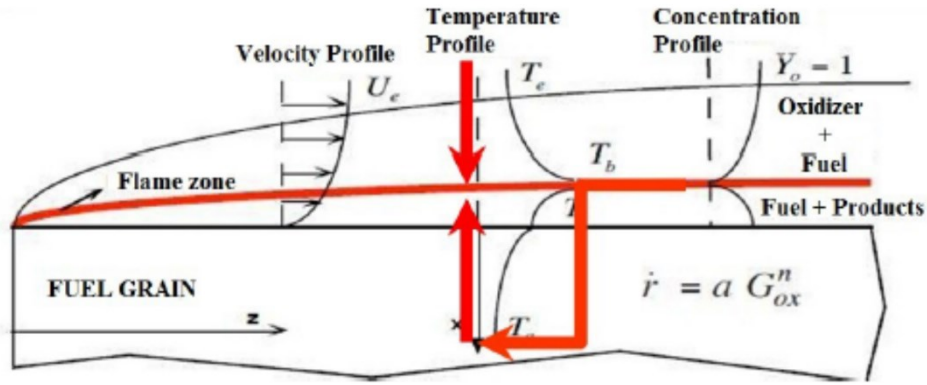


Figure 1.2. Boundary layer combustion mechanism for hybrid rockets.

According to this model, the fuel regression rate is proportional to the wall heat flux as

$$\rho_f \dot{r} = (\rho v)_w = \frac{\dot{q}_w}{h_v} \quad (1.1)$$

where ρ_f is the solid fuel density, $(\rho v)_w$ is the gaseous mass flux at the fuel wall, \dot{q}_w is the heat flux to the wall and h_v is the effective fuel vaporization heat, i.e. the energy per unit mass needed to evaporate fuel from the initial solid fuel temperature.

Considering the simpler configuration of a uniform oxidizer flow on a solid fuel slab, assuming unit Lewis and Prandtl numbers and applying the Reynolds analogy, the previous equation can be manipulated obtaining the following relationship between the fuel regression rate and the total axial mass flux G

$$\rho_f \dot{r} = 0.036 G Re_x^{-0.2} B^{0.23} \quad (1.2)$$

where $Re_x = Gx/\mu$ is the local Reynolds number and B is the so called blowing factor.

More generally, in order to overcome the slab fuel configuration hypothesis and the further complexity due to the total mass flux dependence on the regression rate itself, the regression rate law is simply expressed in the form

$$\dot{r} = aG_{ox}^n \quad (1.3)$$

where G_{ox} is the oxidizer mass flux in the fuel grain port and a and n are constant mainly depending on the propellants and on the system configuration and are usually determined experimentally. Eq. (1.3) represents the fact that, in marked contrast to solid rockets, the regression rate of a hybrid is insensitive to the chamber pressure, while, because of the diffusion-limited nature of the combustion process, it is primarily governed by turbulent mixing and heat transfer in the boundary layer, which in turn depend on the mass flux.

1.2.2 Combustion of liquefying fuels

As described in the previous section, fuel regression of classical polymers is determined by the ratio between the heat flux to the surface and the heat of phase change, thus it is limited by the heat and mass transfer mechanisms occurring from the flame to the fuel wall; blowing of fuel from the surface decreases the velocity gradient at the wall and the convective heat transfer for the so-called blocking effect [15]. Owing to this “counter-balance” between heat flux and blowing, hybrid rocket motors operating with polymeric fuels usually suffer from the problems associated with low regression rate, which hinder the widespread application of such propulsion systems.

Several strategies have been suggested to mitigate this shortcoming, such as, among the most common ones, the design of multi-port grains for which, despite the slow regression, a high thrust level can be obtained; the design of injection systems inducing recirculating [17, 18] or swirling oxidizer flows [19, 20]; and the addition of metal additives or solid particles, which mostly raise the density impulse with a minor effectiveness on the regression rate [21]. Yet, all of these methods lead to an increase of the system complexity and associated cost without producing major improvements of the engine overall performance [22].

Researchers at Stanford University [23] have demonstrated that a much more effective method for enhancing regression rate is to use propellants that form a melt layer at the combustion surface. These are usually non-polymerized substances that liquefy on heating. An obvious class includes liquids or gases at standard conditions,

which are frozen to form solids (that is, solid cryogenic hybrids). However it is clear that the same internal ballistic behaviour can be experienced by materials that are solids at standard conditions if they form a melt layer at the combustion surface. Paraffin-based fuels belong to the latter class [24].

Compared to conventional polymers, the consumption mechanism of this class of fuels, known as liquefying fuels, is basically different and allows for significantly larger regression rate. Karabeyoglu et al. [23] have shown that these fuels display, indeed, regression rates up to 3-4 times higher than those achieved with traditional hybrid fuels. Referring to Figure 1.3, their intrinsic characteristic is the onset of a thin liquid layer on the fuel grain surface, which may become unstable. In fact, due to the low viscosity and surface tension, it is affected by a hydrodynamic instability of the Kelvin-Helmholtz type [25, 26] driven by the oxidizer flow injection, which leads to the lift-off and entrainment of fuel liquid droplets into the main gas stream, increasing the fuel mass transfer rate. This characteristic behaviour has been experimentally investigated showing the formation of roll waves and droplets in the tests carried out at atmospheric pressure, and filament-like structures along the fuel grain in the tests run at elevated pressures [27].

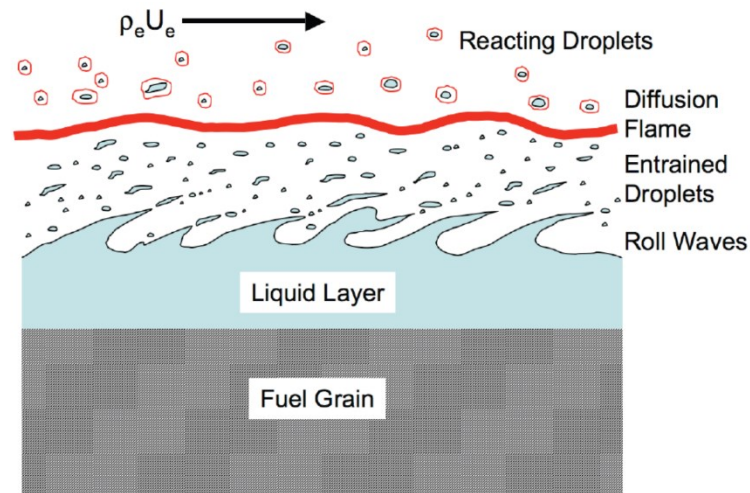


Figure 1.3. Liquid layer instability and droplet entrainment mechanism (Ref. [28]).

This mass transfer mechanism does not depend on heat transfer and raises the fuel mass flow without entailing the blocking effect determined by gaseous fuel blowing. As a result, the overall regression rate can be considered composed by two fractions, one determined by classical fuel vaporization, and the other by the liquid entrainment. The entrainment phenomenon is strongly susceptible to the fuel composition, its manufacturing process and the obtained thermo-mechanical properties as well as to the engine operating conditions [29], which makes the prediction of the combustion chamber internal ballistics even harder. Hence, on the one hand, designers need to characterize the fuel with extended experimental campaigns and, on the other, carry out rocket static firings to measure the achieved engine performance.

1.3 CFD modelling of hybrid rocket internal ballistics

Affordable and reliable computational models, capable to simulate the thermo-fluid-dynamic field in the rocket combustion chamber, are the subject of considerable interest recently, as they are aimed to become an efficient tool both in the system design process and in the performance analysis stage for reducing the engine operation uncertainties and development cost.

In fact, the classical theories, starting from Marxman's work described in Section 1.2.1, elaborated to predict the regression rate of pyrolyzing fuels, are all based on the assumption of a turbulent boundary layer with chemical reactions occurring in the burning of a fuel slab in an oxidant gas flow and, therefore, are unable to reproduce the oxidizer injection effects, which may have a non-negligible impact even in standard motors [17]. The analytical models subsequently developed for liquefying fuels, such as the one in Ref. [23], are essentially modifications of the classical hybrid boundary-layer combustion theory for the entrainment mass transfer from the fuel grain, and consequently present the same limits as the original theory.

In this context, computational fluid dynamic (CFD) approaches to the solution of flowfield in the hybrid propellant rocket chamber have been considerably developed

recently [30, 31, 32]; most of the effort has been addressed to classical non-liquefying fuels, which, however, involve numerous complexities due, for example, to the interactions among fluid dynamics, oxidizer atomization and vaporization, mixing and combustion in the gas phase [19], nozzle thermochemical erosion [33], particulate formation, and radiative characteristics of the flame [34].

A common strategy is solving the Reynolds Averaged Navier-Stokes (RANS) equations, with suitable turbulence closure and combustion models. In particular, justified by the fact that chemical and fluid dynamic characteristic times are much shorter than the regression rate time scale, steady-state solution of RANS equations is generally sought [35]. An acceptable method to study the hybrid rocket internal ballistics can be, therefore, simulating the flowfield at different times in the motor firing by considering the fuel port geometry evolution [36]. Nevertheless, a single numerical simulation is often performed on the chamber geometry drawn at the time-space averaged port diameter [36, 37]. To the authors' knowledge, in the competent literature, even when analyses have been performed at several stages of the motor firing, the grain inner diameter has been always considered uniform down the port; in other words, the axial non-uniformity of the regression rate has been usually neglected and the port diameter has been updated with a spatially-averaged regression rate value.

Moreover, the definition of a suitable and computational cost-effective strategy for liquefying fuels poses further complications related to the modeling of the melting layer dynamics and of the liquid entrainment phenomenon. In principle, to successfully simulate the paraffin-fuel consumption, two non-trivial tasks have to be accomplished, that are modeling, first, the melted fuel entrainment from the grain surface, and, second, the transformation of the melted fuel into gaseous species participating in the combustion process. These demanding efforts have probably discouraged researchers, so that usually drastic simplifications are introduced, such as giving the regression rate calculation away by assuming it from experiments [38, 39], or limiting the analysis to one-dimensional integro-differential models [40]. In other cases, observing that under the hybrid rocket chamber characteristic conditions the melted paraffin wax is in the supercritical state (thus surface tension vanishes and the sharp distinction at droplets surface between gas and liquid phases disappear), the melted layer brake up and

subsequent liquid paraffin injection in the flowfield is disregarded, supposing that the entrainment is part of the turbulent mixing process [41]. However, in general, all the existing models are not successfully validated displaying still significant deviations from experimental data, which in some cases are around 25%. Hence, a research effort is definitely of major importance in order to obtain quantitatively accurate results.

1.4 Summary of original contributions of the present dissertation on hybrid rocket internal ballistics modelling

In the research activities described in the present dissertation, a combined experimental/numerical effort has been spent for a better understanding of the consumption mechanism of fuel grains of different classes. The main objectives is the definition, the application and the validation, by comparison with specifically collected experimental data, of dedicated CFD models for the simulation of the thermo-fluid dynamic flow field inside the combustion chamber of hybrid rockets.

In particular, the work started from the definition of a simplified model apt to simulate the thermo-fluid-dynamic field in a hybrid rocket, in which however fuel regression rate was imposed decoupled from the actual flow field. The main purpose was to have a relatively fast tool to qualitatively analyse the effect of different parameters on the regression rate axial profile and to screen several oxidizer injectors based on the resulting motor performance. The results of such model are described in Ref. [42].

The CFD model has been successively elaborated in order to obtain quantitatively predictive capabilities also on the local regression rate of classical polymeric fuels, and on the corresponding chamber pressure, combustion efficiency and rocket performance. For this purpose, an improved treatment of the interface between the gaseous flow and the solid fuel surface has been defined, which is based on local mass, energy and species balances, with the application of proper turbulence boundary conditions and considering an additional equation for the fuel surface pyrolysis. Such

a model has been applied to perform both steady and transient numerical simulation, by numerically integrating the calculated local regression rate and updating the fuel port shape during the engine run to capture the post-burn fuel axial consumption profile. With the aim of completely validating the computational model, different experimental firings have been performed at the Aerospace Propulsion Laboratory of University of Naples (UNINA), with gaseous oxygen as oxidizer and either HDPE or Acrylonitrile-Butadiene-Styrene (ABS) fuel grains. They have been then numerically reconstructed and the measured data have been compared with the corresponding computational results showing a very good agreement.

Finally, the last step was the extension of the CFD model for the simulation of the internal ballistics of hybrid rocket burning paraffin fuel grains and the estimation, also in this case, of the regression rate profile. For this purpose, the gas/fuel surface interface treatment has been properly modified including in this case an additional equation for the calculation of the regression rate component determined by the entrainment of liquid droplets into the main flow. The model has been then applied to study the effects of the fuel properties on the regression rate, and in particular of the fuel vaporization temperature, which has a major impact on the heat flux to the wall, and of the liquid paraffin viscosity, which instead influences the liquid layer stability and the droplets entrainment. Finally, also in this case the numerical model has been applied to the reconstruction of a series of data obtained from static firings of the 200-N class hybrid rocket available at UNINA Aerospace Propulsion Laboratory, burning paraffin-based fuel grains with gaseous oxygen. This allowed validating the adopted model and identifying possible future improvements.

CHAPTER 2. LOW EROSION MATERIALS FOR PROPULSION APPLICATION

2.1 Rocket nozzle operating conditions

The thermal, chemical, and mechanical environments typical of aero-propulsion applications introduce many problems from the point of view of materials. In particular, the inner surface of high performance rocket nozzles, where the propellant flow is accelerated to supersonic conditions, is typically subjected to very high shear stresses and heat fluxes and high pressure in a chemically aggressive environment [43]. Table 2.1 summarizes typical operating conditions and design ranges encountered in solid and hybrid rocket chamber and nozzle [44].

Table 2.1. Solid and hybrid rocket nozzle operating conditions [44].

	Range SRM	Range HYBRID
Pressure (bar)	50-100	5-25
Combustion time (s)	70-150	>10
Throat diameter (m)	0.1-1	0.1-0.2
Throat flame temperature (K)	≈3000 K	≈3000 K
Throat heat flux (MW/m ²)	5 - 30	5 - 15

The values of the throat flame temperature, the operating pressure and throat heat flux are important parameters to identify the operating conditions in which the material must operate.

For the typical propulsion applications the maximum value of operative temperature refers to the flame temperature, while the range of the operative pressure refers to the typical values of propulsive applications for hybrid and solid rocket motors. Furthermore, due to the fast gas expansion through the nozzle, gas pressure and temperature decreases quickly along the nozzle insert profile. This effect generates asymmetric pressure loads and surface temperature higher than 2000 K on the internal

surface, leading to high thermal gradients towards the inner material regions especially if the thermal conductivity of the material is small.

The accelerating flow through the nozzles produces strong shear stresses and heat fluxes, which assume maximum values at the throat section. The throat heat flux values reported in Table 2.1 are representative of the extreme operating conditions for the nozzles.

Moreover, nozzles for rocket applications typically operate in chemically aggressive environments. For instance, Figure 2.1 shows the typical chemical compositions of the combustion chamber of hybrid and solid rockets in representative operating conditions.

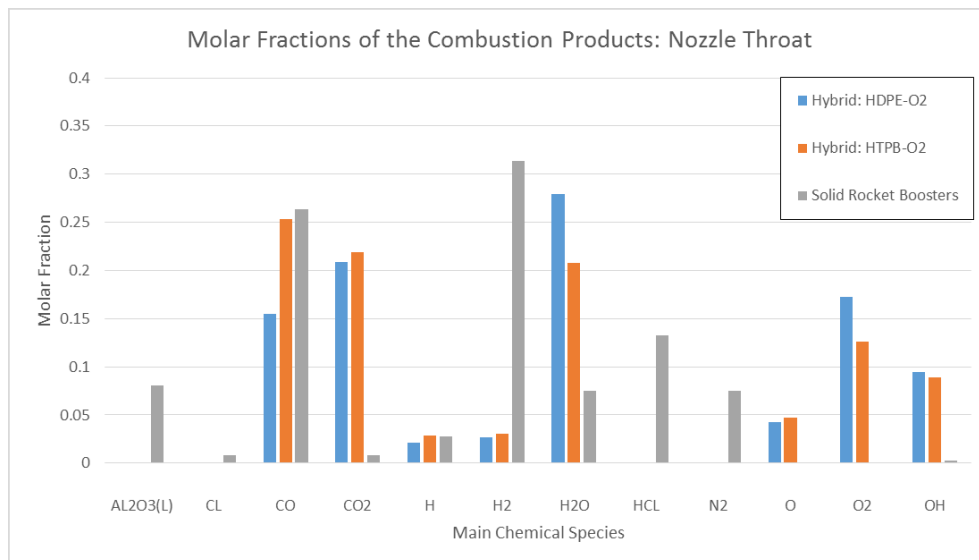


Figure 2.1. Molar fractions of the combustion products in rockets with different propellants [44].

In particular, for the hybrid rockets, two cases have been analyzed, considering Oxygen as oxidizer and a HDPE fuel grain in one case and a HTPB fuel grain in the other one. In the first case, the average Oxidizer to Fuel ratio considered is equal to 4, while in the second case the average OF considered is equal to 3.2: these values are well representative of the operating condition of the 200N-class Hybrid Rocket Motor available at the UNINA Aerospace Propulsion Laboratory. From the figure it can be noticed that in these cases the chemical environment is characterized by the presence

of significant concentration of oxygen and other oxidizing species. On the other side, for solid rockets, the typical propellant composition used for the boosters of the launcher Ariane V has been analyzed. In this case, although the oxidizing species are present in smaller concentrations, they are enough to induce thermochemical erosion of nozzle throat materials. Moreover the environment is characterized by the presence of condensed phase, such as liquid particles of Al_2O_3 , which can lead to a further mechanical erosion of the inner nozzle surface.

These severe conditions usually lead to removal of surface material, due to heterogeneous reactions between oxidizing species in the hot gas and the solid wall [45], which could be significant also in relatively short single operation determining detrimental effects on the rocket performance. In fact, for rocket converging-diverging nozzle the mass balance equation leads to the following relationship

$$\dot{m}_{ox} \left(1 + \frac{1}{OF} \right) = \frac{p_c A_t}{\eta c^*} \quad (2.1)$$

in which p_c is the chamber pressure, A_t is the nozzle throat area, c^* is the theoretical characteristic exhaust velocity (that primarily depends on the mixture ratio and, to a minor degree, on pressure) and η is the combustion efficiency. Therefore, for a fixed propellant mass flow rate and mixture ratio, the chamber pressure inversely depends on the nozzle throat area. Consequently, an increase of the throat section diameter due to the nozzle material erosion causes a decrease of the chamber pressure and, then, of the motor thrust.

Thus, the requirement that dimensional stability of the nozzle throat should be maintained guaranteeing a stable engine operation makes the selection of rocket nozzle materials extremely challenging.

2.2 Materials for rocket nozzle applications

The classical materials used for these applications include refractory metals, refractory metal carbides, graphite, ceramics and fiber-reinforced plastics [46, 47].

Certain classes of materials demonstrated superior performances under specific operating conditions but the choice depends on the specific application. For instance, fully densified refractory-metal nozzles generally are more resistant to erosion and thermal-stress cracking than the other materials. Graphite performs well with the least oxidizing propellant but is generally eroded severely [48, 49, 50]. Some of the refractory-metal carbide nozzles show outstanding erosion resistance, comparable to that of the best refractory-metal materials, but generally suffer due to fractures induced by thermal stresses.

In recent years, Ultra-High-Temperature Ceramic (UHTC) materials, including zirconium or hafnium diborides or carbides, are assuming an increasing importance because of their high temperature capabilities. They are characterized by unique combination of properties, including melting points above 3500 K, high temperature strength, capability to manage and conduct heat when the service temperatures exceed 2200 K. Anyway, it has been proven that the use of single phase materials, without secondary phases, is not sufficient for extreme applications because these materials are characterized by low fracture toughness, low thermal shock resistance and lack of damage tolerance, therefore they are unacceptable for aerospace engineering applications [51, 52, 53].

For example, in Ref. [45] a Tantalum Carbide (TaC)-based nozzle throat insert was manufactured and tested in the lab scaled hybrid rocket at the UNINA Aerospace Propulsion Laboratory. Although no erosion occurred in the throat, the outer surface remained unchanged after the test and no visible chemical alteration was observed, radial cracks were detected, as shown in Figure 2.2, which demonstrated the fragility of this UHTC material.

To improve the behaviour, bulk UHTCs composites with SiC or other Silicon based ceramics, in the form of particles, short fibers and whiskers have been developed with better tolerance and thermal shock resistance in aggressive chemical environments [54, 55]. Unfortunately, despite the very good oxidation resistance of small specimens, larger UHTC components frequently exhibited poor reliability and were subject to failures in high enthalpy flows.

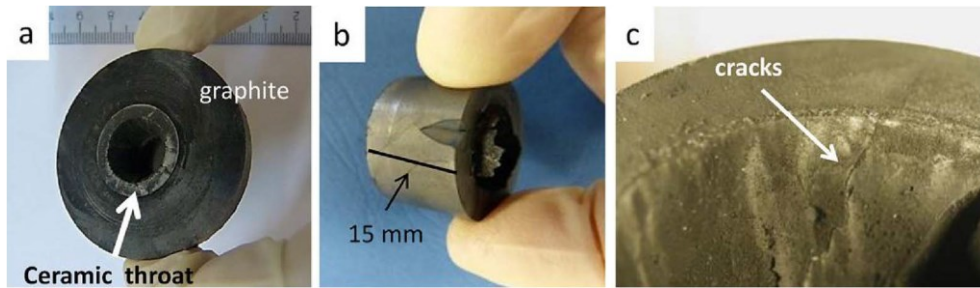


Figure 2.2. (a) Segmented nozzle (after removal of the converging outer element), (b) ceramic throat, (c) details of the ceramic throat showing radial cracks [45].

Based on these results, the current research activities are oriented towards Ultra-High-Temperature Ceramic Matrix Composites (UHTCMC) materials based on C or SiC continuous fibers in UHTC matrices, which can be expected to show good erosion resistance properties compared to C/C and C/SiC composites, as well as good thermal shock resistance and damage tolerance [56, 57, 58] and then to be the potential candidates for use in propulsion applications.

2.3 The C³HARME research project for development and testing of UHTCMC materials

In the framework of Horizon 2020, University of Naples “Federico II” is involved in C³HARME research project, whose main purpose is the design, development, manufacturing and testing of a new class of UHTCMCs suitable for application in severe aerospace environments. The project will bring the Proof-of-Concept of these new materials into two main applications:

- Near zero-erosion nozzle inserts that can maintain dimensional stability during firing in combustion chambers of high performance rockets for civil aerospace propulsion.
- Near zero-ablation thermal protection systems (tiles) able to resist the very high heat fluxes in strongly reactive gases and thermo-mechanical stresses found at launch and re-entry into Earth’s atmosphere.

In the present dissertation, the focus will be given to the first application.

The project foresees a 4-year plan of research activities, aimed at introducing innovative material solutions with high performances and optimizing standard processing techniques in order to manufacture final products suitable for space applications.

The project relies on the integration of extensive existing experience with both UHTCs and CMCs (ceramic matrix composites). Well-established techniques for CMC production will be integrated with state-of-art methods for the hot consolidation of ultra-refractory ceramics.

In the framework of the project, UNINA contributed to the definition of the requirements and is responsible for the prototypes design and the identification of the corresponding testing conditions. An incremental approach has been used for this task, proposing to start the experimental campaign with simple material samples and increasing the complexity up to a Technology Readiness Level (TRL) 6, as shown in Figure 2.3.

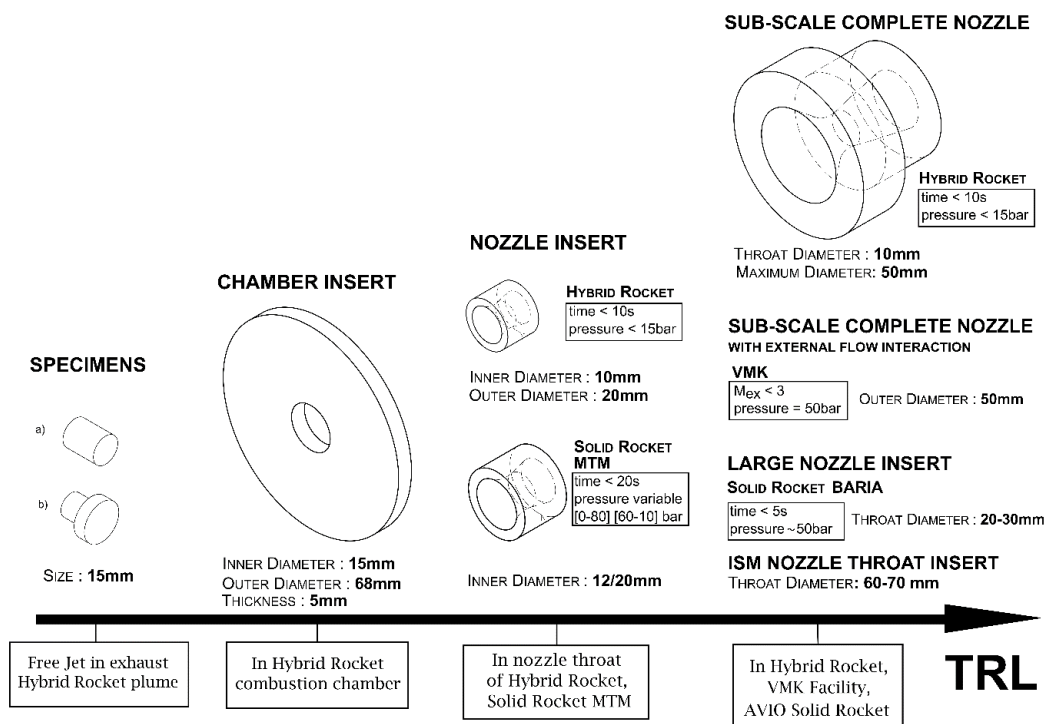


Figure 2.3. Design of the test articles for C³HARME experimental campaign for characterization of UHTCMCs in propulsion application [59].

A preliminary experimental campaign will be carried out with specimen and prototypes characterized by simple geometry and small dimensions to screen the behavior of different material compositions and select the most interesting ones. After the identification of possible materials, the prototypes with greater dimensions and complex shape will be fabricated and tested in order to achieve the final product design and the best manufacturing processes. The experimental activities for this application will be carried out in UNINA test facilities, the AVIO laboratory and DLR (German Aerospace Research Center) facilities.

2.4 Summary of the contributions of the present dissertation on advanced materials for propulsion application

A combined experimental/numerical approach, similar to that described in Section 1.4 for the fuel grain consumption mechanism characterization, has been adopted also in this framework of nozzle material characterization, giving in this case a major effort to the experimental activities. Therefore, in the present dissertation, the results of the first experimental tests for the characterization of new UHTCMC materials for application in hybrid rockets, carried out at UNINA Aerospace Propulsion Laboratory in the framework of C³HARME research project, will be presented.

In particular, the first tests have been performed with a novel, dedicated test set-up exposing UHTCMC samples to the supersonic exhaust jet of a 200 N-class hybrid rocket operated with gaseous oxygen burning cylindrical port HDPE. Non-intrusive diagnostic equipment, including two-colour pyrometers and an infrared thermo-camera, has been employed to monitor the surface temperature of the samples. The combination of combustion temperature over 3000 K, supersonic Mach number and stagnation pressures allowed reproducing realistic rocket nozzles operating conditions, in order to demonstrate the ability of the specimens to preserve their functional integrity in a relevant environment.

After that UHTCMC nozzle throat inserts has been manufactured and experimentally tested to verify the erosion resistance and evaluate the effects on the rocket performance by comparison with those obtained in similar operating conditions employing a graphite nozzle.

The experimental activities are supported by numerical simulations able to predict the complex flow field in the hybrid rocket combustion chamber and the thermo-fluid dynamic conditions on the material. A simplified model has been adopted in this phase with the aim of getting relatively rapidly more information not experimentally measurable about the test conditions. Anyway the development of the model for the study of the interaction between the reacting fast-accelerating flow and the materials, extending the strategy developed for the fuel grain regression rate prediction, will be the subject of future research activities.

CHAPTER 3. EXPERIMENTAL SETUP AND FIRING TEST CASES

3.1 Experimental facilities

The experimental activities described in this work have been carried out at the Aerospace Propulsion Laboratory of University of Naples “Federico II”, located in the Military Airport “F. Baracca” of Grazzanise (CE, Italy).

The test rig is a versatile set up primarily designed for testing hybrid rocket engines of several sizes [60]. It is equipped with a test bench and a general-purpose acquisition system, which allow evaluating propellant performance and combustion stability [61], testing of sub-components and/or complete power systems, nozzles [62], air intakes, catalytic devices [63], burners, ignition and cooling systems [45, 64]. As it will be discussed in detail in Section 6.1, the experimental setup can be adjusted also for testing of material in harsh combusting environment for propulsion applications.

3.1.1 The lab-scale motors

Several rocket demonstrators of different scales are available for testing at the Laboratory. The experimental firings that will be presented in this work have been performed mainly with a 200 N-class hybrid rocket whose schematic is depicted in Figure 3.1.

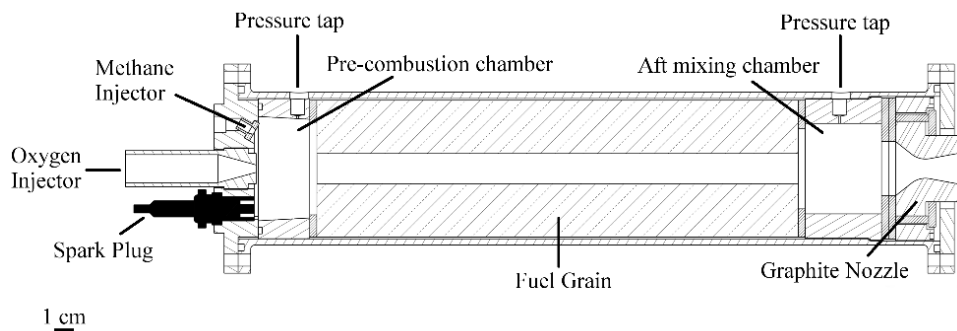


Figure 3.1. 200 N-class hybrid rocket engine schematic.

The lab rocket engine has an axisymmetric combustion chamber, with 350 mm length and 69 mm case inner diameter.

The motor forward closure can accommodate different injectors; the tests presented in the following sections have been performed with a converging nozzle injector, whose exit section diameter is 6 mm, which delivered oxygen in single-port cylindrical fuel grains.

Upstream and downstream of the solid grain a dump plenum and an aft-mixing chamber are set up. The pre-chamber, which is 25 mm long with a 46 mm inner diameter, shifts the broad oxidizer recirculation towards the fore end of the grain, in order to increase the overall regression rate. The post-chamber is usually required in hybrids to promote gas mixing at the exit of the fuel port, thereby improving combustion efficiency. Aft-mixing chamber with either 38 mm or 58 mm length can be employed with the aim of testing fuel grains of either 240 mm or 220 mm length, respectively.

The engine has two pressure taps for static pressure measurements in the pre- and in the post-chamber.

A graphite converging-diverging exhaust nozzle is usually employed. The modular design of the engine allows the use of nozzles with different throat diameter and area ratio. Moreover, the graphite nozzle can be easily replaced by segmented nozzles with throat insert or by complete nozzles made of new high performance materials to test their erosion behaviour and structural and thermal resistance for this kind of applications, as it will be discussed in more detail in CHAPTER 6.

A spark plug powered by a Honeywell solid-state igniter spark generator is arranged in the pre-chamber where methane gas is injected for 3 seconds simultaneously with the oxygen to ignite the motor. This system ensures repeatable ignition conditions as well as motor re-ignition.

In addition to the firings performed with the subscale engine presented above, some firing test have been performed on a larger scale, 1 kN-class hybrid rocket available at the lab, whose schematic is depicted in Figure 3.2.

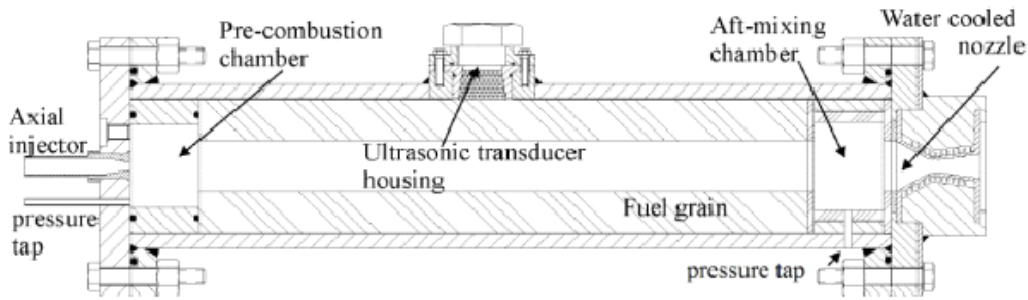


Figure 3.2. 1 kN-class hybrid rocket engine layout.

The engine design is conceptually similar to the design of the subscale engine. The combustion chamber is axisymmetric as well; it is 720 mm long and has a 133 mm inner case diameter. Similarly to the small-scale engine, a converging nozzle injector, with 8 mm diameter exit-section, has been employed, and ahead and aft of the fuel grain two chambers were set up.

Also in this case two pressure taps for pressure measurements in the pre-chamber and in the aft-mixing chamber are set up. Furthermore, in this case near the middle of the engine case is present an opening which can house an ultrasonic transducer for the measurement of the time-resolved local grain thickness and fuel regression rate.

A water-cooled, converging–diverging nozzle with a 16-mm throat diameter, 2.44 area ratio, made of a copper alloy ensures long duration firings without throat erosion.

3.1.2 Feeding line

A schematic of the oxidizer feeding line is depicted in Figure 3.3.

Gaseous oxygen is supplied by a reservoir of 4 pressurized tanks connected to the motor feed line. The feeding pressure is then set by means of the TESCOM ER3000 electronically controlled pressure valve (see Figure 3.4), which regulates an electro-pneumatic valve in order to reduce the pressure to the desired set point. The control is performed on the basis of the pressure signal measured by a transducer located downstream the regulator. The presence of a choked Venturi tube before the injector ensures that the set feeding pressure is directly proportional to the desired oxygen mass flow rate. The same device allows the evaluation of the latter parameter through gas temperature and pressure measurements upstream of the throat section.

An additional line is present for nitrogen purging into the chamber for the burn out and in case of an accident

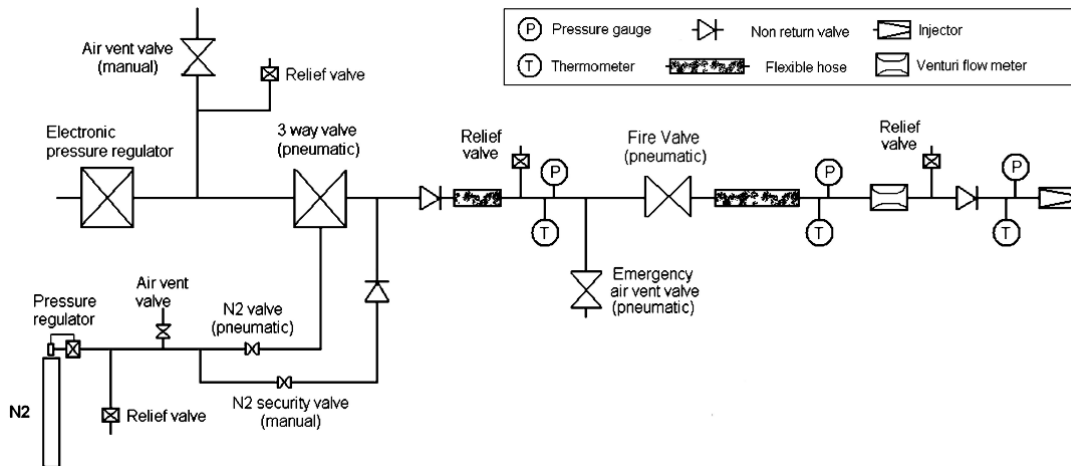


Figure 3.3. Test feeding lines schematic.

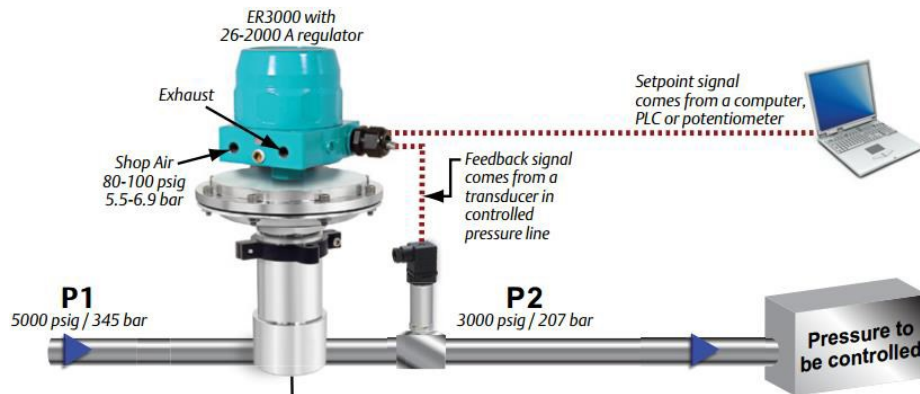


Figure 3.4. Tescom ER3000 pressure controller scheme.

3.1.3 Signal measurements and data acquisition system

Several sensors are present for the measurement of significant quantities during experimental test, which are listed in the following.

- Three capacitive pressure transducers and three thermocouples are located along the feeding line and at the section upstream of the oxidizer injector for the

measurement (and monitoring for safety reasons) of the feeding pressure and of the temperature.

- As above mentioned, a choked Venturi tube is located upstream the oxidizer injector; a pressure transducer and a thermocouple allow the measurement of the pressure and the temperature upstream its throat section for the evaluation of the oxidizer mass flow rate.
- Two pressure transducers are assembled on proper pressure taps present on the rocket for the measurement of the pressure in the pre-chamber and in the aft-mixing chamber during engine operation.
- Four load cells assembled on the test bench allow evaluating the motor thrust by computing the sum of the loads measured with each cell.

The analogue signals generated by thermocouples, pressure transducers and load cells are sampled at 5 kHz, digitally converted, processed and recorded on the hard disk by a National Instruments (NI) PXI Express standard system interconnected with the computer by means of optic fiber connections. With this equipment and using a software developed in LabView, the motor is ignited and the firing test is completely automated. All the signals are stored in a binary format and, after downsampling the data to 100 Hz with a boxcar average, in text format for post-processing.

As mentioned before, for the 1 kN-class hybrid rocket it is possible to employ an ultrasonic transducer set up near the middle of the chamber to measure the time-resolved local grain thickness and fuel regression rate by means of the ultrasound pulse-echo technique, explained in detail in Ref. [61]. The transducer is a Panametrics Videoscan V114-SB of $\frac{3}{4}$ in nominal diameter and 1 MHz central frequency. The waves emitted by the transducer are generated, received and amplified by a pulser/receiver unit (Panametrics model 5072PR) with 1 kHz pulse repetition frequency.

Finally, digital two-colour pyrometers and an infrared thermo-camera are available for non-intrusive monitoring of surface temperature in the case of characterization testing on materials for propulsion applications, as it will be described in more detail in Section 6.1.

3.2 Firing data reduction technique

The main parameters directly measured in the firing tests are the oxidizer mass flow rate \dot{m}_{ox} , the chamber pressure p_c , the motor thrust Th , the fuel grain mass consumption ΔM and the burning time t_b . The remaining quantities of interest can be derived from the measured ones. From the fuel grain mass loss and the operation time, the average fuel mass flow rate can be calculated as

$$\bar{\dot{m}}_f = \frac{\Delta M}{t_b} \quad (3.1)$$

and consequently the average oxidizer-to-fuel ratio can be evaluated as

$$\overline{O/F} = \frac{\dot{m}_{ox}}{\bar{\dot{m}}_f} \quad (3.2)$$

The space-averaged final port diameter can be calculated from the fuel mass loss as

$$\tilde{D}_2 = \sqrt{D_1^2 + \frac{4 \Delta M}{\pi \rho_f L}} \quad (3.3)$$

where D_1 and L are the grain initial diameter and length, respectively. The time-space-averaged port diameter can be then evaluated as

$$\bar{D} = \frac{D_1 + \tilde{D}_2}{2} \quad (3.4)$$

and the average oxidizer mass flux can be calculated as

$$\bar{G}_{ox} = \frac{4\dot{m}_{ox}}{\pi \bar{D}^2} \quad (3.5)$$

The time-space-averaged fuel regression rate can be evaluated as

$$\bar{r} = \frac{\tilde{D}_2 - D_1}{2t_b} \quad (3.6)$$

Finally, the combustion efficiency is calculated as the ratio

$$\eta = \frac{c^*}{c_{th}^*} \quad (3.7)$$

in which c^* is the characteristic exhaust velocity estimated with the measured values of pressure, total mass flow rate and nozzle throat area as

$$c^* = \frac{pA_t}{\dot{m}} \quad (3.8)$$

and c_{th}^* is the theoretical exhaust characteristic velocity, obtained in adiabatic chemical equilibrium conditions at the measured overall mixture ratio and chamber pressure, with the CEA code [65].

The main factors of uncertainty involving the measured quantities are the determination of the burning duration (i.e. the time interval between the inflection point on the pressure rise branch at the motor start up and the one on the pressure drop at the burnout); the dispersion of the grain port initial diameter measurements, and, of course, on a lesser degree, the scale sensitivity for the measurement of the initial and final grain masses, and the signals oscillation during the test in the measurement of the oxidizer mass flow rate. For the details of the uncertainty assessment procedure refer to [21].

Besides the average quantities evaluated as described before, also the axial profiles of the fuel grain consumption and the corresponding time-averaged local regression rate profiles have been measured. In particular, experimental data are obtained by sectioning the fuel grain transversally in a number of slices, and measuring the port diameter by means of a caliper; in each transversal section, the minimum, maximum

and the average of eight diameter measurements have been recorded. The corresponding local regression rate has been then obtained with Eq. (3.6).

3.3 Experimental firing test

In this section, the results of several firing tests carried out at the Aerospace Propulsion Laboratory described in the previous sections are presented. The main aim is the collection of significant experimental data representative of the regression behaviour of different fuels and of the corresponding engine performance. From the comparison between these experimental data and the numerical results obtained with the models described in CHAPTER 4, it will be possible to assess their validation and to identify possible future improvements.

3.3.1 Test cases with polymeric fuels

In this section, the results of three firing tests performed with different polymeric fuels are presented, which will be considered as test cases for the validation of the numerical model for the prediction of the regression behaviour of pyrolyzing fuels described in Section 4.4.1. In particular:

- Test HDPE-1 was performed with the 200 N-class rocket burning a HDPE fuel grain whose length was equal to $L = 220$ mm and the initial port diameter was equal to $D_I = 15$ mm.
- Test ABS-1 was performed the 200 N-class rocket burning an ABS fuel grain whose length was equal to $L = 240$ mm and the initial port diameter was equal to $D_I = 15$ mm.
- Test HDPE-2 was performed with the 1 kN-class rocket burning a HDPE fuel grain whose length was equal to $L = 570$ mm and the initial port diameter was equal to $D_I = 25$ mm.

In all cases, gaseous oxygen was employed as oxidizer. The test duration was set to 12 s in both tests with the subscale engine and to 42 s in the test with the larger scale rocket.

A picture of the rocket exhaust plume for the firing Test HDPE-1 is shown in Figure 3.5.

Figure 3.6 shows a sequence of pictures of the rocket nozzle taken at three instants after the engine burnout for the same test. It is interesting to note the intense brightness which testifies the very high temperatures reached in the nozzle block at the end of the test, caused by the severe thermo-fluid dynamic conditions to which it is exposed.



Figure 3.5. Rocket exhaust plume (Test HDPE-1).

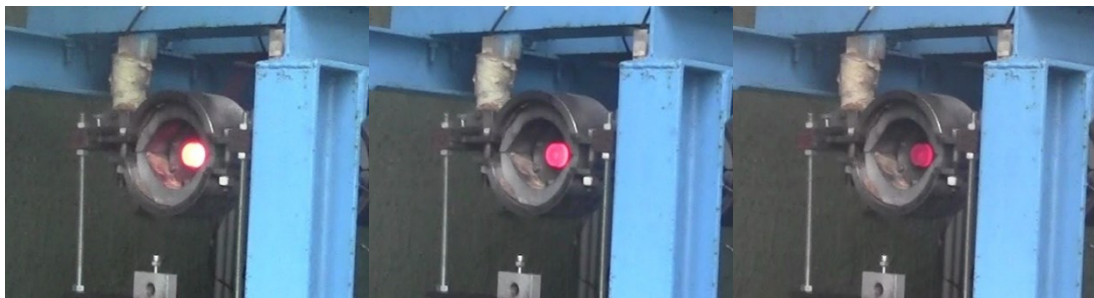
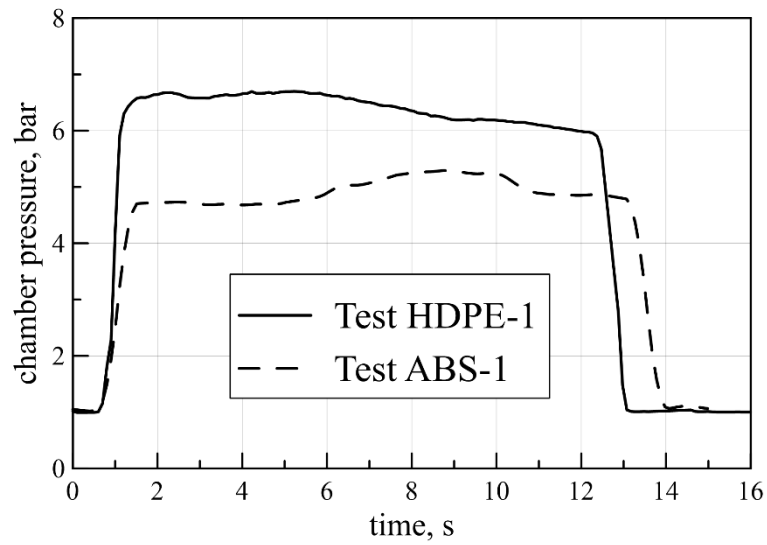


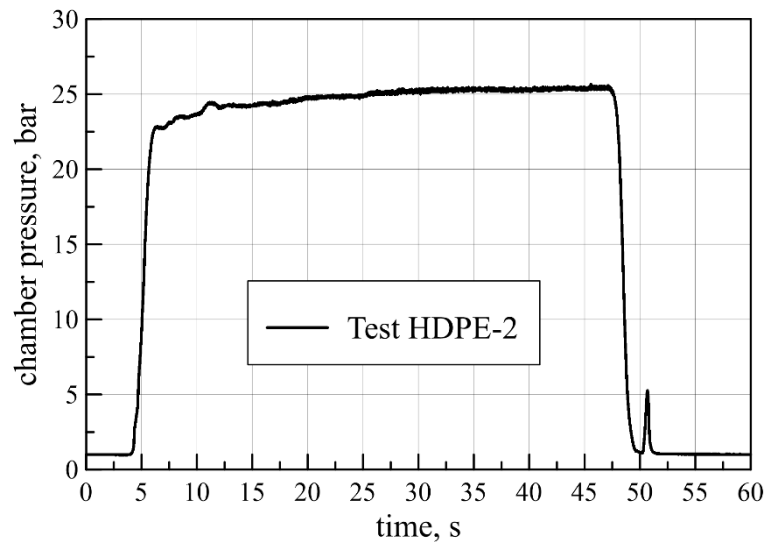
Figure 3.6. Sequence of pictures of the hybrid rocket exhaust nozzle after the firing test (Test HDPE-1).

The trend of the motor operating pressures over the firing time is shown in Figure 3.7 for the three tests.

Referring for example to Test HDPE-1, the oxygen feeding valve starts to open at 0 s (test initial time) to deliver the oxygen flow rate targeted for the test; for the valve opening delay, oxygen starts flowing after about 0.9 s and stops after 12.3 s; simultaneously high-pressure nitrogen is fed into the engine for immediate shutdown.



a) Test with the subscale hybrid rocket



b) Test with the larger scale hybrid rocket

Figure 3.7. Operating pressures vs time.

The decreasing trend of the chamber pressure in Test HDPE-1 (continuous line in Figure 3.7a) can be explained with the nozzle erosion during the test, whose throat diameter has increased from 9.6 mm to 10.6 mm, as measured after the test. On the contrary, the use of the water-cooled nozzle in Test HDPE-2 allowed having constant nozzle throat section area; consequently, the chamber pressure showed a slightly increasing trend, because of the fuel mass flow rate growth, determined by the increase

of the burning surface, which is prevailing on the effect of regression rate decrease (see Figure 3.7b). The detrimental effect of the nozzle throat erosion highlighted above makes necessary the design and manufacturing of new high performance materials with good erosion resistance to the highly severe atmosphere typical of rocket propulsion applications, avoiding on the other side complex and heavy cooling systems. This topic will be analysed in detail in CHAPTER 6, where the results of other firing test performed in similar conditions, but using UHTCMC throat insert or complete nozzle, will be described. The nozzle throat diameter in Test ABS-1 was equal to 12 mm, and this explains the lower chamber pressure measure during the firing.

The average parameters, measured over the firings as described in Section 3.2, are summarised in Table 3.1.

Table 3.1. Experimental data of firing test cases with polymeric fuels.

	Test HDPE-1	Test ABS-1	Test HDPE-2
Engine class	200 N-class	200 N-class	1 kN-class
Fuel	HDPE	ABS	HDPE
Grain initial port diameter, mm	15	15	25
Oxygen mass flow rate, g/s	27	27.5	208
Time-space averaged port diameter, mm	19.4	22.4	55.9
Average oxidizer mass flux, kg/m ² s	91.34	69.78	84.75
Time-space averaged regression rate, mm/s	0.39	0.61	0.73
Time-averaged overall mixture ratio	5.63	2.62	3.02
Time-averaged aft-chamber pressure, atm	6.41	4.78	25
Nozzle throat diameter, mm	9.6	12	16

3.3.2 Test cases with paraffin-based fuel grain

For the validation of the numerical model coupled with the gas/surface interface treatment for liquefying fuels presented in Section 4.4.2, a number of firing tests have been performed with the subscale hybrid rocket demonstrator burning paraffin-based fuel grains, made of a blending of a low-melting point paraffin wax and a microcrystalline wax, with gaseous oxygen axially injected in the grain single port. Detailed information about the test campaign from which the experimental data have been gathered can be retrieved in Ref. [66].

In particular, seven test cases are considered here. In all the cases single cylindrical port paraffin-based grains with 220 mm length have been employed. A graphite nozzle with 10.7 mm throat diameter was employed. The test were performed by varying the oxidizer mass flow rate and the time-space average port diameter obtained in the firing, with the aim of achieving a significant range of the oxidizer mass flux.

The typical test sequence is similar to the one described in the previous section for Test HDPE-1. The main experimental parameters, measured over the firings as described in Section 3.2, are summarised in Table 3.2. Figure 3.8 shows a picture of the rocket exhaust plume in the case of Test P-4.

Table 3.2. Experimental data of firing test cases with paraffin-based fuel grains performed with the 200 N-class hybrid rocket.

Test	Oxygen mass flow rate, g/s	Time-space averaged port diameter, mm	Time-space averaged oxidizer mass flux, kg/m ² s	Time-space averaged regression rate, mm/s	Time average overall mixture ratio	Average chamber pressure, bar
P-1	16	20.5	48.38	1.63	0.77	4.9
P-2	29	25.0	59.22	1.79	1.03	8.0
P-3	38	26.6	67.83	2.04	1.10	11.2
P-4	42	27.1	72.58	2.29	1.08	12.9
P-5	55.5	29.0	83.75	2.41	1.26	16.9
P-6	59.5	28.0	96.76	2.73	1.19	18.4
P-7	60.5	27.1	105.22	2.96	1.20	19.1

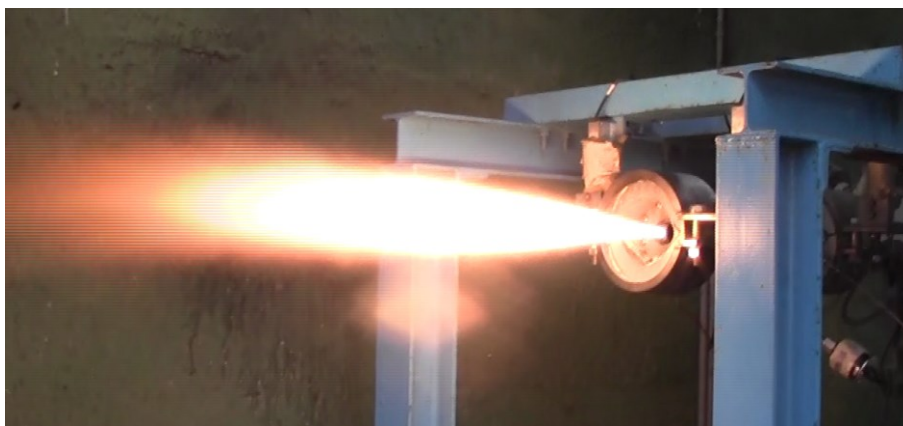


Figure 3.8. Rocket exhaust plume (Test P-4)

CHAPTER 4. MODELLING OF HYBRID ROCKETS INTERNAL BALLISTICS

4.1 Introduction to the definition of the numerical model for hybrid rockets simulation

As mentioned before, one of the fundamental goals of the present dissertation is the definition of a suitable numerical model for the simulation of the thermo-fluid dynamic flowfield in the combustion chamber and through the nozzle of hybrid rockets, which will be presented in this chapter.

As it will be described in details in the following, the definition of such a model followed several steps with an increasing degree of sophistication and accuracy as well as of the predictive capabilities on the fluid dynamics, the fuel consumption and the engine performance.

The first step consisted in identifying the equations governing the complex physical phenomena involved in hybrid rockets internal ballistics, including the proper turbulence closure for the RANS equations and a suitable chemical model for the combustion.

Then, a dedicated treatment for predicting the interaction between the gaseous flowfield and the solid grain surface has been defined and implemented in order to estimate the local fuel regression rate for a fixed condition in terms of oxidizer mass flow rate and grain geometry. This treatment is based on a system of equations based on local mass, energy and species balances and on physical considerations about the consumption mechanism involved depending on the class of fuel. An iterative strategy for the resolution of this system of equations has been adopted, since the solution itself is affected by the thermo-fluid dynamic conditions in the combustion chamber.

Finally, a specific procedure has been implemented for the transient simulation of the grain geometry evolution due to the fuel consumption during the engine operation, consisting in solving at each time-step the flowfield, calculating the regression rate

distribution along the grain surface as described before, and then numerically integrate the regression rate in time in order to calculate the grid nodes displacements. The fluid domain geometry is then modified, the computational mesh is adjusted to the new geometry and the numerical simulation at the new time-step is performed.

4.2 Physical and numerical models for gaseous flowfield simulation

In this section the physical models for the CFD simulation of the thermo-fluid dynamic flowfield in the combustion chamber and through the nozzle of hybrid rockets are presented.

Numerical simulations are carried out with a commercial fluid dynamic solver with ad-hoc user-defined functions. The RANS equations for compressible single-phase multicomponent turbulent reacting flows are solved with a control-volume-based technique and a pressure-based algorithm [67].

For the sake of reader's convenience, the set of equations solved is presented in the following. The Favre-averaged (i.e. density-weighted) equations of continuity and momentum can be expressed in Cartesian tensor form, with the understanding that repeated indices mean summation, as [68]:

$$\frac{\partial \bar{\rho}}{\partial t} + \frac{\partial}{\partial x_j} (\bar{\rho} \tilde{u}_j) = S_m \quad (4.1)$$

$$\frac{\partial}{\partial t} (\bar{\rho} \tilde{u}_i) + \frac{\partial}{\partial x_j} (\bar{\rho} \tilde{u}_i \tilde{u}_j) = -\frac{\partial \bar{p}}{\partial x_i} + \frac{\partial \bar{\tau}_{ij}}{\partial x_j} + \frac{\partial}{\partial x_j} (-\overline{\rho u'_i u'_j}) \quad (4.2)$$

where S_m is the mass source term eventually needed for representing the fuel mass addition.

Here the bar denotes conventional time averaging, while the tilde denotes density-weighted averaging; τ_{ij} is the stress tensor that is defined as

$$\tau_{ij} = \mu \left[\left(\frac{\partial u_i}{\partial x_j} + \frac{\partial u_j}{\partial x_i} \right) - \frac{2}{3} \delta_{ij} \frac{\partial u_k}{\partial x_k} \right] \quad (4.3)$$

where δ_{ij} is the Kronecker delta. Symbols with prime indicate the corresponding quantity fluctuation. The term $\mathcal{R}_{ij} = -\overline{\rho u'_i u'_j}$, originating from the averaging operation, is known as the Reynolds stress tensor, and it needs to be modeled.

4.2.1 Turbulence model

The Shear Stress Transport (SST) turbulence model [69] has been employed for its improved capability of predicting flows with separated regions. This latter is a combination of the robust and accurate k - ω model, developed by Wilcox [70], in the near-wall region, with the standard k - ε model implemented away from the wall using a blending function. With the SST model the transport equations of the turbulence kinetic energy, k , and the specific dissipation rate, ω , are formulated as

$$\frac{\partial}{\partial t} (\bar{\rho} k) + \frac{\partial}{\partial x_i} (\bar{\rho} \tilde{u}_i k) = \frac{\partial}{\partial x_j} \left[(\mu + \mu_t \sigma_k) \frac{\partial k}{\partial x_j} \right] + \mathcal{R}_{ij} \frac{\partial \tilde{u}_i}{\partial x_j} - \beta^* \bar{\rho} \omega k \quad (4.4)$$

$$\begin{aligned} \frac{\partial}{\partial t} (\bar{\rho} \omega) + \frac{\partial}{\partial x_i} (\bar{\rho} \tilde{u}_i \omega) = & \frac{\partial}{\partial x_j} \left[(\mu + \mu_t \sigma_\omega) \frac{\partial \omega}{\partial x_j} \right] + \bar{\rho} \frac{\alpha}{\mu_t} \mathcal{R}_{ij} \frac{\partial \tilde{u}_i}{\partial x_j} - \beta \bar{\rho} \omega^2 + \\ & 2(1 - F_1) \bar{\rho} \sigma_{\omega_2} \frac{1}{\omega} \frac{\partial k}{\partial x_j} \frac{\partial \omega}{\partial x_j} \end{aligned} \quad (4.5)$$

in which the Reynolds stress is modelled using the Boussinesq approximation

$$\mathcal{R}_{ij} = \mu_t \left[\left(\frac{\partial \tilde{u}_i}{\partial x_j} + \frac{\partial \tilde{u}_j}{\partial x_i} \right) - \frac{2}{3} \delta_{ij} \frac{\partial \tilde{u}_l}{\partial x_l} \right] - \frac{2}{3} \bar{\rho} k \delta_{ij} \quad (4.6)$$

The turbulent viscosity, μ_t , is expressed as follows

$$\mu_t = \frac{\bar{\rho} k}{\omega} \frac{1}{\max \left(1; \frac{\Omega F_2}{0.31 \omega} \right)} \quad (4.7)$$

where the function F_2 is defined, depending on the distance from the wall y , as

$$F_2 = \tanh(\Phi_2^2) \quad (4.8)$$

with

$$\Phi_2 = \max\left(\frac{2\sqrt{k}}{0.09\omega y}; \frac{500\mu}{\bar{\rho}\omega y^2}\right) \quad (4.9)$$

The coefficient α is given by

$$\alpha = \gamma \frac{1/9 + Re_t/2.95}{1 + Re_t/2.95} \quad (4.10)$$

where $Re_t = \bar{\rho}k/\mu\omega$ is the turbulent Reynolds number.

The blending function F_1 takes the value of 1 on the wall and tends to zero at the boundary layer edge, being defined as

$$F_1 = \tanh(\Phi_1^4) \quad (4.11)$$

With

$$\Phi_1 = \min\left[\max\left(\frac{\sqrt{k}}{0.09\omega y}; \frac{500\mu}{\bar{\rho}\omega y^2}\right); \frac{4\bar{\rho}\sigma_{\omega_2}k}{CD_{k\omega}y^2}\right] \quad (4.12)$$

where $CD_{k\omega}$ is the positive part of the last term in Eq. (4.5) (cross-diffusion term):

$$CD_{k\omega} = \max\left(2\bar{\rho}\sigma_{\omega_2} \frac{1}{\omega} \frac{\partial k}{\partial x_j} \frac{\partial \omega}{\partial x_j}; 10^{-20}\right) \quad (4.13)$$

The model coefficients σ_k , σ_ω , β , γ are defined by blending the corresponding coefficients of the original k - ω model, denoted with the subscript 1, with those of the transformed k - ε model that are denoted with the subscript 2, as

$$\begin{bmatrix} \sigma_k \\ \sigma_\omega \\ \beta \\ \gamma \end{bmatrix} = F_1 \begin{bmatrix} \sigma_{k_1} \\ \sigma_{\omega_1} \\ \beta_1 \\ \gamma_1 \end{bmatrix} + (1 - F_1) \begin{bmatrix} \sigma_{k_2} \\ \sigma_{\omega_2} \\ \beta_2 \\ \gamma_2 \end{bmatrix} \quad (4.14)$$

All the model constants are listed in Table 4.1.

Table 4.1. Values of SST model constants [68].

Constant	Value	Constant	Value
σ_{k_1}	0.850	σ_{k_2}	1.00
σ_{ω_1}	0.500	σ_{ω_2}	0.856
β_1	0.075	β_2	0.0828
γ_1	0.553	γ_2	0.440
β^*	0.090		

4.2.2 Combustion model

Assuming that the chemical kinetics is fast compared to the diffusion processes occurring in the motor for the typical mass fluxes and chamber pressures considered here [71], the non-premixed combustion of oxygen and gaseous fuel injected from the grain wall is modelled by means of the Probability Density Function (PDF) approach coupled to chemical equilibrium [72]. Accordingly, combustion is simplified to a mixing problem (mixed is burnt), and the difficulties associated with closing non-linear reaction rates are avoided. In fact, under the hypothesis of equal diffusivities for all chemical species and assuming that the Lewis number is equal to 1, the species equations can be reduced to a single equation for the transport of the mixture fraction, which, thus, represents the elemental mass fraction originated from the fuel stream, $f = 1/(1 + OF)$, where OF is the local oxidizer-to-fuel mass ratio for the equivalent non-burning field. The density-averaged mixture fraction equation is

$$\frac{\partial}{\partial t}(\bar{\rho}\tilde{f}) + \frac{\partial}{\partial x_j}(\bar{\rho}\tilde{u}_j\tilde{f}) = \frac{\partial}{\partial x_j}\left(\frac{\mu_t}{Pr_t}\frac{\partial\tilde{f}}{\partial x_j}\right) + S_m \quad (4.15)$$

For the closure model describing turbulence-chemistry interaction, the variance of the mean mixture fraction \tilde{f}'^2 is introduced and an additional equation for this quantity is needed, which, according to [73], and making use of the relation between ω , k , and ε , is written as

$$\frac{\partial}{\partial t}(\bar{\rho}\tilde{f}'^2) + \frac{\partial}{\partial x_j}(\bar{\rho}\tilde{u}_j\tilde{f}'^2) = \frac{\partial}{\partial x_j}\left(\frac{\mu_t}{Pr_t}\frac{\partial\tilde{f}'^2}{\partial x_j}\right) + 2\frac{\mu_t}{Pr_t}\left(\frac{\partial\tilde{f}}{\partial x_j}\right)^2 - 2\beta^*\bar{\rho}\omega\tilde{f}'^2 \quad (4.16)$$

The shape of the assumed PDF is described by the β -function of the mean mixture fraction and its variance [74].

Finally, in non-adiabatic systems, changes in the total enthalpy H due to heat loss or gain impacts the chemical equilibrium calculation and the temperature and species of the reacting flows. Consequently, neglecting the contribution from viscous dissipation, the conduction and species diffusion terms combine to give the following total enthalpy form of the energy equation

$$\frac{\partial}{\partial t}(\bar{\rho}\tilde{H}) + \frac{\partial}{\partial x_j}(\bar{\rho}\tilde{u}_j\tilde{H}) = \frac{\partial}{\partial x_j}\left(\frac{\mu_t}{Pr_t}\frac{\partial\tilde{H}}{\partial x_j}\right) + S_h \quad (4.17)$$

where Pr_t is the turbulent Prandtl number, which is assumed equal to 0.85, and the source term S_h includes the volumetric heat of phase change (see Section 4.4.2).

Once \tilde{f} and \tilde{f}'^2 and H are calculated at each point in the flowfield, the known PDF is used to compute the time-averaged values of individual species mole fractions, density and temperature with simple thermochemistry calculations based on the minimization of Gibbs free energy [65].

4.2.3 Thermodynamic and transport properties

Heat capacities, molecular weights, and enthalpies of formation for each species considered are extracted from the solver chemical database. In particular, the specific heat of the single species is determined as a piecewise polynomial function of the local temperature, while the mixture's specific heat, C_p , is then determined as a mass fraction average of the pure species heat capacities, i.e. with the following mixing law

$$C_p = \sum_i Y_i C_{p,i} \quad (4.18)$$

where Y_i is the mass fraction of the i -th species and $C_{p,i}$ is the corresponding specific heat capacity.

Molecular dynamic viscosities and thermal conductivities of the i -th species are calculated as functions of local temperature, as

$$\ln \mu_i = A_{\mu,i} \ln T + \frac{B_{\mu,i}}{T} + \frac{C_{\mu,i}}{T^2} + D_{\mu,i} \quad (4.19)$$

$$\ln \lambda_i = A_{\lambda,i} \ln T + \frac{B_{\lambda,i}}{T} + \frac{C_{\lambda,i}}{T^2} + D_{\lambda,i} \quad (4.20)$$

where the fitting coefficient $A_{\mu,i}$, $B_{\mu,i}$, $C_{\mu,i}$, $D_{\mu,i}$, $A_{\lambda,i}$, $B_{\lambda,i}$, $C_{\lambda,i}$, $D_{\lambda,i}$, are taken from Ref. [65]. The mixture's dynamic viscosity, μ , and thermal conductivity, λ , are then calculated by means of the following mixture formula [65]

$$\mu = \sum_i \frac{X_i \mu_i}{X_i + \sum_{j \neq i} X_j \phi_{ij}} \quad (4.21)$$

$$\lambda = \sum_i \frac{X_i \lambda_i}{X_i + \sum_{j \neq i} X_j \psi_{ij}} \quad (4.22)$$

where X_i is the mole fraction of the i -th species, ϕ_{ij} is the viscosity interaction coefficient between species i and j in eq. (4.21) and ψ_{ij} is the interaction coefficient between species i and j in eq. (4.22). For the interaction coefficient the following form is used

$$\phi_{ij} = \frac{1}{4} \left[1 + \left(\frac{\mu_i}{\mu_j} \right)^{\frac{1}{2}} \left(\frac{M_j}{M_i} \right)^{\frac{1}{4}} \right]^2 \left(\frac{2M_j}{M_i + M_j} \right)^{\frac{1}{2}} \quad (4.23)$$

$$\psi_{ij} = \phi_{ij} \left[1 + \frac{2.41(M_i - M_j)(M_i - 0.142M_j)}{(M_i + M_j)^2} \right] \quad (4.24)$$

where M_i is the molecular weight of the species i .

4.3 Computational domain and boundary conditions

The simulations that will be presented in CHAPTER 5 have been all performed considering a simple engine configuration with the conical axial injector for the oxidizer, which yield an axially-symmetric flowfield. Consequently, the numerical computations are performed with two-dimensional structured grids representing the internal volume of the pre-chamber, the fuel grain port, the post-chamber and the nozzle of the two hybrid rockets presented in Section 3.1.1.

A typical computational grid employed for the 200 N-class rocket is shown in Figure 4.1. Note that it is only an example, inasmuch as the grain length and the port diameter change for the different considered cases. As it can be observed from Figure 4.1, the cells are clustered towards the grain wall in such a way to ensure that the maximum value of y^+ is around 2÷3 at the wall-adjacent cell all along the grain length for all the considered test cases. Additional axial clustering of cells is placed in the regions near the grain inlet and outlet edges, and near the pre-chamber, post-chamber and nozzle inner surfaces. In order to assess the convergence of the numerical results with the mesh size, grid sensitivity analyses have been performed considering three

mesh refinement levels and applying the methods reported in [75] to have an estimation of the numerical errors in terms of the average computed regression rate and its components. The grid convergence analyses are described in detail in Sections 5.1.2 and 5.2.2.

A similar computational grid is defined for the test cases performed with the 1 kN-class hybrid rocket. The main dimensions are listed in Table 4.2.

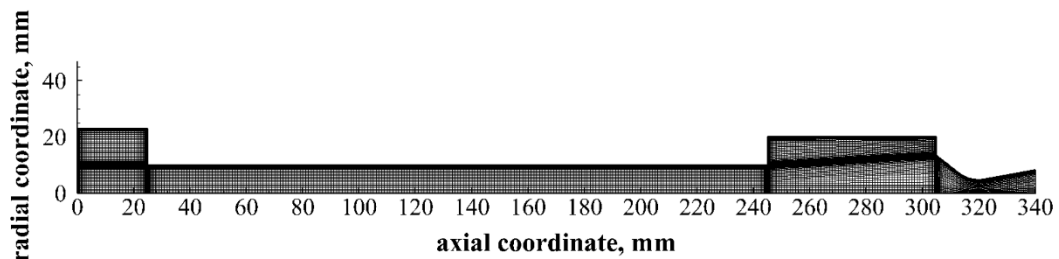


Figure 4.1. An example of the computational grid for the 200 N-class engine

Table 4.2. Computational domain dimensions.

Engine	Pre-chamber diameter	Pre-chamber length	Fuel grain length	Post-chamber diameter	Post-chamber length
200 N-class	46 mm	25 mm	220; 240 mm	40 mm	60; 40 mm
1 kN-class	80 mm	70 mm	430; 570 mm	80 mm	200; 60 mm

For what concern the boundary conditions, on the inner surface of both the pre-chamber and post-chamber as well as on the nozzle wall no-slip and adiabatic boundary conditions are imposed. At the injector exit section, a mass flow boundary condition is prescribed along with the temperature (equal to 300 K), the oxygen mass fraction and the turbulent quantities, while a pressure outlet condition is set at the nozzle exit section.

4.4 Gas/fuel surface interface modelling

The theoretical model formulation has to be completed by assigning the boundary conditions at the interface between the gaseous flow region and the solid fuel wall,

which can properly describe the fuel consumption mechanism. The fuel surface is, actually, an inlet boundary along which both the fuel mass flux, the temperature and the mixture fraction depends on the regression rate that is an unknown to be determined.

At this point it is necessary to distinguish the case of classical polymeric fuels and the case of liquefying fuels. In fact, in both cases the gas/surface interface treatment is based on local mass, energy and mean mixture fraction balances, but while in the former case a proper additional equation is needed for modelling the pyrolysis mechanism which governs the fuel consumption, in the latter case a different treatment is needed to take properly into account the entrainment of liquid droplets from the unstable melt layer forming along the fuel surface, which becomes dominant.

4.4.1 The case of polymeric fuels

Under the hypothesis that no material is removed from the surface in a condensed phase (neither solid, such as in the case of fuel loaded with metal particles, nor liquid, when, for instance paraffin wax is used), the mass conservation at the gas-solid interface over a pyrolyzing fuel grain imposes that

$$(\rho v)_w = \rho_f \dot{r} \quad (4.25)$$

where ρ is the gas density at the wall, and v is the normal-to-wall velocity component due to the pyrolysis products injection; ρ_f is the solid fuel density and \dot{r} is the local regression rate.

As anticipated in Section 1.2.1, the energy balance at the gas-solid interface, taking into account the convective heat transfer from the gas to the fuel surface, the heat conduction into the solid, and neglecting the radiation (the latter is known to produce second order effects with the non-metallized propellant considered here [76]) leads to the following relationship between the convective heat flux to the wall, \dot{q}_w , and the regression rate [37]

$$\dot{q}_w = \left(\lambda_g \frac{\partial T}{\partial n} \right)_w = \rho_f \dot{r} [\Delta h_p + C_f (T_w - T_a)] \quad (4.26)$$

where n is the coordinate normal to surface oriented from solid to gas, λ_g the gas thermal conductivity, C_f is the solid heat capacity per unit mass, Δh_p the so-called heat of pyrolysis, T_w is the fuel surface temperature, and T_a is its initial temperature (which is assumed equal to the one of the external surface of the fuel). The term in brackets at the right-hand side represents the effective heat of gasification of the fuel, which, further than for the heat of pyrolysis, accounts for the heat conducted into the solid grain. Note that, concerning the latter energy term, for the negligible surface temperature axial variation (as will be observed next), heat conduction only in the direction normal to the grain surface is considered.

The fuel pyrolysis is, finally, modelled with the following semi-empirical Arrhenius-type equation [77] relating the regression rate to the fuel surface temperature

$$\dot{r} = A \cdot \exp\left(-\frac{E_a}{2RT_w}\right) \quad (4.27)$$

where A is the pre-exponential factor, E_a is the activation energy and R is the universal gas constant.

The values of the constants appearing in Eqs. (4.26) and (4.27) considered for the HDPE and for ABS fuel grains analysed in this work are summarized in Table 4.3. Density, specific heat and heat of pyrolysis for HDPE are taken from the work in Ref. [78], while the values of the pre-exponential factor and the activation energy from Ref. [77] by modifying the activation energy to match the surface temperature commonly observed in polymeric hybrid fuels (which is around 800 K) [79]. The properties for ABS are taken from the work in Ref. [80], with similar considerations for the activation energy.

Table 4.3. Solid fuels properties and rate constants.

Fuel	Density, ρ_f , kg/m ³	Specific heat, C_f , J/kg K	Heat of pyrolysis, Δh_p , MJ/kg	Initial fuel temperature, T_a , K	Pre- exponential factor, A , mm/s	Activation Energy, E_a , kJ/mol
HDPE	950	2833	4.045	300	$4.78 \cdot 10^6$	190
ABS	1020	2620	1.890	300	7.194	32

A specific treatment of the boundary condition on the mean mixture fraction at the gas-solid interface is needed as well. In fact, for the low fuel regression rate of hybrid rockets, the normal convection of the fuel at the grain surface is relatively weak compared to the gas convection in the cells near the boundary; furthermore, there exist significant differences in the species concentrations between the fuel surface and the cells adjacent to the boundary, so that a steep mixture fraction gradient at the fuel wall is present. In this conditions the diffusive flux plays a dominant effect in the mixture fraction transport.

As a consequence, if a simple Dirichlet-type boundary condition is applied on the gas-fuel interface, by imposing $f = 1$, extra mixture fraction will be diffused into the flow affecting the global oxidizer to fuel ratio and the chemical equilibrium properties, which eventually leads to an incorrect estimation of the characteristic exhaust velocity and chamber pressure.

A possible approach proposed to mitigate this problem may consist in imposing that the diffusion coefficient μ_t/Sc_t is equal to zero in the cells close to the fuel inlet boundary, but this would imply a non-exact evaluation of the gradients in this zone, and, in particular, of the heat flux to the fuel wall, which, for Eq. (4.26), would lead to a mistaken regression rate.

The correct solution to this problem is to consider an additional equation for the mean mixture fraction balance at the gas-solid interface, which can be expressed as

$$(\rho v)_w f_w - \left(\frac{\mu_t}{Pr_t} \frac{\partial f}{\partial n} \right)_w = \rho_f \dot{r} \quad (4.28)$$

According to this equation, the total mass flux entering the gaseous domain due to the solid fuel regression, which appears on the right-hand side of the equation and represents the production term, is partially balanced by the convection and partially by the diffusion of the fuel mass fraction.

Finally, the enhanced wall treatment is employed for the turbulence boundary conditions at the gas/solid interface.

Note that Eqs. (4.26), (4.27) and (4.28) constitute a system of three algebraic equations in the three unknowns, regression rate, surface temperature and mixture fraction, whose resolution needs the computation of the heat flux and of the mixture fraction diffusive flux to the wall from the flowfield solution. As the flowfield, indeed, depends on the abovementioned parameters at the grain surface, the problem needs to be solved iteratively. In particular, first a constant regression rate value is assumed and the corresponding values of the fuel mass flux entering in the computational domain and the surface temperature T_w are computed according to Eqs. (4.25) and (4.26), respectively. The fuel mass flux and surface temperature values are imposed as boundary conditions at the solid-gas interface and the flowfield numerical resolution is started. Then, at each numerical iteration the convective heat flux and the species diffusion to the wall are evaluated so that Eqs. (4.26)-(4.27)-(4.28) can be solved simultaneously, the new distributions of the temperature, mean mixture fraction and fuel regression rate along the grain surface are computed and the boundary conditions are accordingly adjusted. The iterative procedure is stopped when the residuals of each volume balance equation is smaller than 10^{-3} and when the following criterion is satisfied

$$\frac{\|\dot{r}_i - \dot{r}_{i-1}\|}{\|\dot{r}_i\|} < 10^{-2} \quad (4.29)$$

where \dot{r}_i is the regression rate axial profile at the i -th numerical iteration.

4.4.2 The case of liquefying fuels

In the case of liquefying fuels, as already mentioned, the regression rate, \dot{r} , can be split in the sum of two components: the vaporization fraction of regression rate, \dot{r}_v , that is generated by the fuel gasification, and the entrainment fraction, \dot{r}_{ent} , that is related to the mechanical transfer of the liquid droplets from the surface melt layer

$$\dot{r} = \dot{r}_v + \dot{r}_{ent} \quad (4.30)$$

On the other side, in this case the fuel surface temperature is considered known and equal to the paraffin vaporization temperature T_v , and an isothermal boundary condition is set along the fuel wall.

Again, the enhanced wall treatment is employed for the turbulence boundary conditions at the gas/solid interface.

Therefore, a set of equations is needed for the calculation of the regression rate and its two components and the resulting fuel mass flow rates, which have to be included in the fluid dynamic computation. As mentioned before, the approach consists mainly in considering again the mass, energy and species balances at the gas/solid interface, but in the present case it is necessary to define an additional equation for the calculation of the entrainment component of the fuel mass flow rate.

From the energy balance at the fuel grain wall, the following relationship of the total surface heat flux with the total and the vaporization regression rate is obtained

$$\dot{q}_w = \rho_f \dot{r} [C_s(T_m - T_a) + L_m + C_l(T_v - T_m)] + \rho_f \dot{r}_v L_v \quad (4.31)$$

where ρ_f is the solid fuel density, C_s and C_l are the specific heats of the solid and liquid fuel (which are here considered independent from temperature), respectively, T_a is the ambient temperature, T_m is the fuel melting temperature, and L_m and L_v are the fuel heat of fusion and the heat of vaporization, respectively. This equation represents the fact that the total energy transferred from the combusting gases to the fuel surface must be equal to, following the terms on the right-hand-side of Eq. (4.31), the fraction required to heat the solid up to the melting temperature, the fraction required for the

melting, the one to heat the liquid layer up to the vaporization temperature, and, finally, to the component required for vaporization. The latter contribution involves only the fuel mass flow rate due to the vaporization component of the regression rate.

Except for the vaporization temperature, the values of the constants appearing in Eq. (4.31) found in the literature do not show significant variations with the paraffin fuel formulation; anyway, their effect on the simulations results has been here assumed to be negligible. The values considered in this study are taken from Ref. [23] and are listed in Table 4.4. Whereas, the vaporization temperature has an important role, as it affects both the heat flux to the wall and the term $C_l(T_v - T_m)$ appearing in Eq. (4.31), which, in turn, both influence the fuel regression rate. This parameter much depends on the fuel formulation and it is not always known, thus a parametric analysis has been carried out in this work and will be described in the following.

Table 4.4. Paraffin fuel properties.

Solid fuel density, ρ_f , kg/m ³	Specific heat solid phase, C_s , J/kg K	Specific heat liquid phase, C_l , J/kg K	Heat of fusion, L_m , kJ/kg	Heat of vaporization, L_v , kJ/kg	Melting temperature, T_m , K
920	2030	2920	167.2	163.5	339.6

According to the approach described in [23] and [22], in this work, the following semi-empirical relationship has been considered for modelling the entrainment component of the fuel regression rate

$$\dot{r}_{ent} = a_{ent} \frac{G^{2\zeta}}{\dot{\gamma}^\xi} \quad (4.32)$$

where $G = 4\dot{m}/\pi D^2$ is the total mass flux in the local section of the grain port, ζ and ξ are correlation constants (here $\zeta = \xi = 1.5$) and a_{ent} is a factor depending on the physical properties of the selected fuel, primarily on the fuel liquid viscosity, and on the average gas density in the chamber as

$$a_{ent} \propto \frac{1}{\mu_l \rho_g \zeta} \quad (4.33)$$

Eq. (4.32) is based on theoretical considerations about the fluid dynamic stability of the surface liquid layer for which the susceptibility of a given fuel to this instability increases with decreasing viscosity and surface tension of the melt layer; the entrainment component of fuel regression rate is, therefore, roughly inversely proportional to viscosity and surface tension (to a lesser degree) evaluated at the characteristic temperature of the layer, while it depends directly on dynamic pressure, and layer thickness, which, properly rearranged, yield Eq. (4.32).

A parametric analysis has been carried out also to assess the effect of the coefficient a_{ent} , which, as mentioned above, essentially corresponds to studying the effect of the fuel liquid viscosity on the different components of the fuel regression rate. The considered values are of the same order of magnitude of the one employed in the calculation reported in Ref. [23].

Once Eqs. (4.30), (4.31) and (4.32) are combined, given the heat flux to the wall and the total mass flux, the three components of the fuel regression rate can be calculated. Correspondingly, the fuel mass fluxes associated to the vaporization and entrainment components, respectively, are obtained as follows

$$G_{f,v} = \rho_f \dot{r}_v \quad (4.34)$$

$$G_{f,ent} = \rho_f \dot{r}_{ent} \quad (4.35)$$

Vaporization and entrainment components are handled differently.

The vaporization component is treated as described in the previous section for the case of pyrolyzing fuels, considering the mass and mixture fraction balance equations at the grain wall, given by

$$(\rho v)_w = G_{f,v} \quad (4.36)$$

$$(\rho v)_w f_w - \left(\frac{\mu_t}{Pr_t} \frac{\partial f}{\partial n} \right)_w = G_{f,v} \quad (4.37)$$

This allows taking correctly into account the blocking effect on the heat transfer to the wall. Furthermore, as explained in the previous section, Eq. (4.37) is needed to ensure the mixture fraction global balance for which the mass flux due to the vaporization component of the fuel regression entering the computational domain, which appears on the right-hand side of the equation, is partially balanced by the convection, and partially by the diffusion of the fuel mass fraction.

As mentioned above, the entrainment mass flux does not participate to the blocking effect, thus a specific treatment is adopted for the introduction of the entrainment component into the computational domain. Assuming that, despite the entrained droplets are initially in the liquid phase, they immediately gasify because of the large combustion heat release, the local entrainment contribution is assigned as a mass production term in the local volume of the grain port corresponding to the surface cell of length Δx through which the fuel mass enters the fluid domain, $\pi D^2 \Delta x / 4$:

$$S_m = 4 \frac{G_{f,ent}}{D} \quad (4.38)$$

In order to satisfy also the species balance, an equal production term is assigned also for the mean mixture fraction. Finally, the energy required by the gasification of the liquid fuel mass flow rate is taken into account assigning in the same volume a corresponding negative energy source term:

$$S_h = -4 \frac{G_{f,ent}}{D} L_v \quad (4.39)$$

As the heat flux to the surface and the total mass flux needed for the calculation of the regression rate and its components are outputs of the flowfield resolution, which, in turn, depends on the regression rate itself, an iterative procedure, similar to that described for the case of polymeric fuels, is needed for the problem solution.

4.5 Port diameter update with time for the transient simulation of the fuel grain consumption

As anticipated before, a common practice for the hybrid rocket internal ballistics numerical simulation is performing a single numerical simulation for the entire firing test considering the time-space averaged port diameter [36], [37]. In fact, results obtained in Ref. [37] have shown that the time-and-spatially averaged regression rate obtained through simulations conducted at different grain geometries (each corresponding to a specific stage in the burn), thanks to the employed mass flux averaging definition [81], is only deviating by a few percent from the spatially averaged regression rate calculated with a single simulation at the average port diameter. However, in the competent literature, even when analyses have been performed at several stages of the motor firing, the grain inner diameter has been always considered uniform down the port; in other words, the axial non-uniformity of the regression rate has been usually neglected and the port diameter has been updated with a spatially-averaged regression rate value. In the present work, this limitation has been superseded, and in addition to the steady simulation at time-space averaged port diameter, the considered firing test cases with polymeric fuels have been also simulated updating the local port diameter at a given instant on the basis of the local regression rate calculated at the instant before.

In particular, for the surface regression the fluid-solid interface boundary changes in time; the displacements of the computational grid nodes are not uniform throughout the grain length but, rather, vary because at each point the regression rate has a different value. Furthermore, since the regression rate is defined in the direction normal to the fuel surface, due to the local surface inclination the displacement of a generic point occurs not only along the radial direction, but also along the axial direction.

In the present work, a forward numerical integration of the local fuel regression rate has been implemented in order to calculate the grid nodes displacement. Starting from a certain grain port profile at the n -th time-step, defined by the vectors of the axial and radial coordinates x_i^n , y_i^n of the grid nodes (where the subscript i indicates

the i -th node), CFD simulation is carried out with the iterative numerical procedure described before in order to compute the fuel regression rate distribution $\dot{r}^n(x_i)$ at the same time step. This regression rate is then integrated forward in order to calculate the displacement after a fixed time-step $\Delta t = t^{n+1} - t^n$, which for the i -th node can be expressed as

$$\Delta_i^n = \dot{r}^n(x_i)\Delta t \quad (1)$$

If we indicate with ϑ_i the local inclination of the fuel surface with respect to the axial direction in the i -th node (see Figure 4.2), the coordinates of the same node at the time t^{n+1} can be calculated as

$$x_i^{n+1} = x_i^n - \Delta_i \cos \vartheta_i \quad (2)$$

$$y_i^{n+1} = y_i^n + \Delta_i \sin \vartheta_i \quad (3)$$

allowing reconstructing the new grain port profile.

Once the new distribution is calculated, the fluid domain geometry is consequently modified, the computational mesh is adjusted to the new geometry and the numerical simulation at the new time-step is performed.

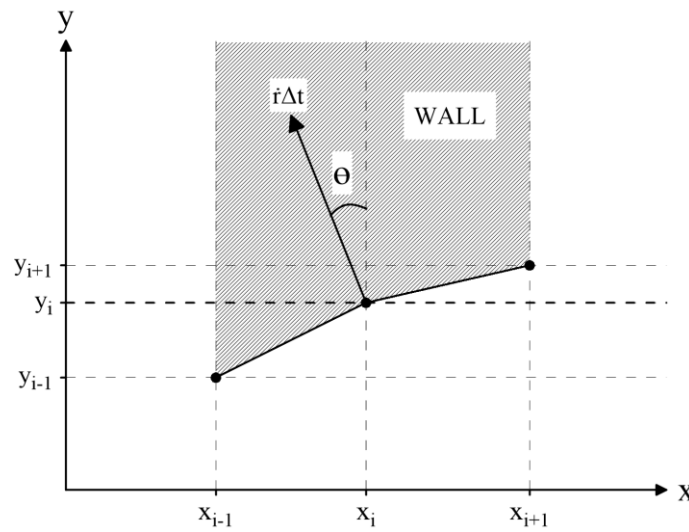


Figure 4.2. Schematic representation of the i -th node displacement components.

CHAPTER 5. NUMERICAL RESULTS OF HYBRID ROCKETS INTERNAL BALLISTICS SIMULATION

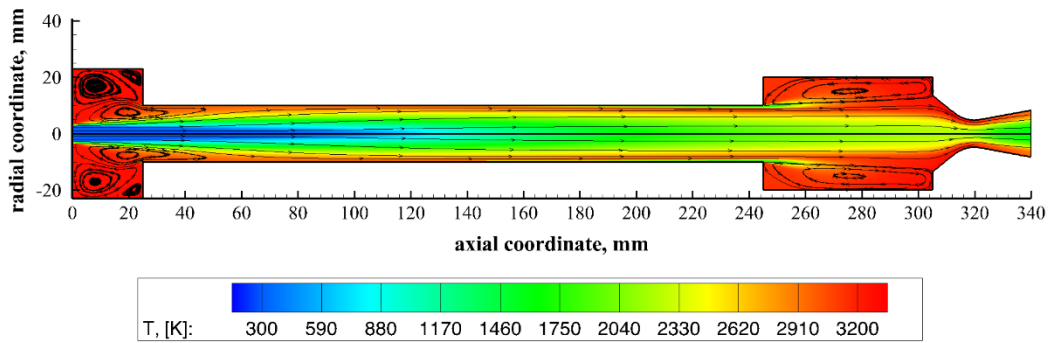
5.1 Numerical results in the case of polymeric fuels

In this section the numerical results obtained with the abovementioned method for the case of classical polymeric fuels, i.e. with the gas/surface interface treatment presented in Section 4.4.1, are presented. First, the results of two steady simulations carried out in the cases corresponding to Test HDPE-1 and Test ABS-1 are presented and compared with the experimental data for the validation of the employed numerical model. Then, the results of the two transient simulations carried out updating the grain port geometry during the time of the engine operation (as described in Section 4.5) in the cases corresponding to Test HDPE-1 and Test HDPE-2 are presented and again compared with the experimental data.

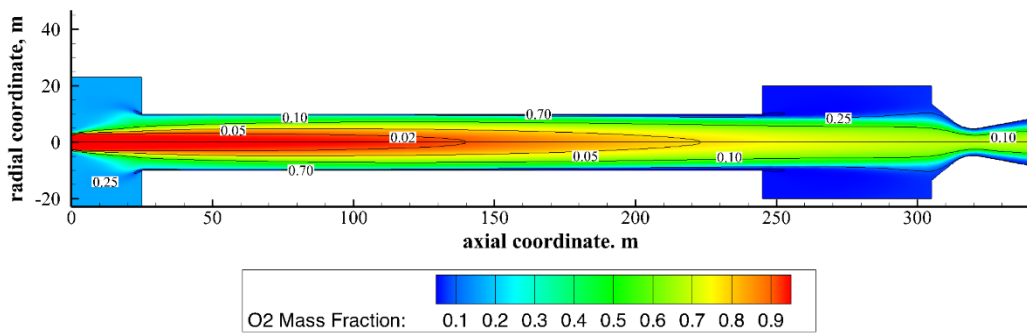
5.1.1 Steady simulations

In this section, the results of the numerical simulations carried out in the conditions of the Test HDPE-1 and Test ABS-1, presented in Section 3.3.1, are analysed. Values of oxygen mass flow rate in Table 3.1 are enforced in the calculation. The simulations were carried out considering the time-spatially averaged grain port diameter in the burns, since they can provide meaningful details of the flowfield in the hybrid rocket combustion chamber and the corresponding average regression rate, and are then valuable for a preliminary validation of the numerical model.

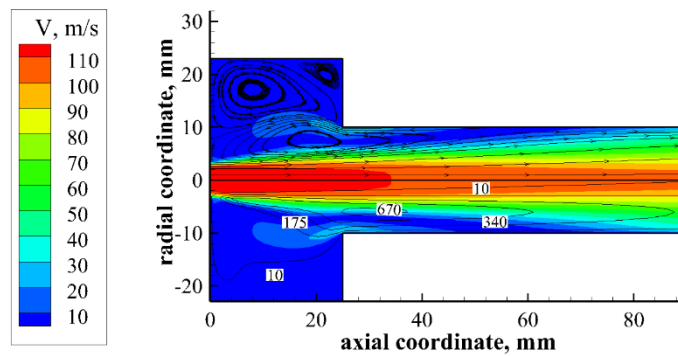
Figure 5.1 and Figure 5.2 show the most significant results calculated in the two test cases, respectively.



a) Temperature contour plot and streamlines.

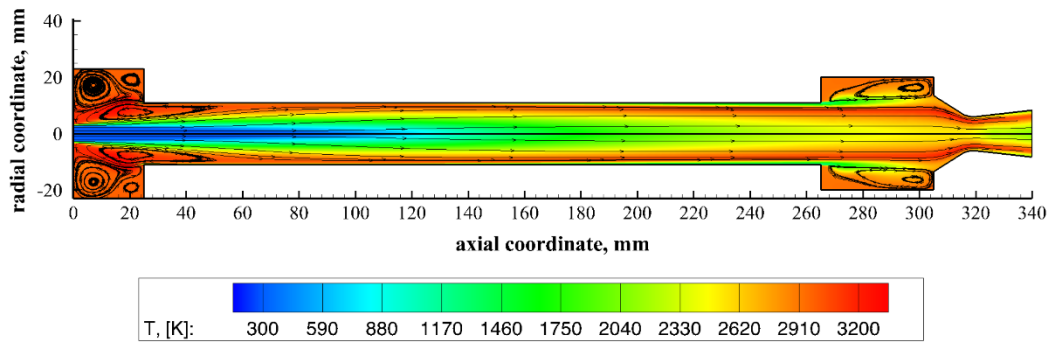


b) O₂ mass fraction contour plot and mixture fraction isolines.

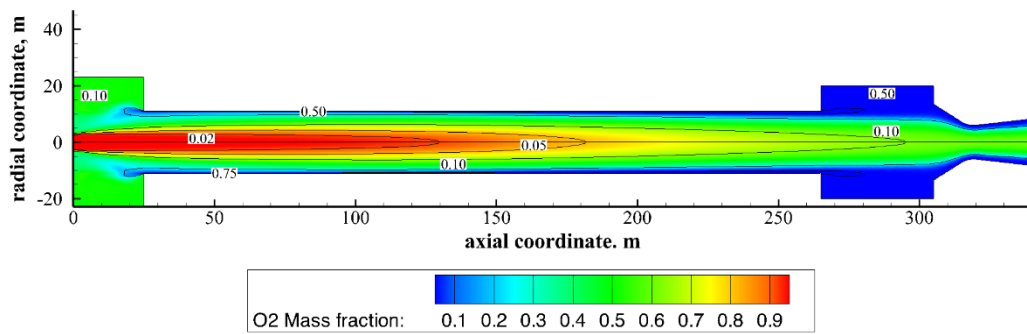


c) Velocity magnitude contour plot, streamlines and turbulent kinetic energy isolines (bottom half) in the injection zone.

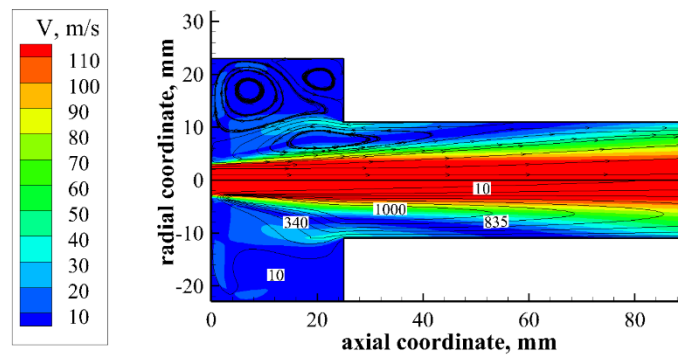
Figure 5.1. Results of the steady-state numerical simulation in the case of Test HDPE-1.



a) Temperature contour plot and streamlines.



b) O_2 mass fraction contour plot and mixture fraction isolines.



c) Velocity magnitude contour plot, streamlines and turbulent kinetic energy isolines (bottom half) in the injection zone.

Figure 5.2. Results of the steady-state numerical simulation in the case of Test ABS-1.

First, it can be observed that the combustor inlet flowfields, which are similar in the two considered test cases, are dominated by the development of the oxygen jet

emerging from the axial injector (that is clearly distinguishable from the low-temperature, high-oxygen-concentration region), spreading almost linearly up to the impingement point on the grain surface, which is located 35 mm and 40 mm ahead of the grain entrance section (in accordance with the point calculated assuming a free jet pattern with a spreading angle of 8° [82]). Upstream of the impingement point, in the entrance region of the grain, there is an extended recirculation region characterized by a main, broad counter-clockwise-rotating vortex that is bounded, on the front side, by the zone of oxygen impingement. In the pre-combustion chamber, another large vortex, clockwise rotating, is formed delimiting the main one on the backside. Finally, also in the aft-mixing chamber, a large trapped counter-clockwise-rotating vortex is formed [17], [83], which further promotes the propellant mixing, improving the combustion efficiency (the mass-weighted average temperature at the nozzle inlet section is increased of around 10% with respect to that at the grain outlet section).

As a result of the flow recirculation generated at the motor head end, propellant mixing is strongly promoted, and combustion takes place in the recirculation core; hot combustion gases are transported from the grain entrance region back to the pre-chamber, where temperature is very high (around 2500 K in both cases). Downstream of the recirculation, the temperature distribution reflects the typical structure of a diffusion flame, in which the oxidizer and the fuel combine by diffusion from separate regions (in the present case the oxygen diffuses from the jet core towards the grain surface and, on the contrary, the fuel is injected from the grain surface and diffuses towards the core flow) and a narrow region close to the fuel surface forms where the near-stoichiometric conditions are reached and the temperature shows its maximum value (around 3200 K which is the maximum value which can be reached in stoichiometric conditions supposing chemical equilibrium for the combustion of oxygen and ethylene). Anyway, as a consequence of the relatively high turbulent kinetic energy determined by the different vortices, which increase the mixing so that a non-negligible amount of fuel reaches the central region of the combustion chamber, relatively high temperatures characterize also the core flow (differently to what happens for example in a classical configuration with a uniform oxygen injection through the grain entrance section, as testified in Refs. [37, 42]).

Figure 5.3 shows the computed fuel regression rate axial profiles in the two considered cases compared with the experimental data of the corresponding firing tests. In both cases, the regression rate axial distribution yields a peak, due to the oxygen jet impingement, followed by a minimum point, after which it monotonically increases. This behaviour is typical of the boundary layer heat transfer, for which the heat flux increase due to the mass addition down the port becomes dominant on the decrease due to the boundary layer growth from a certain axial distance. Furthermore, this effect is more prominent in the case of the test with ABS, where, because of the smaller heat of pyrolysis (see Table 4.3), the fuel regression rate and consequently the mass addition are higher.

Considering that the numerical regression rates have been calculated at the average port diameter, whereas the experimental data are, of course, been retrieved after the motor extinguishment, in both the firing test cases a good agreement between numerical results and experiments is shown, yielding the maximum deviation in correspondence of the point of maximum consumption; however, note that in this zone the maximum experimental uncertainty is obtained, because of the asymmetric consumption determined by the motor ignition device.

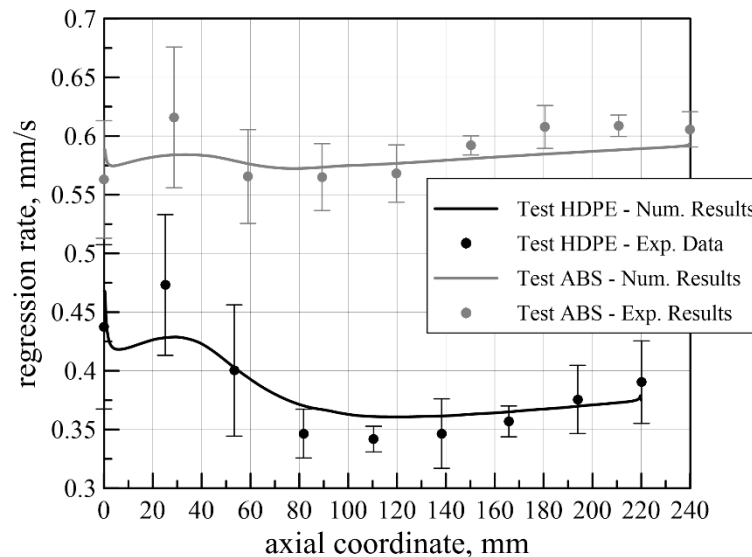


Figure 5.3. Regression rate distributions evolution in the firing with the axial-nozzle injector.

The values of the computed averaged regression rate and pressure in the aft-mixing chamber are reported in Table 5.1, along with the relative errors with respect to corresponding experimental data. Again a good agreement is obtained, which gives confidence on the validation of the numerical model.

Table 5.1. Computed average pressure in the aft-mixing chamber and deviation with experimental data.

Test case	Computed averaged fuel regression rate, mm/s	Regression rate relative error	Aft-mixing chamber pressure, atm	Chamber pressure relative error
HDPE-1	0.384	1.54%	6.52	1.7%
ABS-1	0.581	4.75%	4.91	2.7%

5.1.2 Grid sensitivity analysis

In order to assess the numerical results shown in the previous and in the following sections, a grid sensitivity analysis is carried with three mesh refinement levels.

In the reference mesh the pre-chamber is subdivided into 40×90 grid cells in the axial and radial directions, respectively, the grain port in 240×40 grid cells, the post-chamber in 80×90 cells and the nozzle in 60×40 cells. Cells are clustered towards the grain wall in such a way to ensure that the maximum value of y^+ is around 1 at the wall-adjacent cell all along the grain length. Additional axial clustering of cells is placed in the regions near the grain inlet and outlet edges, and near the pre-chamber, post-chamber and nozzle inner surfaces.

The coarser mesh is constructed doubling the size of the cells in both the axial and the radial directions compared to the reference mesh, while the finer mesh was realized halving the cell size in both directions.

Figure 5.4 shows the axial profiles of the regression rate calculated with the different meshes. It appears that the largest change in regression rate profile is achieved with the first refinement, while the deviation between the regression rates achieved with the reference and the finer meshes is visible in the grain portion subject to recirculation, as expected from the effect of the turbulence intensity which is larger in

that region. Downstream of the attachment point the deviation between the regression rates achieved with the reference and the finer meshes is negligible.

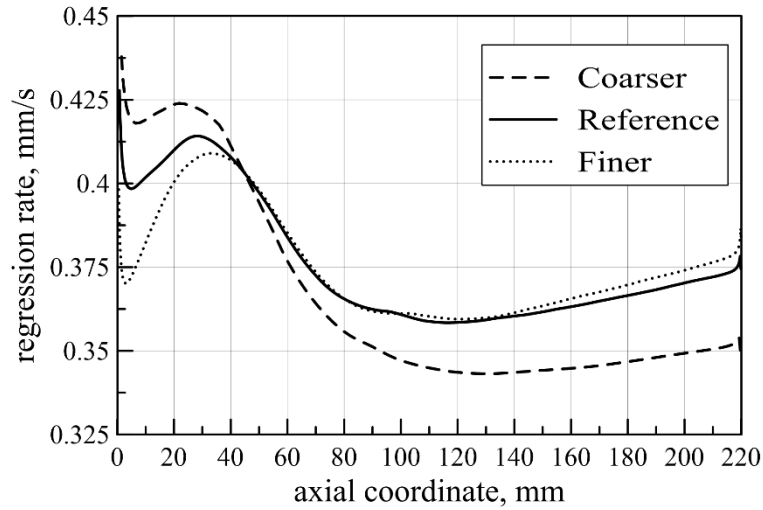


Figure 5.4. Numerical regression rate profiles calculated with different refined computational grids (Test HDPE-1).

Table 5.3 reports the calculated averaged regression rates and aft-mixing chamber pressures obtained with the different meshes and the corresponding numerical errors. The latter is evaluated according to the methods presented in [75], estimating the exact value of the generic quantity \hat{g} as the relevant Richardson's extrapolation

$$\hat{g} = g_c - \frac{2^n \cdot (g_c - g_m)}{2^n - 1} \quad (5.1)$$

where n is the order given by

$$n = \frac{\log \frac{g_c - g_m}{g_m - g_f}}{\log 2} \quad (5.2)$$

and g_c , g_m and g_f are the values of the considered quantity computed with the coarse, medium and fine grids, respectively. The numerical error is then defined as the relative difference between the computed value and the exact value estimated with Eq. (5.1).

It can be seen that the numerical error gathered with the reference mesh is already smaller than 1% and, therefore, it can be stated that a satisfying convergence of the numerical results is obtained.

Table 5.2. Results of grid sensitivity analysis on the spatially averaged regression rate.

Mesh	Averaged regression rate, mm/s	Regression rate numerical error	Aft-mixing chamber pressure, atm	Chamber pressure numerical error
Coarser	0.3782	0.022	6.48	0.008
Reference	0.3840	0.007	6.52	0.002
Finer	0.3859	0.002	6.53	0.0005

5.1.3 Transient simulation

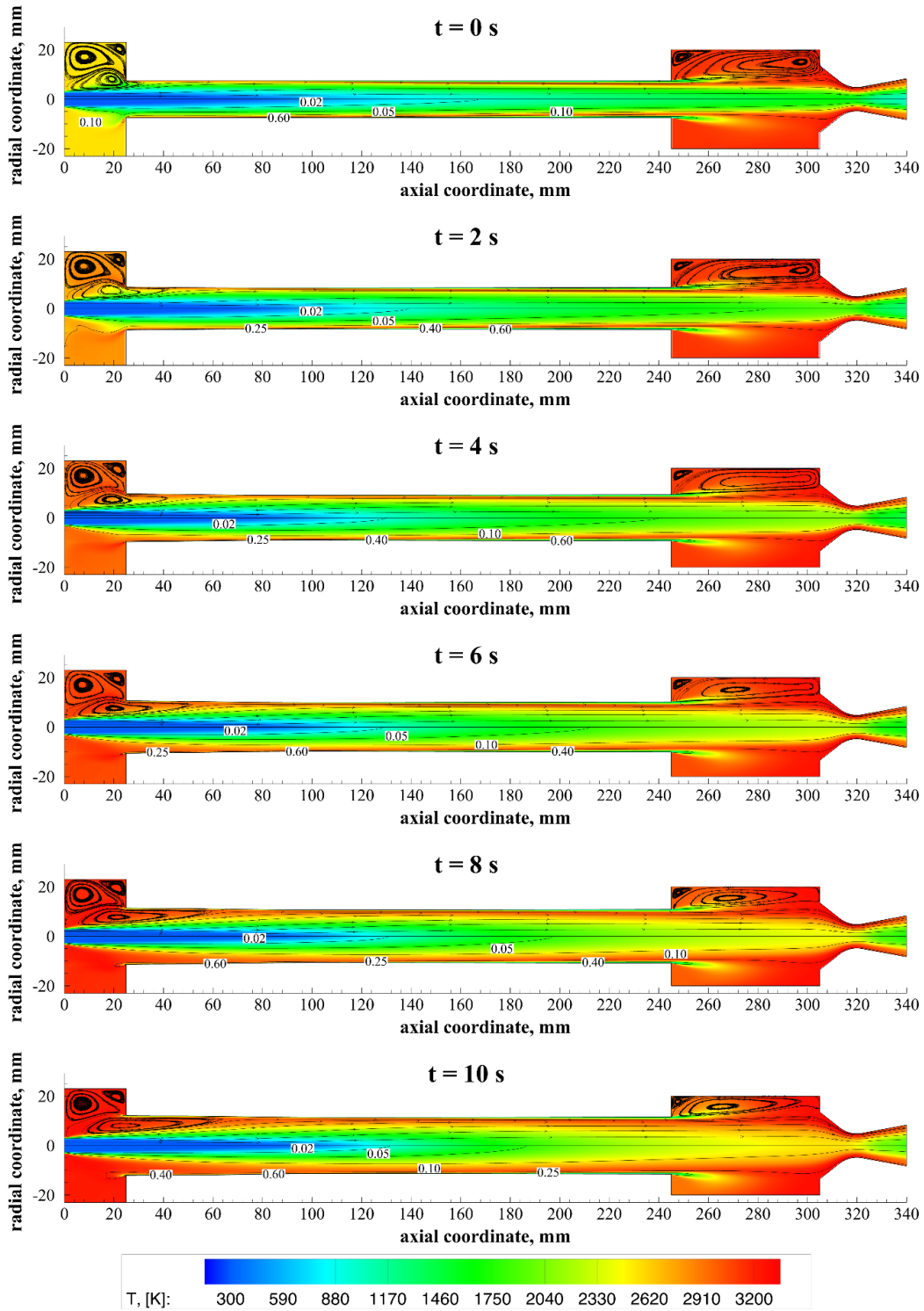
Although numerical simulations performed at the time-space average port diameter in the burn can provide meaningful details of the flowfield in the hybrid rocket combustion chamber and the corresponding average regression rate, a transient simulation is required to compute the fuel consumption distribution at the end of the burn, especially when the regression rate axial profile is uneven and strongly depends on the grain port geometry.

In this section, the results of the transient simulations carried out in the conditions of Test HDPE-1 and Test HDPE-2, presented in Section 3.3.1, are analyzed. Values of oxygen mass flow rate in Table 3.1 are enforced in the calculation. The grain has an initial port diameter equal to 15 mm in Test HDPE-1 and 25 mm in Test HDPE-2, and its geometry is updated in the subsequent time-steps according to the computed regression rate, as described in Section 4.5.

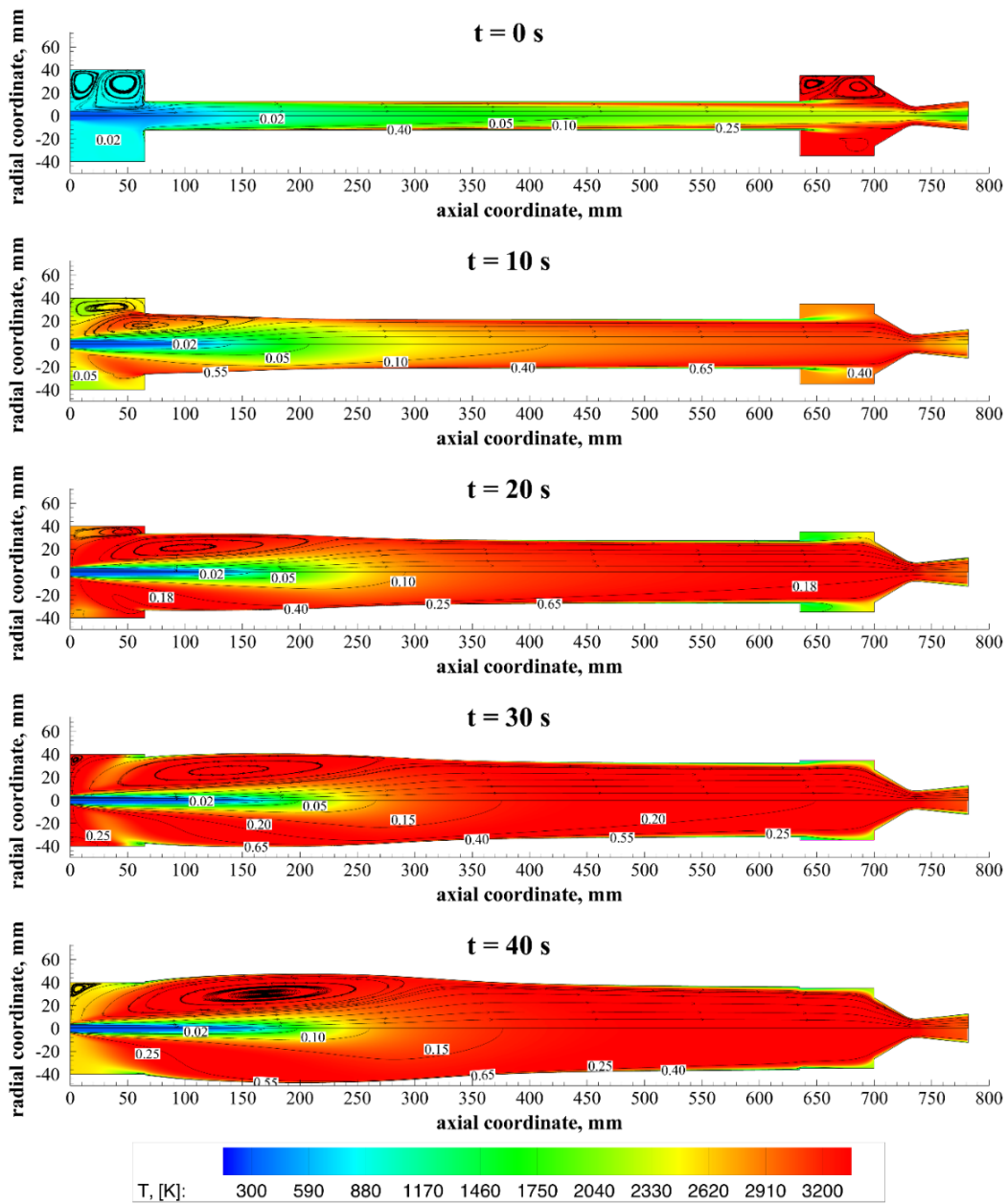
Figure 5.5 shows the plots of temperature contours, with the streamlines overlapped on the top half, and the fuel mass fraction in the unburnt mixture (bottom half), obtained at the different time steps.

First, note that the fluid domain enlarges in time because of the port opening, and it changes shape as well for the non-uniform regression rate, which is clearly evident in Test HDPE-2 (Figure 5.5b). The development of the oxygen jet core in the combustor is not significantly affected by either the oxygen mass flux or the port diameter [37]. In both cases the recirculation region at the motor start up is confined

to the prechamber, while as the port opens up, the oxygen jet impingement point on the fuel wall moves forward and the recirculation region becomes larger.



a) Test HDPE-1



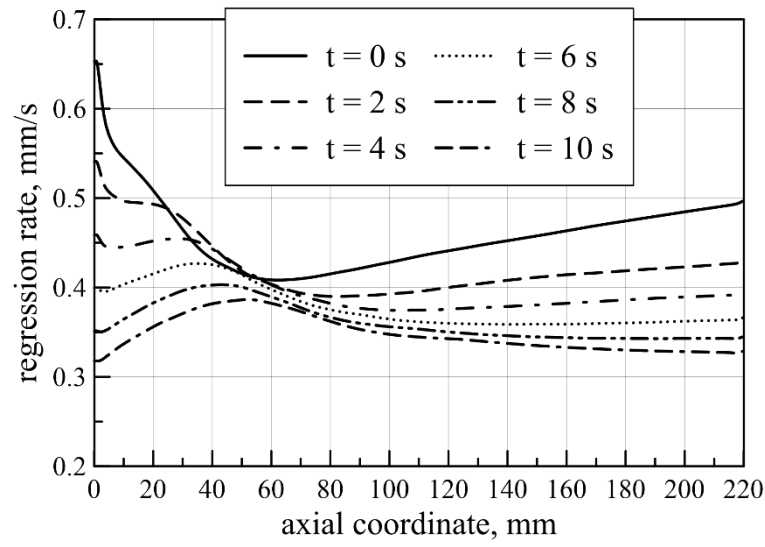
b) Test HDPE-2

Figure 5.5. Temperature contour plot with overlapped streamlines (top half) and mixture fractions isolines (bottom half) at different times.

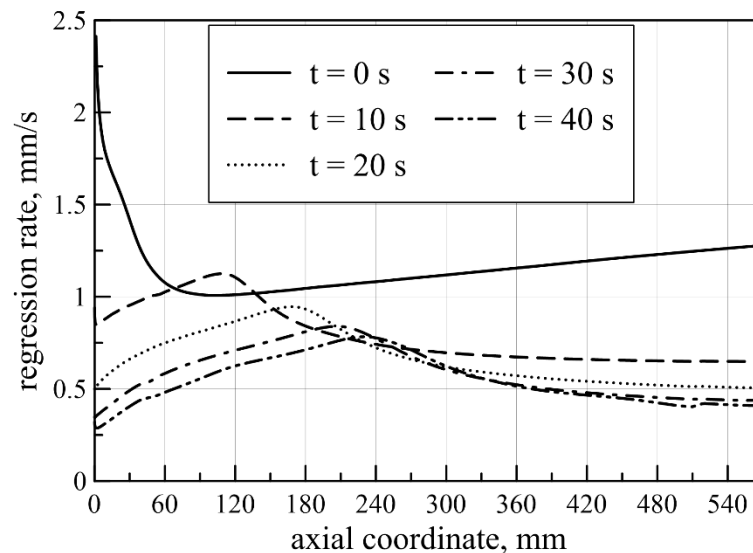
This trend is reflected in the axial profiles of regression rate, shown in Figure 5.6 where it can be noticed that the maximum regression rate point, which is achieved in the impingement region, moves downstream as well, for the recirculation region

enlargement described above. Moreover, because of the mass flux decrease, a reduction of the average regression rate can be observed.

Figure 5.7 shows the evolution of the grain port diameter during the motor run. Fuel consumption in Test HDPE-1 is nearly uniform, except in the port entrance region, whereas Test HDPE-2 yields the typical concave port shape.

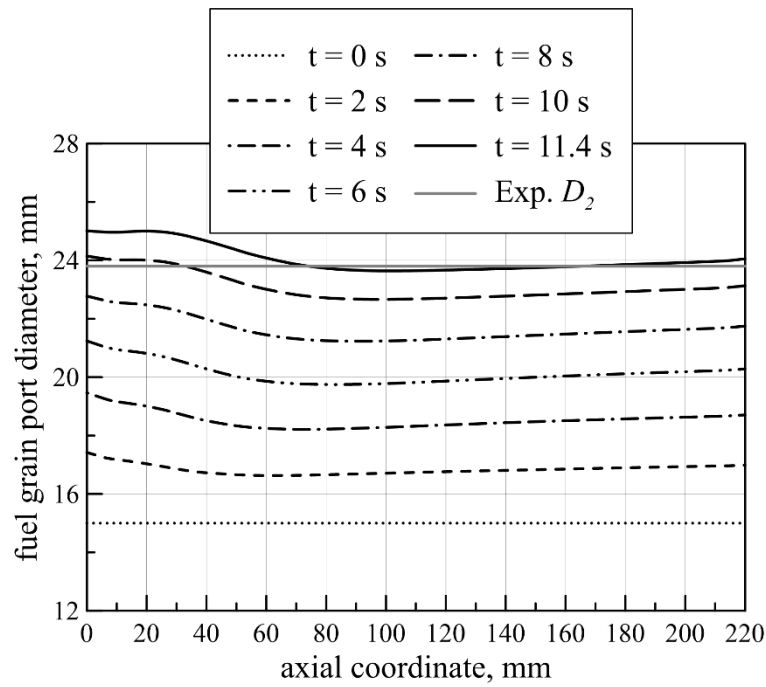


a) Test HDPE-1

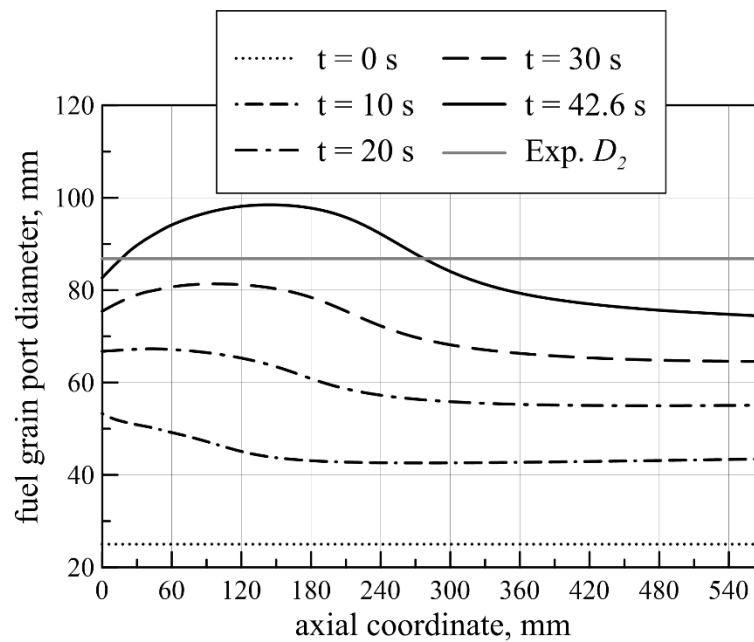


b) Test HDPE-2

Figure 5.6. Regression rate distributions evolution in the firing test.



a) Test HDPE-1



b) Test HDPE-2

Figure 5.7. Fuel-grain port local diameter evolution in the firing test.

The averaged parameters computed with the numerical simulations are summarized in Table 5.3 along with the corresponding deviation with respect to experimental data. A general good agreement between numerical results and experimental data has been obtained, which validates the employed model. The

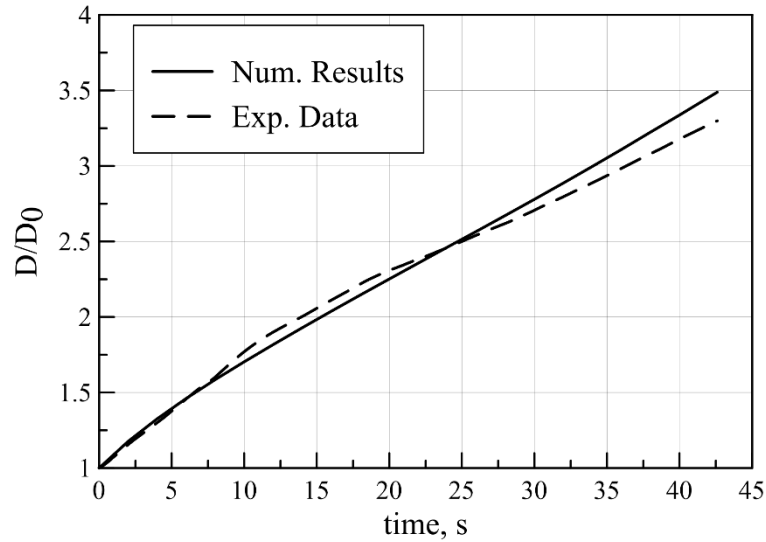
maximum deviation is achieved for the aft-mixing chamber pressure for Test HDPE-2, but it can be explained by the combined effect of the errors in the total mass flow rate and in the overall mixture ratio. In fact, once the comparison is made in terms of the combustion efficiency, better agreement is obtained.

Table 5.3. Computed averaged parameters and deviation with respect to experimental data.

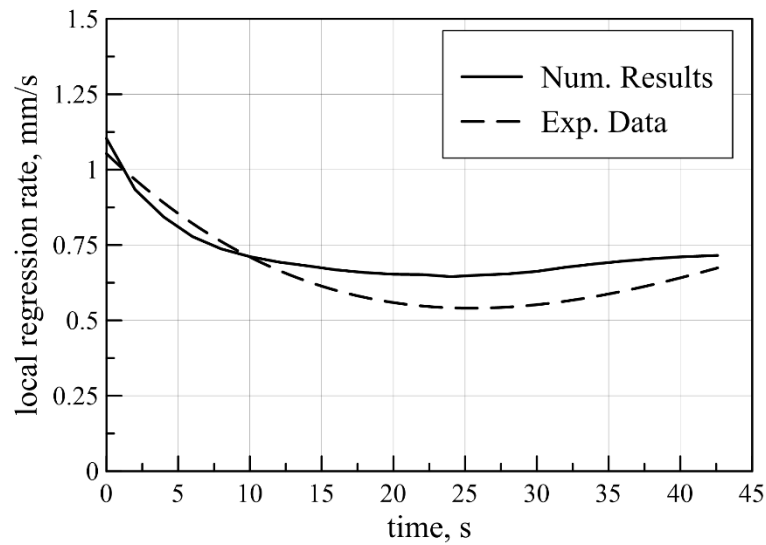
Parameter	Test HDPE-1		Test HDPE-2	
	Numerical results	Relative error wrt experimental data	Numerical results	Relative error wrt experimental data
Postburn space-averaged port diameter, mm	24.34	2.27%	85.78	1.2%
Time-averaged overall mixture ratio	5.60	0.54%	3.20	6.0%
Aft-mixing chamber pressure, bar	6.34	1.15%	22.47	10%
Combustion efficiency	0.942	1.6%	0.952	1.24%

The capability of the numerical model has been further investigated comparing the time resolved regression rate obtained with the ultrasound pulse-echo technique with the numerical results calculated in the position of the ultrasonic transducer, as shown in Figure 5.8. In particular, Figure 5.8a shows the trend of the local grain port diameter, which yields an inflection point changing from a negative to a positive curvature. Of course, this behaviour is directly linked to the local regression rate trend, as shown in Figure 5.8b. The experimental regression rate curve in this case has been obtained numerically differencing the measurement of the local diameter and then smoothing with a polynomial fitting curve. The main feature to be noted is that the regression rate time profile shows a first decreasing trend due to the effect of the port enlargement and the consequently mass flux decrease. Then a change of the slope occurs due to the fact that the impingement region, characterized as seen before by a higher regression rate, approaches the location of the transducer.

In conclusion, although the above described effect is more evident in the experimental curves, the numerical model has been able to capture this behaviour.



a) Normalized local grain port diameter



b) Local regression rate

Figure 5.8. Comparison between the measured and calculated local regression rate for Test HDPE-2.

5.2 Numerical results in the case of liquefying fuels

In this section the results of the numerical simulations of the internal ballistics of hybrid rocket burning liquefying fuels, i.e. performed with the gas/surface interface treatment described in Section 4.4.2, will be presented.

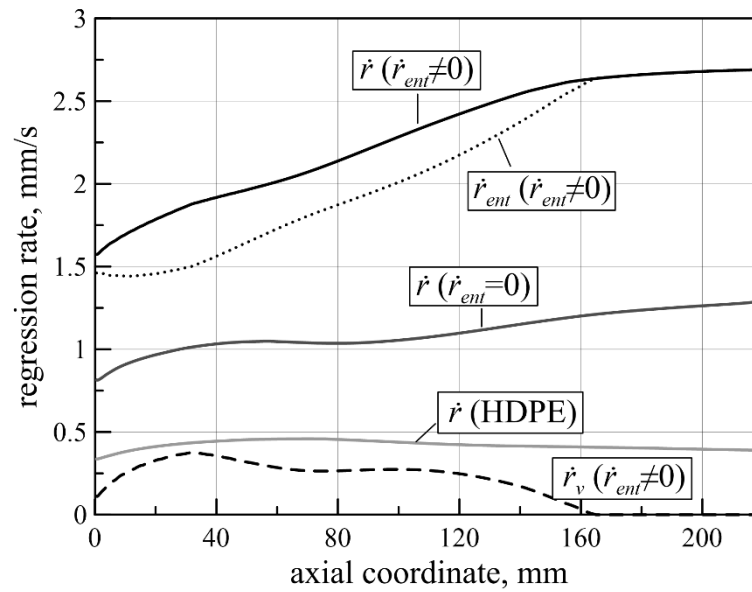
The effect of the additional entrainment component on the total regression rate is considered first. Then, the results of parametric analyses carried out by varying the grain surface temperature and the entrainment parameter are shown highlighting the influence on the two components of the regression rate.

Numerical simulations presented in this section are all performed with the same reference input conditions, i.e. with an oxidizer mass flow rate of 42 g/s and a grain port diameter equal to 27 mm. These values are relative to the operating conditions of the firing Test P-4 (see Section 3.3.2), which yields an intermediate oxidizer mass flux in the range obtained in the experimental tests considered in the present work for the numerical model validation.

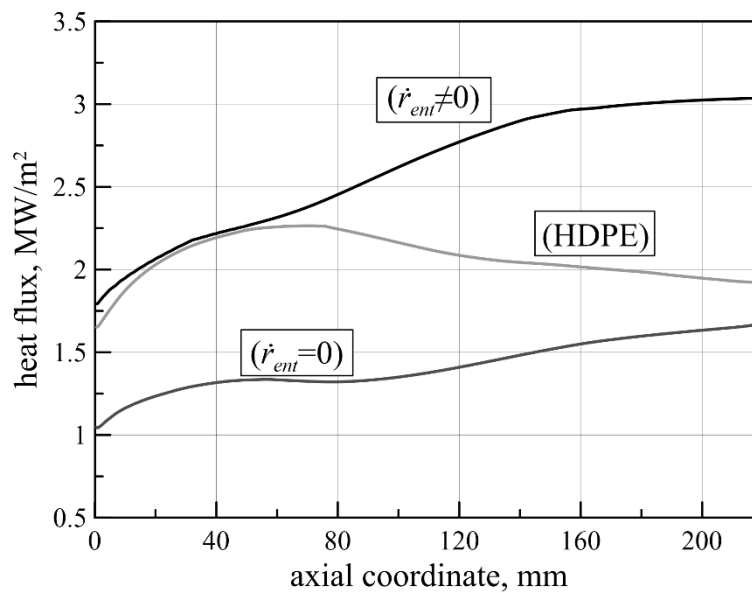
5.2.1 Effect of the additional entrainment regression rate component

First of all, an extreme case is considered in which the entrainment component is assumed to be zero, so that the overall regression rate is only due to vaporization, i.e. $\dot{r} = \dot{r}_v$, (Eq. (4.32) is, thus, not considered), and it is compared to the other case in which also the entrainment term is included in the calculations. The comparison is made considering in both cases the vaporization temperature equal to 675 K (which has been imposed as boundary condition on the grain wall), and the entrainment parameter is assigned equal to $2.1 \cdot 10^{-13} \text{ m}^{8.5} \text{ s}^{0.5} / \text{kg}^3$. It will be shown in the following that these values allow for a good fit of the experimental data for the Test P-4, considered as reference. Finally, the results are compared with that gathered for the case of a HDPE fuel grain, calculated with the numerical model described in Section 4.4.1.

Figure 5.9a shows the fuel regression rates calculated in both cases, and Figure 5.9b the corresponding surface heat fluxes.



a) Regression rate



b) Heat flux to fuel grain surface

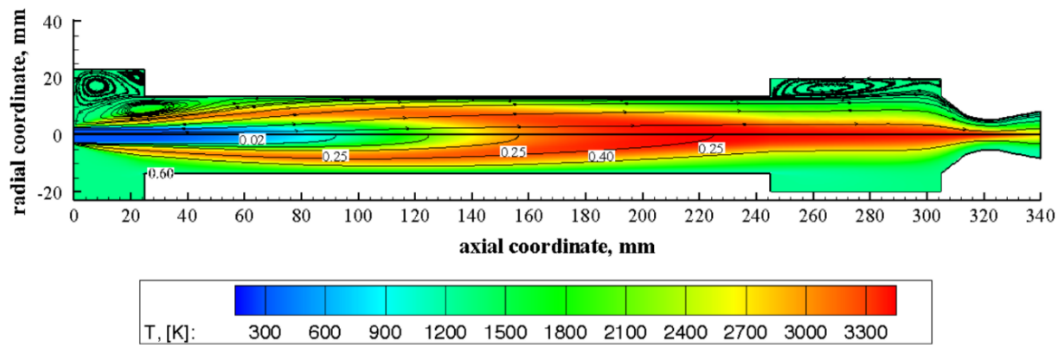
Figure 5.9. Comparison between the results with and without considering the entrainment.

Total regression rate and relevant heat flux have similar axial profiles. It is worth noting that, since the heat requested for pyrolysis is typically larger than that needed for paraffin melting and vaporization (about 5500 kJ/kg against 1400 kJ/kg, respectively), in the first extreme case, without considering the entrainment contribution, the regression rate (see the dark grey continuous line in Figure 5.9a) is

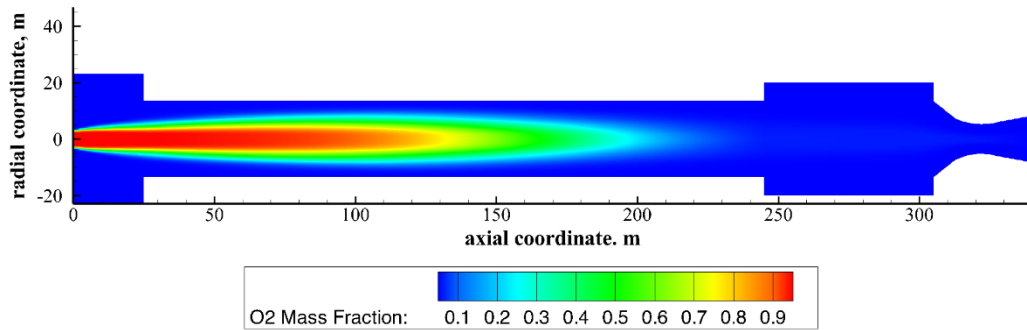
fairly higher compared to the profile obtained with the HDPE fuel (light grey continuous line in Figure 5.9a) at equal oxidizer mass flux, despite the fact that the enhanced blocking effect determines a significantly lower surface heat flux (see Figure 5.9b). However, the spatially-averaged regression rate obtained in this case is equal to 1.11 mm/s, which is still significantly lower than the corresponding measured value of 2.29 mm/s (see Section 3.3.2).

When the entrainment component is taken into account, the calculated regression rate is more than doubled (see the black continuous line in Figure 5.9a) because, with the set of parameters considered here, the most significant contribution is given by the entrainment itself (black dotted line), the vaporization component (black dashed line) being much smaller than the entrainment fraction. With the considerably larger mass flux due to the entrained fuel, as entrainment does not contribute to the heat-transfer blocking, the heat flux is raised, as can be observed in Figure 5.9b (black line). In particular, in the fore end of the grain (up to about 80 mm), where the effect of the mass addition is low, the vaporization regression rate yields values similar to the HDPE regression rate; accordingly, comparable equilibrium conditions between the heat transfer and the mass blowing at the grain wall is obtained, and the heat flux profiles are similar. Whereas, downstream along the fuel grain, for the largely increased mass flux due to the entrainment component, the heat flux to the paraffin fuel surface significantly diverges from that achieved with HDPE.

Figure 5.10 and Figure 5.11 show the two contour maps of the temperatures and O₂ mass fraction calculated with paraffin (considering both vaporization and entrainment) and HDPE. The temperature distribution resembles the typical structure of a diffusion flame. On the top half of the Figure 5.10a and Figure 5.11a the flow streamlines are overlapped, whereas the fuel mass fraction in the unburned mixture isolines are drawn on the bottom half. In both cases, the thermo-fluid dynamic flowfield is similar to that described in Section 5.1.1, with the oxygen jet spreading from the axial injector up to the impingement point on the grain surface and the consequent formation of an extended recirculation zone in the entrance region of the port, which promotes propellant mixing.

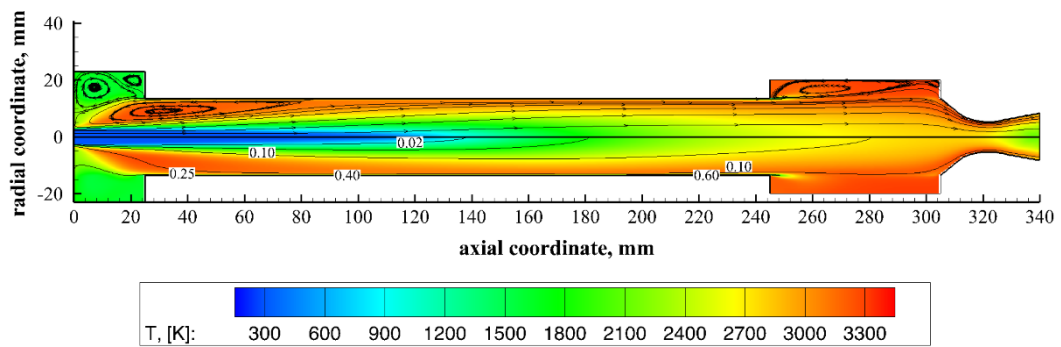


b) Temperature contour plot with overlapped streamlines (top half) and mixture fraction isolines (bottom half)

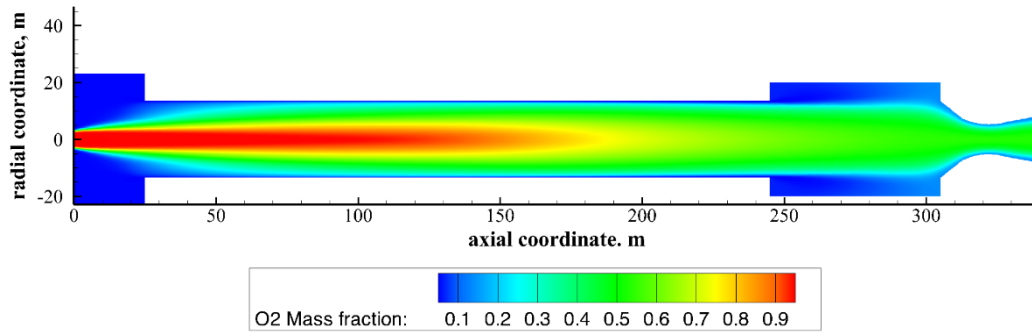


b) O₂ mass fraction contour plot

Figure 5.10 Numerical results in the case of paraffin fuel



a) Temperature contour plot with overlapped streamlines (top half) and mixture fraction isolines (bottom half)



b) O₂ mass fraction contour plot

Figure 5.11. Numerical results in the case of HDPE fuel

It is worth noting that, in the case of paraffin fuel burning, the recirculation region, which is determined by the spreading of the oxygen jet discharged from the injector, is smaller. This seems due to the modeling of entrained paraffin mass that, as mentioned above, is introduced in the port volume; the latter needs to be axially accelerated at the expense of the oxygen jet momentum, which decreases and causes larger jet spreading. For the same reason, the hottest region in the flowfield of HDPE grain port is attained close to the grain surface and a high oxygen concentration characterizes the core region, whereas, because of the significant fuel mass addition largely due to the entrainment, in the paraffin-fuel port it rapidly extends into the core flow and the oxygen is completely burned in the post-chamber.

5.2.2 Grid sensitivity analysis

In order to assess the numerical results shown in the previous section and in the following, a grid sensitivity analysis is carried with three mesh refinement levels.

In the reference mesh the pre-chamber is subdivided into 40×80 grid cells in the axial and radial directions, respectively, the grain port in 240×40 grid cells, the post-chamber in 80×80 cells and the nozzle in 60×40 cells. Also in this case, cells are clustered towards the grain wall in such a way to ensure that the maximum value of y^+ is around 2÷3 at the wall-adjacent cell all along the grain length. Additional axial clustering of cells is placed in the regions near the grain inlet and outlet edges, and near the pre-chamber, post-chamber and nozzle inner surfaces.

Similarly to what done in Sec. 5.1.2 for the case of pyrolyzing fuels, the coarser mesh is constructed doubling the size of the cells in both the axial and the radial directions compared to the reference mesh, while the finer mesh was realized halving the cell size in both directions.

Figure 5.12 shows a log-log plot of the numerical error, estimated as described in Sec. 5.1.2, versus the grid size for the average values of the total regression rate and its components, summarized in Table 5.4. Again, spatial convergence study is carried out determining the discretization error of the CFD simulations according to the methods presented in [75]. The maximum deviation is obtained for the vaporization regression rate component, which anyway reduces to around 3% with the reference mesh. For the total regression rate and the entrainment components the deviations with the reference mesh are much smaller than 1%. Therefore, it can be stated that a satisfying convergence of the numerical results is obtained with the reference mesh.

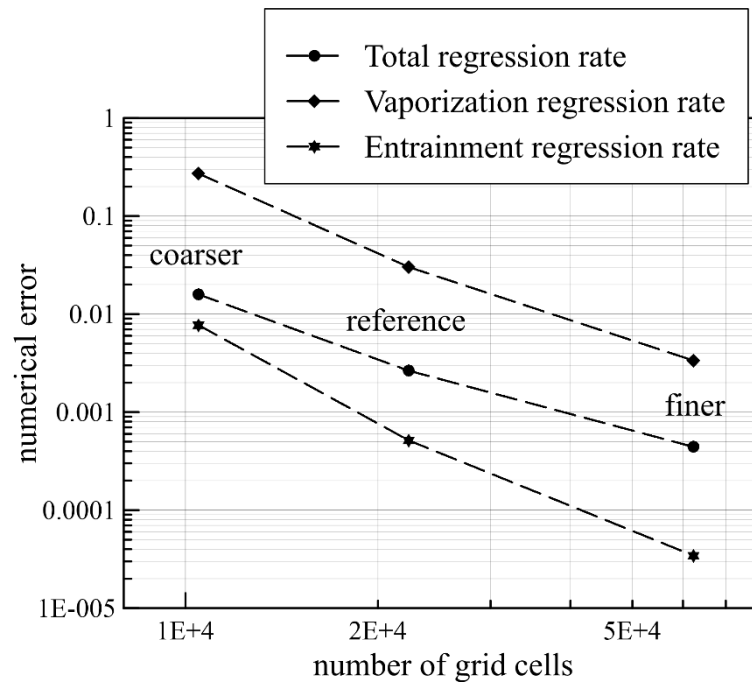


Figure 5.12. Numerical error versus grid size.

Table 5.4. Results of grid sensitivity analysis on the spatially averaged regression

rate components.

Mesh	Total regression rate, mm/s	Vaporization regression rate, mm/s	Entrainment regression rate, mm/s
Coarser	2.302	0.237	2.065
Reference	2.272	0.192	2.080
Finer	2.267	0.188	2.079

5.2.3 Effect of vaporization temperature and entrainment parameter

In this section the results of two parametric analyses performed by varying first the vaporization temperature, and then the entrainment parameter, are presented.

Figure 5.13 shows the axial profiles of the regression rate and its two components obtained with two different values of the vaporization temperature, 675 and 725 K; the entrainment parameter used in the calculations is equal to $2.1 \cdot 10^{-13} \text{ m}^{8.5} \text{ s}^{0.5} / \text{kg}^3$. According to the fact that the vaporization temperature mostly influences the term $C_l(T_v - T_m)$ appearing in Eq. (4.31), the main effect of vaporization temperature is on the vaporization component of regression rate, whereas the entrainment component is practically not affected; therefore the percent change of total regression rate with temperature is equal to that of the vaporization component. In particular, the larger vaporization temperature yields the lower fuel vaporization and total regression rate, whereas the entrainment component is almost unchanged up to the point in which the vaporization component vanishes, then it follows the trend of the total regression rate.

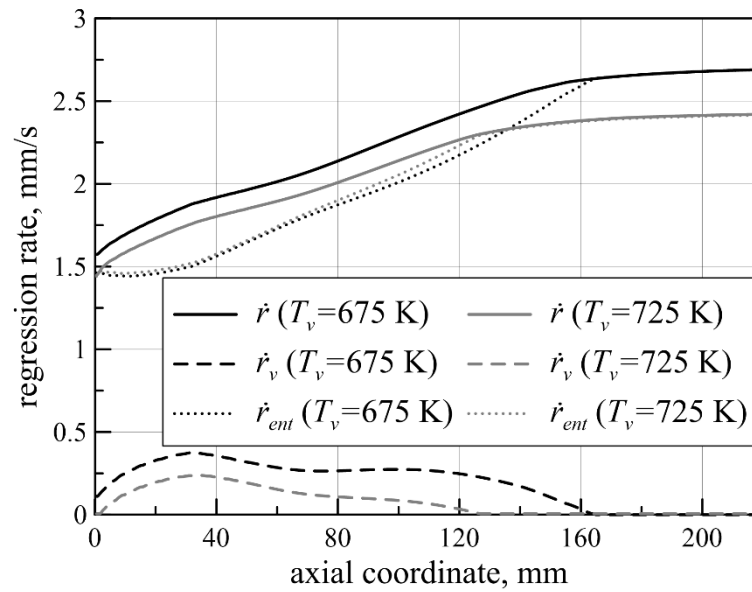


Figure 5.13. Effect of the vaporization temperature on the axial profiles of the regression rate and its components.

The influence of the entrainment parameter is shown in Figure 5.14 from which it can be seen that the primary effect is on the entrainment component of regression rate. This result was of course expected since the entrainment parameter directly enters the entrainment regression rate fraction through Eq. (4.32). Thus, higher the entrainment parameter is, larger entrainment is produced (see dotted lines in Figure 5.14). Recalling that the entrainment parameter is inversely proportional to the fuel liquid viscosity (Eq. (4.33)), lower a_{ent} means higher viscosity, which implies a more effective stabilization of the fuel surface melt layer, and smaller mechanical transfer of liquid droplets, resulting in lower entrainment. Note that, as the entrainment parameter has not a direct influence on the heat flux to the fuel surface, the decrease of the entrainment regression rate causes an opposite change in the vaporization fraction (dotted lines in Figure 5.14). This behaviour affects the balance between the energy transfer to the wall and the blocking phenomenon caused by the blowing of the gasified fuel, and a new equilibrium condition is established. As the blowing is raised for the vaporization increase, also the heat transfer blocking is larger, and the result is that the overall regression rate is smaller (continuous lines in Figure 5.14).

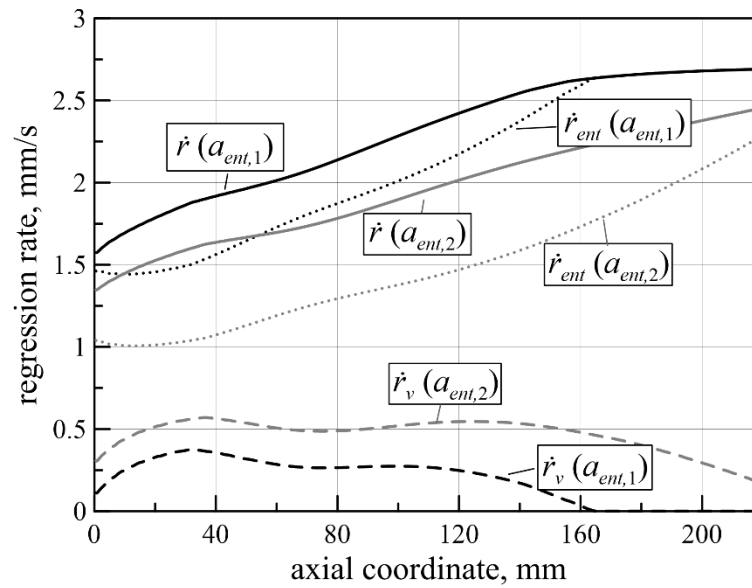


Figure 5.14. Effect of the entrainment parameter on the axial profiles of the regression rate and its components.

A summary of the average regression rate obtained by varying the vaporization temperature and the entrainment parameter is represented in Table 5.5. As the measured average regression rate in Test P-4 is 2.29 mm/s, 675 K and $2.1 \cdot 10^{-13} \text{ m}^{8.5} \text{ s}^{0.5} / \text{kg}^3$ are, therefore, the values leading to the best prediction of the experimental data, and they are used in all the simulations discussed in the following.

Table 5.5. Vaporization temperature and entrainment parameter effect on the average regression rate.

Computational case(*)	Total regression rate, mm/s	Vaporization regression rate, mm/s	Entrainment regression rate, mm/s
$T_{v1} \quad a_{ent,1}$	2.272	0.192	2.080
$T_{v2} \quad a_{ent,1}$	2.114	0.073	2.041
$T_{v1} \quad a_{ent,2}$	1.957	0.453	1.504

(*) $T_{v1} = 675 \text{ K}$; $T_{v2} = 725 \text{ K}$; $a_{ent,1} = 2.1 \cdot 10^{-13} \text{ m}^{8.5} \text{ s}^{0.5} \text{ kg}^{-3}$, $a_{ent,2} = 1.1 \cdot 10^{-13} \text{ m}^{8.5} \text{ s}^{0.5} \text{ kg}^{-3}$

5.2.4 Comparison between numerical results and experimental data

The model discussed above is applied to the simulation of the flowfield for the test cases presented in Section 3.3.2, carrying out numerical simulations with the oxygen mass flow rate and the average grain port diameter reported in Table 3.2.

Note that, as pointed out in Ref. [37], the time-and-spatially averaged regression rate obtained through simulations conducted at different grain geometries (each corresponding to a specific stage in the burn), thanks to the employed mass flux averaging definition [81], deviates by only a few percent from the spatially averaged regression rate calculated with a single simulation at the average port diameter. In support of this statement in Figure 5.15 the axial profile of the calculated regression rate in Test 4 is compared with the post-burn measured one.

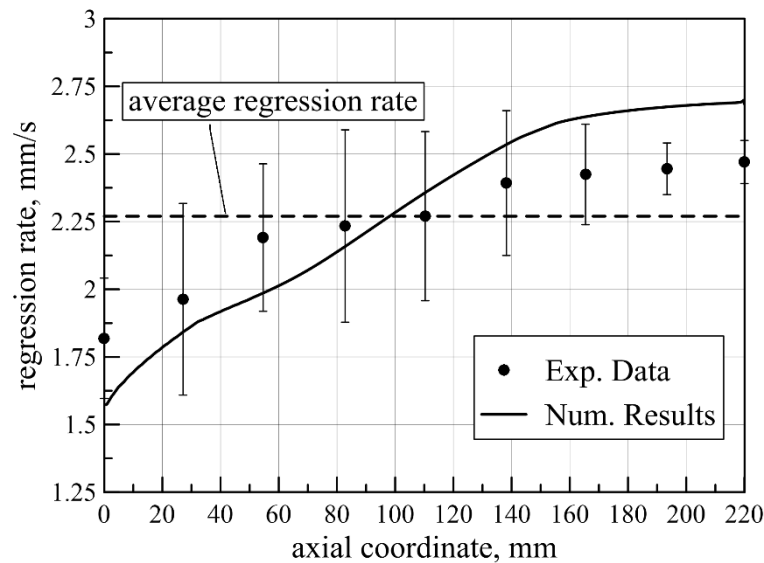


Figure 5.15. Regression rate axial profile (Test 4): comparison between numerical results and experimental data.

The regression rate profile calculated at the average port diameter in the burn is within the measurement uncertainty except at the grain exit portion. Note that the experimental uncertainty is much larger in the grain fore region because of the unburned recirculated melted paraffin (see Figure 5.11a) which is deposited on the

grain surface after the motor extinguishment by means of high-pressure nitrogen injection.

In all the test cases the vaporization temperature has been set equal to 675 K, whereas the entrainment parameter has been varied by scaling the reference value of $2.1 \times 10^{-13} \text{ m}^{8.5} \text{ s}^{0.5} / \text{kg}^3$, identified for the best fit of the experimental data of Test 4, with the ratio $(\rho_g^* / \rho_g)^{1.5}$, where ρ_g^* is the average gas density in the grain port calculated in Test 4, and ρ_g is the corresponding value calculated in the analysed test case. This allows considering the dependence of the entrainment parameter on the average gas density as prescribed by Eq. (4.33).

Figure 5.16 shows the calculated average fuel regression rates along the grain compared with the measured time-space averaged ones as a function of the oxidizer mass flux; the percent deviations between the numerically computed values and the experimental data are listed in Table 5.6. The experimental regression rates have been obtained with the fuel mass-loss method (see Section 3.2) starting from the measurement of the burned fuel mass and burning time. The maximum deviation of 11% is reached at the minimum mass flux; numerical prediction improves with higher mass fluxes showing excellent agreement at the largest mass fluxes where the deviation is only 0.3%, still lower than that achieved at the reference Test 4. This behaviour makes the regression-rate mass flux trends to converge as shown by the trendlines in Figure 5.16.

The displayed deviation trend can be explained observing that the critical pressure of paraffin wax is 6.5 bar and that the chamber pressure attained in the test with the largest error is lower than the critical pressure (see Table 5.6). Below the critical pressure, neglecting the effects of the entrained liquid paraffin dynamics is a much less suitable assumption. The agreement with experiments is improved as pressure increases with the mass flux.

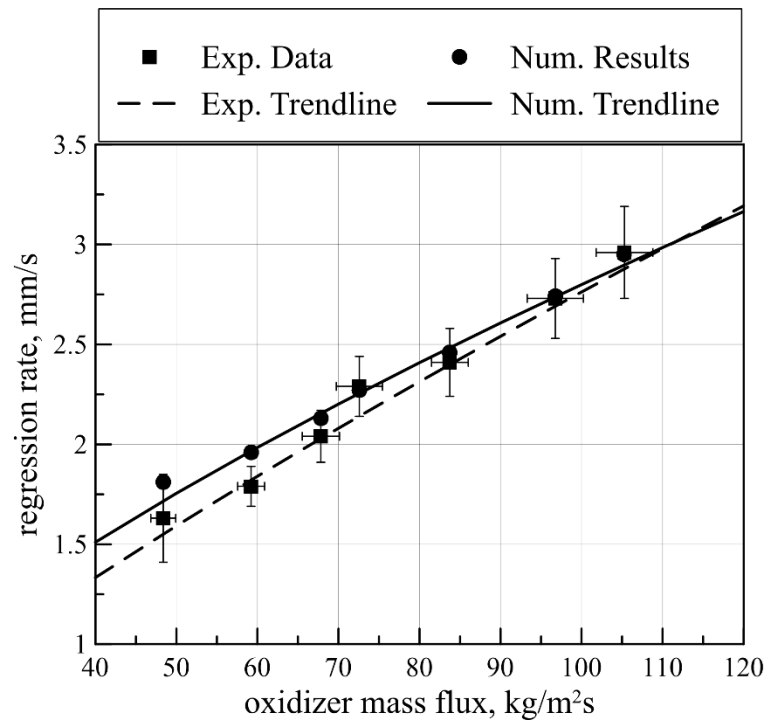


Figure 5.16. Comparison between numerical results and experimental data in terms of average regression rate as a function of the oxidizer mass flux.

Table 5.6. Computed regression rate deviations from experimental data.

Test ID	Calculated space-averaged regression rate, mm/s	Error relative to experimental data
P-1	1.81	11.0%
P-2	1.96	9.5%
P-3	2.13	4.4%
P-4	2.27	-0.9%
P-5	2.46	2.1%
P-6	2.74	0.3%
P-7	2.95	-0.3%

CHAPTER 6. CHARACTERIZATION OF UHTCMC IN HYBRID ROCKET PROPULSION ENVIRONMENT

6.1 Design of prototypes and experimental setup

As mentioned before, in the framework of the C³HARME European research project, experimental and numerical activities have been carried out and are currently ongoing for the characterization of new UHTCMC materials for propulsive applications. For this purpose, novel, dedicated test set-up were developed to test the new materials following an incremental approach, starting from small sample and increasing the complexity up to full scale components to be tested in representative environments.

6.1.1 Experimental setup for free-jet test

The first step of these activities consists in testing small, button-like samples, with maximum diameter of 17mm (Figure 6.1) in representative conditions in terms of combustion temperature over 3000 K, supersonic Mach number and stagnation pressure. This kind of test allows in a relatively fast and low-cost way to have a first evaluation of the ability of the specimens to preserve their functional integrity in a relevant environment, hence supporting the selection of the most promising materials compositions for realizing more complex prototypes for the next steps of the research.

For this purpose, the facility has been upgraded to allow performing tests placing the specimen downstream of the hybrid rocket engine, in order to be reached by the exhaust plume coming from the nozzle.

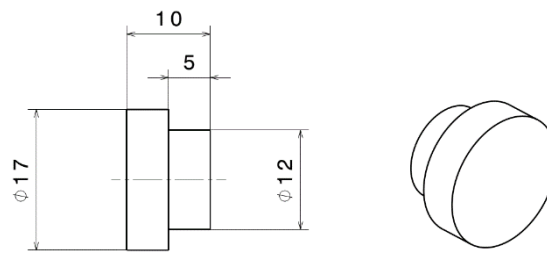


Figure 6.1. Nominal design of UHTCMC samples for free jet tests. Dimensions are in mm.

The experimental set-up consists of a mechanical system connected to the test bench in order to support and keep the specimen aligned with the motor axis. This system is designed to place the test article at the desired distance to the nozzle exit. In the present test campaign, a distance of 15 cm was selected. Figure 6.2 shows the experimental set-up, including the non-intrusive diagnostic equipment employed for the real-time evaluation of the sample surface temperature.

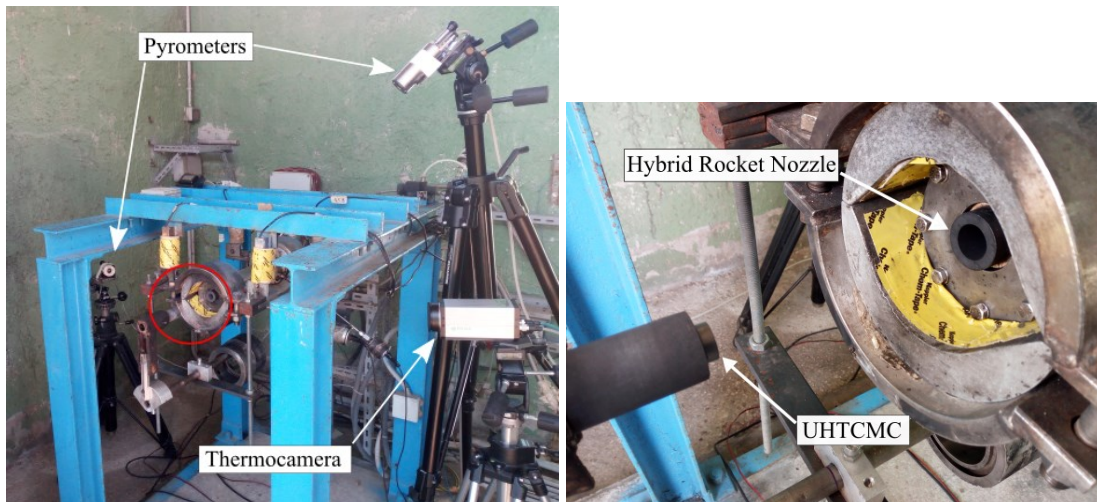


Figure 6.2. Set-up for free-jet test. The area within the red circle in the left picture is zoomed in the right picture.

In particular, the surface temperature of the samples can be continuously measured ($\pm 1\%$ instrumental accuracy) by digital two-colour pyrometers (Infratherm ISQ5 and IGAR6, Impac Electronic GmbH, Germany) at an acquisition rate of 100 Hz. In addition, the infrared response of the specimen during the free-jet testing can be obtained by means of an infrared (IR) thermo-camera (TC, Pyroview 512N, DIAS

Infrared GmbH, Germany). The two-colour ISQ5 pyrometer exploits two overlapping infrared wavelength bands at 0.7–1.15 μm and 0.97–1.15 μm to measure the temperature from 1273 K up to 3273 K. The IGAR6 pyrometer operates in the bands 1.5-1.6 μm and 2.0-2.5 μm to return the sample temperature in the range 523-2273 K. The two pyrometers gave similar responses, so only the temperature profiles measured by ISQ5 are herein reported. The pyrometers mode can be set in order to give back the peak value of the temperature field detected inside the measurement area, consisting in a round spot of 3.3 mm in diameter. In addition, the so-called “two-colour mode” provides an output value independent on the (directional) spectral emittance. It is generally assumed that the observed surface behaves as a grey body over the operating temperature range. Surface chemical reactions occurring during test can be responsible for changes in emittance versus testing time. On one hand, the two-colour pyrometers overcome this problem measuring the true temperature. On the other hand, the IR-TC detects the spectral radiance coming out from the heated sample along the infrared band wavelengths of 0.8-1.1 μm . The surface temperature distribution can be calculated assuming constant emissivity along the monitored surfaces of the samples and taking into account the axial symmetry of the specimens. Once the local temperature is measured thanks to the pyrometer at the measurement spot, that value is input to determine the spectral emittance in the range of the IR-TC, and finally the surface temperature distribution is evaluated.

6.1.2 Setup for test of nozzle throat inserts

In the second step of the experimental characterization of the UHTCMCs, the graphite nozzle usually employed in the firing test is replaced by a segmented-designed nozzle having the outer parts, namely the converging and diverging conical elements, made of graphite, while the restricted region around the throat is made of the new materials to be tested (Figure 6.3). This configuration allows to manufacture relatively small prototypes, gradually increasing the geometric complexity, and to test them to most severe conditions in terms of shear stresses and heat fluxes, which are encountered right in the nozzle throat region.

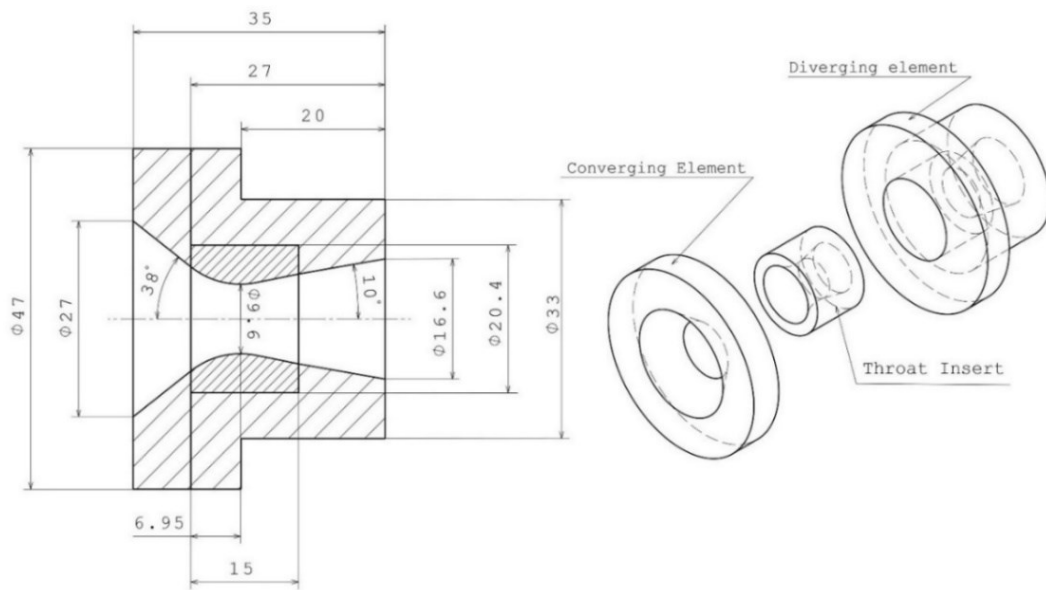


Figure 6.3. Design of segmented nozzle with UHTCMC nozzle throat insert.
Dimensions are in mm.

Samples and nozzle insert external surfaces were observed before and after the test by a Digital Microscope KH-8700 (HIROX-USA, Inc., United States), employing a MX(G) 5040SZ optical lens with 50-400x magnification factor. These were also measured by a digital caliper (0.01 mm accuracy).

Future activities are foreseen on nozzle completely made of the new UHTCMCs.

6.2 Numerical models for the characterization of the flowfield around test articles

In this section the models for the numerical simulations of the thermo-fluid dynamic flow field inside the combustion chamber and through the nozzle of hybrid rocket engines and for the evaluation of the operating conditions around the test article are described.

As the major focus in this part of the work has been dedicated to the experimental activities for the characterization of the new-class materials behaviour when exposed to the harsh combusting environment typical of hybrid rockets, simplified numerical

models have been employed in this phase as a relatively low-computational-cost support to the experimental tests in order to get additional information, that are difficult to collect experimentally, about the operating conditions corresponding to the different selected test conditions.

Anyway, the numerical results described in the following represents also the basis for the future research activities, aimed at developing the numerical models coupling them with the results obtained with the simulations of the hybrid rocket internal ballistics described in the previous chapters and extending the iterative loose-coupled treatment for the interaction between the gaseous combusting flow and the material surface with the aim of getting a deeper insight on the phenomena involved in the material oxidation and erosion.

6.2.1 One-dimensional model for chamber and nozzle conditions simulation

A one-dimensional model based on NASA CEA software can be used to rapidly evaluate the evolution of the operating conditions in the combustion chamber, in particular the chamber pressure, and through the nozzle during the time. In this case, the input of the model are the oxidizer mass flow rate, the geometrical dimensions of the fuel grain and the operating time.

As the instantaneous regression rate is an unknown parameter and the oxidizer mass flux and chamber pressure depend on the regression rate itself, the expected data are estimated assuming the classical regression rate law

$$\dot{r} = aG_{ox}^n \quad (6.1)$$

where the coefficient a and n have been selected from the values available in literature relevant to the combustion of gaseous oxygen with HDPE fuel grains [81]. Integrating Eq. (1) in time, the instantaneous port diameter $D(t)$ can be calculated. Then, considering the prescribed oxidizer mass flow rate, the corresponding mass flux $G_{ox}(t)$ and regression rate $\dot{r}(t)$ can be estimated. Then the fuel mass flow rate can be easily calculated as

$$\dot{m}_f(t) = \rho_f \pi D(t) L \dot{r}(t) \quad (6.2)$$

where ρ_f is the solid fuel density and L is the length of the grain, and correspondingly the average mixture ratio $OF(t) = \frac{\dot{m}_{ox}}{\dot{m}_f(t)}$ can be derived. From these calculations, the estimation of the aft-chamber pressure p_c can be performed by means of an iterative procedure to solve the steady-state mass balance equation

$$\frac{\dot{m}_{ox}}{A_t} \left(1 + \frac{1}{OF}\right) = \frac{p_c}{\eta C^*} \quad (6.3)$$

in which A_t is the nozzle throat area, C^* is the theoretical characteristic exhaust velocity (that primarily depends on the mixture ratio and, to a minor degree, on pressure) and the combustion efficiency, η , has been assumed equal to unity. For the dependence of the C^* on pressure, Eq. (3) is implicit and an iterative calculation technique is needed. A combustion pressure is first assumed, then the CEA code [65] is run to calculate the equilibrium composition and the theoretical exhaust velocity, assuming frozen flow through the nozzle, at the given OF ratio in input. Finally, combustion pressure is adjusted repeatedly until convergence.

6.2.2 CFD model for the simulation of the flow field around test articles

In order to provide a better understanding of test conditions around the material samples and prototypes, CFD simulation of the flow through the rocket nozzle and of the external plume of the exhaust gases are performed, employing as boundary conditions the time-averaged results of the numerical tool described in the previous section.

To this purpose the RANS equations for single-phase multicomponent turbulent reacting flows are solved with a control-volume-based technique and a density-based algorithm, employing the SST $k-\omega$ model as turbulence closure. However, with

respect to the models described in Section 4.2, a different model is preferable for the chemical species transport and reaction mechanism, as the chemical equilibrium hypothesis is no longer applicable for an accurate analysis of the fast accelerating flow through the nozzle and downstream of it. In fact, although the assumption of chemical equilibrium does not influence significantly the estimation of the chamber pressure and of the engine performance, it can affect the correct prediction of the chemical composition evolution and of the heat transfer to the wall. Accordingly, in this case the transport equations for the main combustion products (O_2 , C_2H_4 , H_2O , CO_2 , CO , H_2 , H , O , OH are the species considered in the current model, together with the non-reacting N_2) are solved, and the Eddy Dissipation Concept (EDC) model is employed for the combustion mechanism, which accounts for detailed chemical reaction rates in turbulent flows. Consequently, the Arrhenius rate K for each reaction is calculated as

$$K = A_K T^\beta \exp\left(-\frac{E_a}{RT}\right) \quad (6.4)$$

where the constants have been taken from Ref. [84] and are reported in Table 6.1.

Table 6.1. $C_2H_4 - O_2$ reaction system.

No.	Reaction ^a	A_K ^b	β	E_a ^b
1	$C_2H_4 + O_2 \rightleftharpoons 2CO + 2H_2$	1.80e+14	0.0	35500
2	$CO + O \rightleftharpoons CO_2 + M$	5.30e+13	0.0	-4540
3	$CO + OH \rightleftharpoons CO_2 + M$	4.40e+06	1.5	-740
4	$H_2 + O_2 \rightleftharpoons OH + OH$	1.70e+13	0.0	48000
5	$H + O_2 \rightleftharpoons OH + O$	2.60e+14	0.0	16800
6	$OH + H_2 \rightleftharpoons H_2O + H$	2.20e+13	0.0	5150
7	$O + H_2 \rightleftharpoons OH + H$	1.80e+10	1.0	8900
8	$OH + OH \rightleftharpoons H_2O + O$	6.30e+13	0.0	1090
9	$H + H \rightleftharpoons H_2 + M$	6.40e+17	-1.0	0
10	$H + OH \rightleftharpoons H_2O + M$	2.2e+22	-2.0	0

^aThird-body efficiencies for all thermomolecular reactions are 2.5 for $M = H_2$, 16 for $M = H_2O$, and 1 for all other M .

^bUnits are in seconds, moles, cubic centimeters, calories and Kelvin.

The Discrete Ordinates model for the radiation is included in the numerical modelling.

The computational grid used for the simulation of the free reacting jet exiting from the nozzle is shown in Figure 6.4. A supersonic inflow boundary condition is set on the surface representative of the nozzle exit section, imposing the total pressure and the total temperature corresponding to the operating chamber pressure and temperature in the rocket and the static pressure and the chemical composition at the exit of the nozzle. The ambient pressure is set on the other external boundaries of the computational domain.

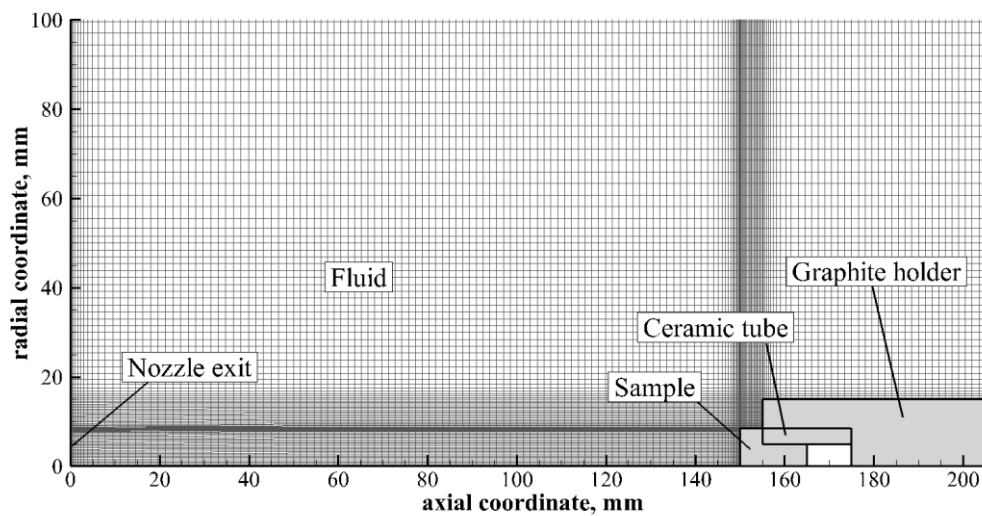


Figure 6.4. Computational grid for the simulation of the free reacting jet exiting from the rocket nozzle.

The typical computational grid for the simulation of the flowfield through the exhaust nozzle of the hybrid rocket is shown in Figure 6.5. Similarly to what described above, a pressure inlet boundary condition is set on the inlet section of the nozzle imposing the time-averaged values of the total pressure, the total temperature and the chemical composition estimated by means of the model described in the previous section. A supersonic outlet condition is set at the exit section.

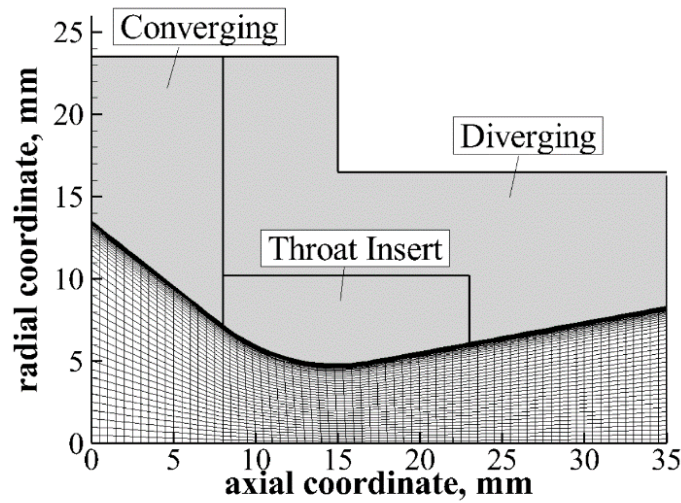


Figure 6.5. Computational grid for the simulation of the flow through the rocket nozzle.

6.3 Experimental characterization of UHTCMC samples in free jet conditions

As explained before, the first step of the characterization of the new UHTCMC materials foresees testing of small samples exposed to the free jet of the exhaust gases coming from the hybrid rocket nozzle. In this section, first the samples tested in this experimental campaign will be presented, then the test conditions will be described and finally the experimental results, in terms of the erosion behaviour and of the samples thermal histories, will be discussed.

6.3.1 UHTCMC samples

Five UHTCMC samples were manufactured and tested, which are summarized in Table 6.2. All of them were based on a UHTC matrix with carbon fibers.

In particular, two samples had a Ti_3SiC_2 matrix with short (chopped) carbon fibers, uniformly dispersed into the matrix, and are referred to as TSC-SF.

The other samples had the matrix based on ZrB_2 as major component and SiC as a minority phase. Two of them had long continuous carbon fibers, with a $0^\circ/90^\circ$ plies architecture, while the others had chopped fibers uniformly dispersed into the matrix.

Table 6.2. UHTCMC samples for free jet test.

UHTCMC sample ID	Matrix composition	Carbon fibers
TSC-SF-1	Ti_3SiC_2	Chopped
TSC-SF-2	Ti_3SiC_2	Chopped
ZBSC-SF-1	ZrB_2/SiC	Chopped
ZBSC-LF-1	ZrB_2/SiC	Continuous Unidirectional
ZBSC-LF-2	ZrB_2/SiC	Continuous Unidirectional

6.3.2 Test conditions

Two different test conditions, which mainly differ for the oxidizer mass flow rates, have been selected, to evaluate the materials performance in different aero-thermo-chemical environments. All tests had a nominal duration of 10 s. Cylindrical 220mm-long HDPE grains were employed as fuel and gaseous oxygen as oxidizer. Table 6.3 summarizes the main nominal operating parameters of the test conditions, as estimated by means of the one-dimensional tool described in Section 6.2.1.

Table 6.3. Nominal test conditions for free jet tests.

	Test condition 1FJ	Test condition 2FJ
Oxidizer mass flow rate [g/s]	25	40
Oxidizer-to-Fuel ratio	5.13	6.50
Chamber pressure [bar]	6.49	5.65
Combustion temperature [K]	~ 3200	~ 3200
Nozzle exit pressure [bar]	0.42	0.46
Nozzle exit temperature [K]	~ 2200	~ 2200
Nozzle exit Mach number	2.4	2.25
Nozzle exit CO_2 mass fraction	0.36	0.34
Nozzle exit H_2O mass fraction	0.17	0.14
Nozzle exit O_2 mass fraction	0.30	0.41

Test condition 1FJ has been estimated considering the employment of a nozzle with a throat diameter equal to 9.6 mm. On the other side, for Test condition 2FJ nozzle with a throat diameter equal to 12.5 mm has been employed in order to have similar values of the chamber pressure with respect to Test conditions 1FJ, with a higher average oxidizer-to-fuel ratio, i.e. a more oxidizing chemical environment, with respect to the former two conditions.

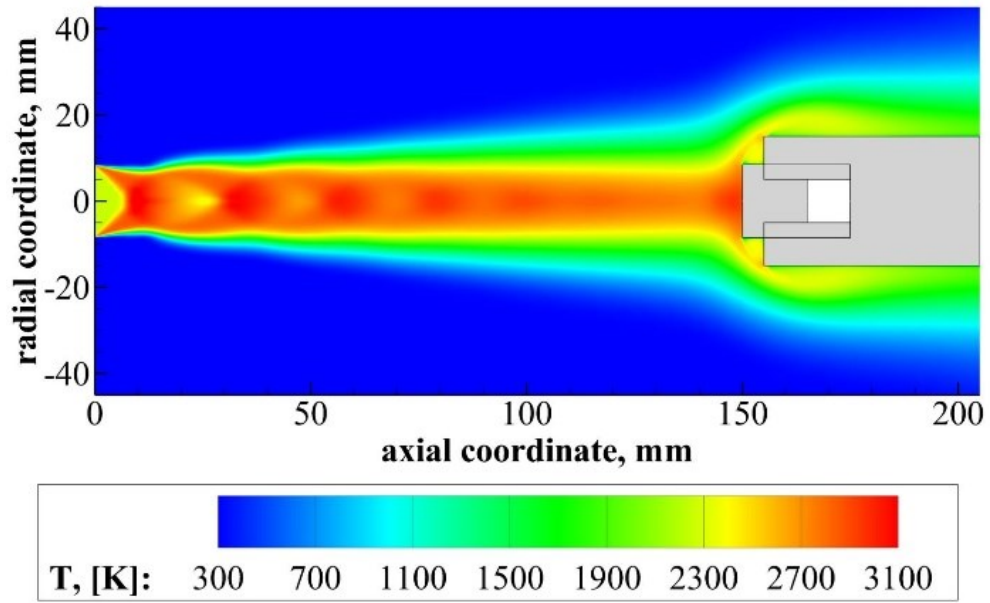
Additional significant information on the operating conditions around the samples can be obtained from the CFD simulations carried out with the models described in Section 6.2.2.

Figure 6.6 and Figure 6.7 show the distributions of temperature and molecular oxygen mass fraction, respectively, in the flow field of the free jet test, for the two considered test conditions (for a better comparison, the contours of the same quantities are plotted in the same scale for the two conditions). In particular, comparison between Figure 6.6a and Figure 6.6b verify that the test conditions do not differ significantly in terms of temperature distribution, as expectable due to the similar values of combustion chamber temperatures evaluated by means of the chemical equilibrium software. On the contrary, major differences are noticeable in the distribution of O₂ mass fraction, which is significantly higher in Test condition 2FJ.

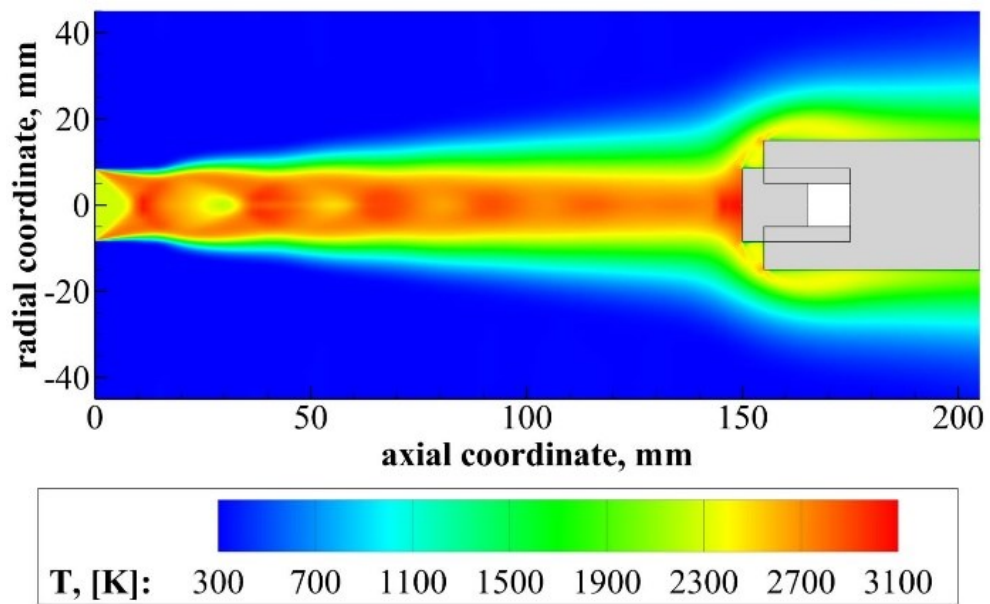
Finally, Table 6.4 summarizes the other significant quantities which characterize the test conditions at the sample location as estimated by the CFD simulations shown above.

Table 6.4. Conditions at sample location estimated with the CFD simulations of the free-jet test.

	Test condition 1FJ	Test condition 2FJ
Stagnation point pressure [bar]	2.6	3.2
Average CO ₂ mass fraction	0.27	0.29
Average H ₂ O mass fraction	0.11	0.12
Average O ₂ mass fraction	0.26	0.37
Average cold-wall surface heat flux [MW/m ²]	11.0	12.4

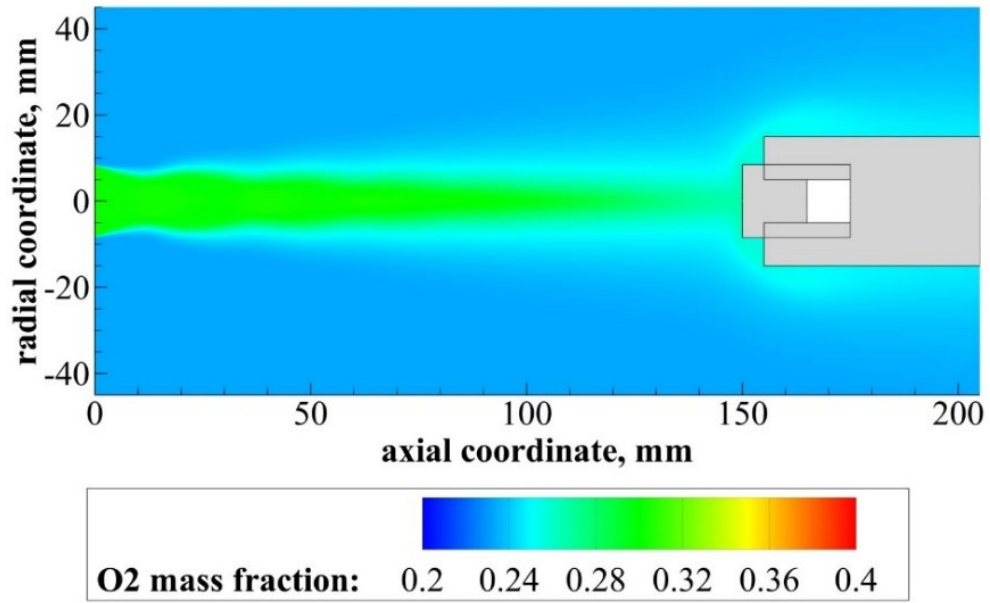


a) Test condition 1FJ

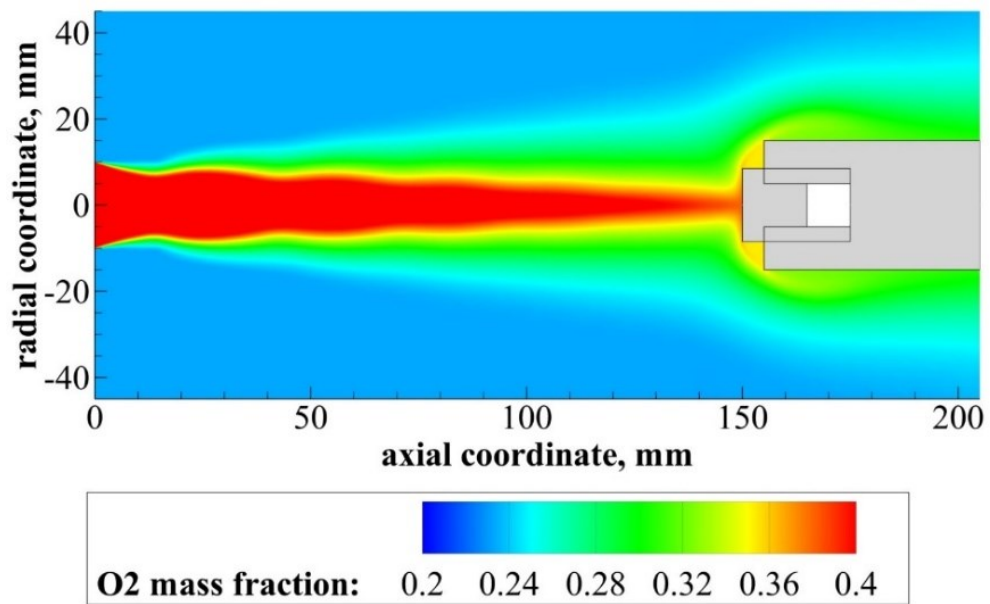


c) Test condition 2FJ

Figure 6.6. Temperature distribution in the free-jet test.



a) Test condition 1FJ



c) Test condition 2FJ

Figure 6.7. O₂ mass fraction distributions in the free jet tests.

6.3.3 Experimental results

6.3.3.1 Comparison between Ti_3SiC_2 -based and ZrB_2/SiC -based UHTCMC materials

The first tests aimed at comparing the response of UHTCMC materials with different matrix composition, testing the Ti_3SiC_2 -based samples and ZrB_2/SiC -based samples at the two different test conditions. In particular, samples TSC-SF-1 and ZBSC-LF-1 have been characterized at Test condition 1FJ and samples TSC-SF-2 and ZBSC-LF-2 have been tested at Test condition 2FJ.

The diagram in Figure 6.8 graphically represents the erosion rates estimated on the basis of the sample mass loss. In both test conditions, ZrB_2/SiC -based specimens showed a better erosion resistance and structural behaviour with respect to Ti_3SiC_2 -based ones. In particular, sample ZBSC-LF-1 showed an excellent resistance to the less demanding test conditions to which it was subjected, preserving structural integrity and demonstrating an almost null erosion rate ($5 \cdot 10^{-4}$ mm/s), while sample TSC-SF-1 already showed a significant erosion rate, equal to 0.204 mm/s. On the other side, correspondingly to the harsher aero-thermo-chemical loads, although also the sample ZBSC-LF-2 showed a perceptible erosion rate (equal to 0.184 mm/s), but it was anyhow significantly smaller than the case of sample TSC-SF-1, which was subjected to an erosion rate equal to 0.360 mm/s.

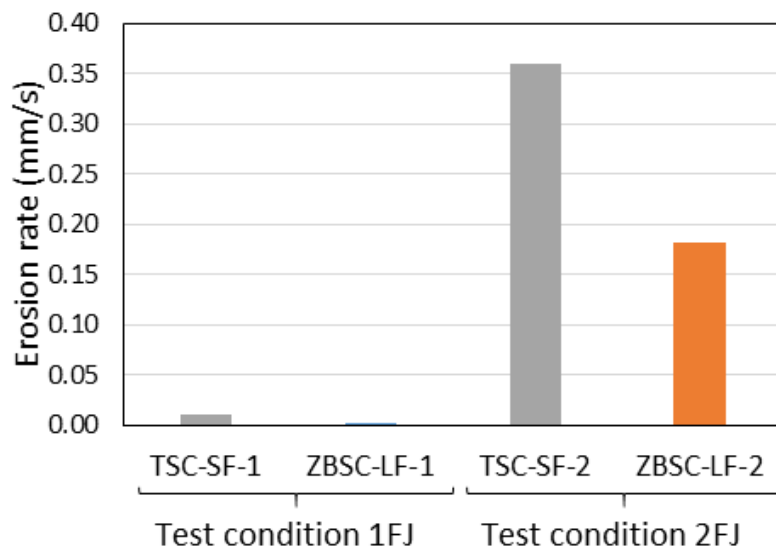


Figure 6.8. Erosion rates of UHTCMC samples in free jet test: comparison between Ti_3SiC_2 based samples and ZrB_2/SiC based samples.

Figure 6.9 and Figure 6.10 show pictures of the samples TSC-SF-1 and ZBSC-LF-1, respectively, before (top) and after (bottom) test at conditions 1FJ, taken by a CCD camera and the optical microscope described in Section 6.1. It is clear that the ZrB₂-SiC-based specimen preserved its original shape with no erosion. However, the microscopic observation of the surface revealed the presence of a thin, irregular white layer, after the test, presumably associated to oxidation of zirconium contained in the sample matrix. The Titanium Silicocarbide-based sample, on the contrary, eroded significantly, and the exposed surface appears to be almost completely oxidized.

Figure 6.11 and Figure 6.12 show the corresponding pictures of the samples TSC-SF-1 and ZBSC-LF-1, respectively, after test at conditions 2FJ. In this case, the former specimen head appears almost completely eroded (the asymmetry in the consumption is probably due to the non-correct alignment of the specimen with respect to the engine axis). On the other side, also for the ZrB₂-SiC-based specimen, almost all the exposed surface appears to be covered by zirconia. The more evident oxidation detected in these conditions, associated, as said, also to a considerably higher erosion rate, is explainable taking into account the higher content of oxidizing species in the flow, as exemplified by the molecular oxygen distribution presented in Figure 6.7.

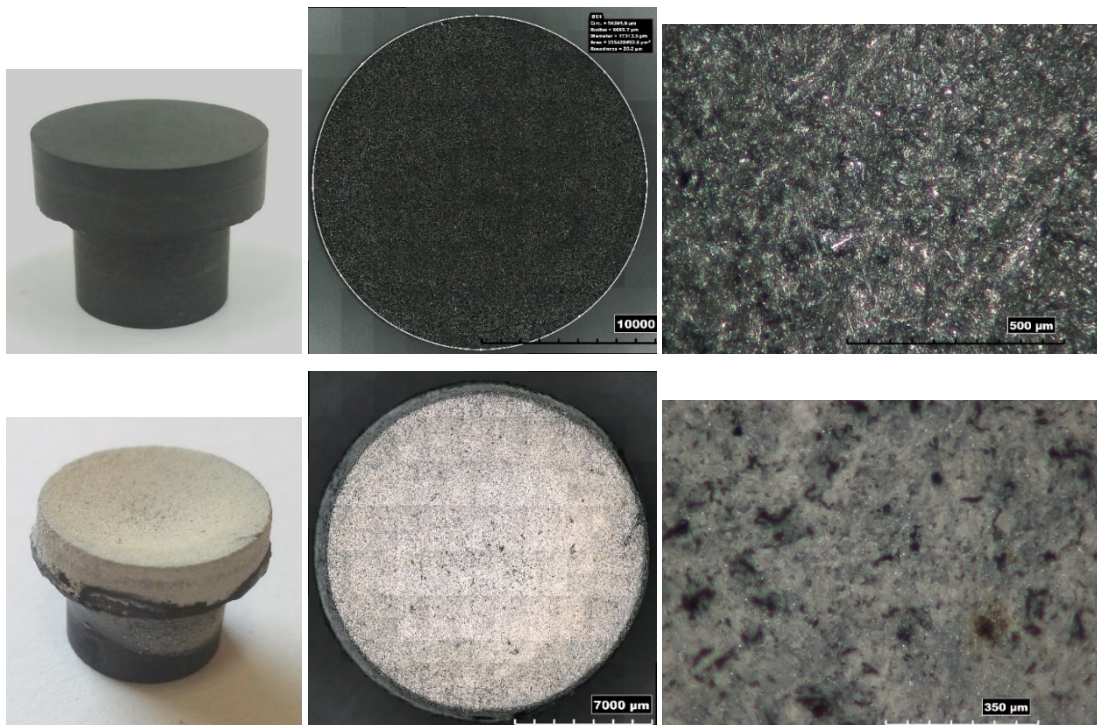


Figure 6.9. Pictures of sample TSC-SF-1 before (top) and after (bottom) the test.

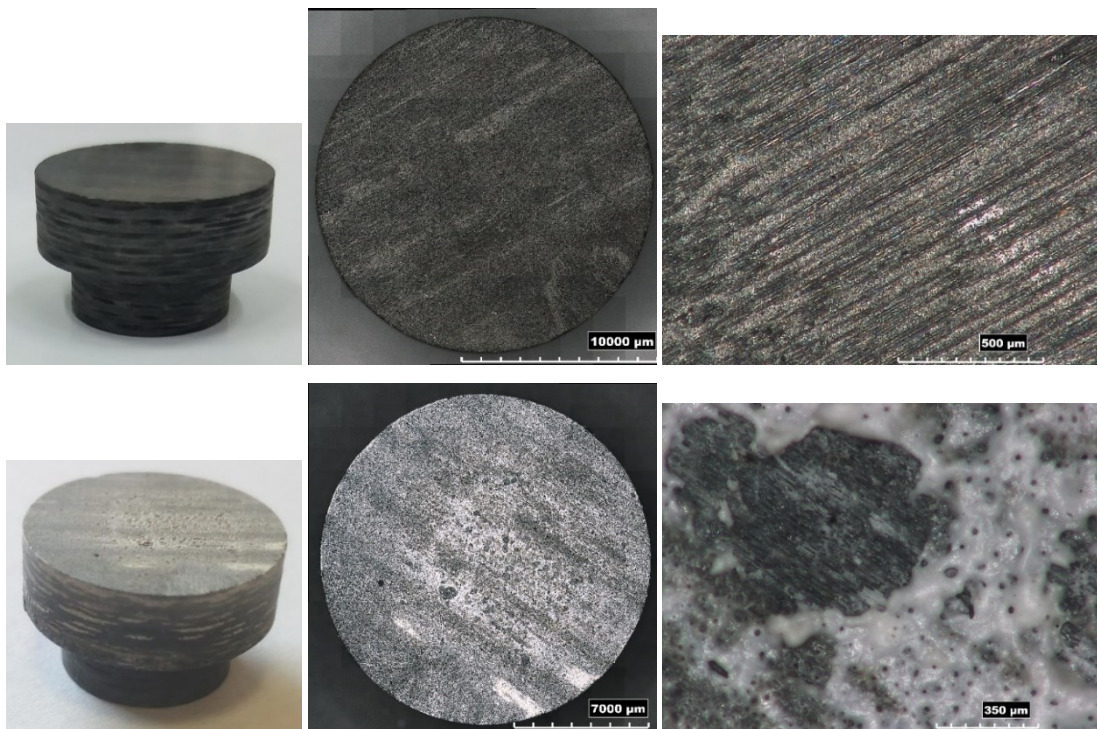


Figure 6.10. Pictures of sample ZBSC-LF-1 before (top) and after (bottom) the test.

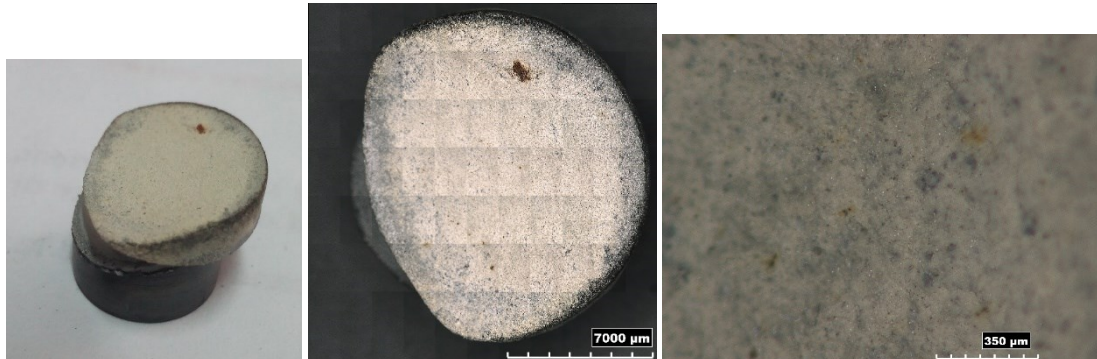


Figure 6.11. Pictures of sample TSC-SF-2 after the test.

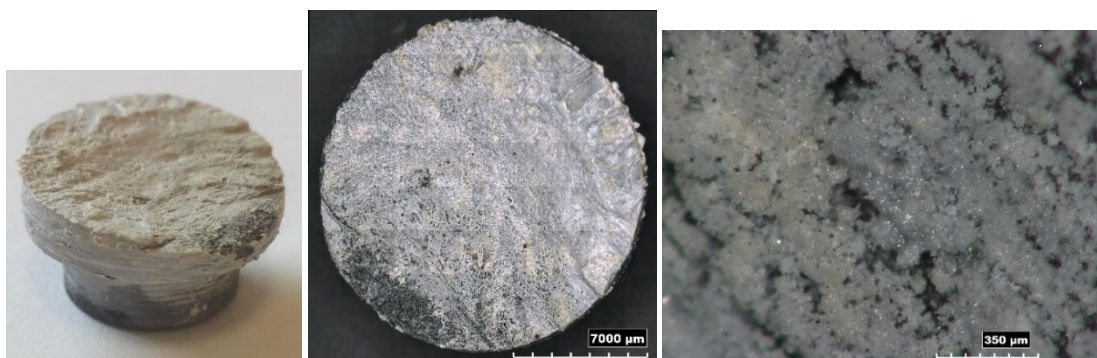


Figure 6.12. Pictures of sample ZBSC-LF-2 after the test.

Figure 6.13 shows the thermal histories of the samples tested in Test condition 1FJ, detected by the pyrometer ISQ5. The thermal histories of the two specimens practically overlap for the first 4-5 s, then, when T approaches 1900 K, the TSC-SF-1 sample experiences a sudden rise in temperature, which at the end of the test exceeds 2800 K.

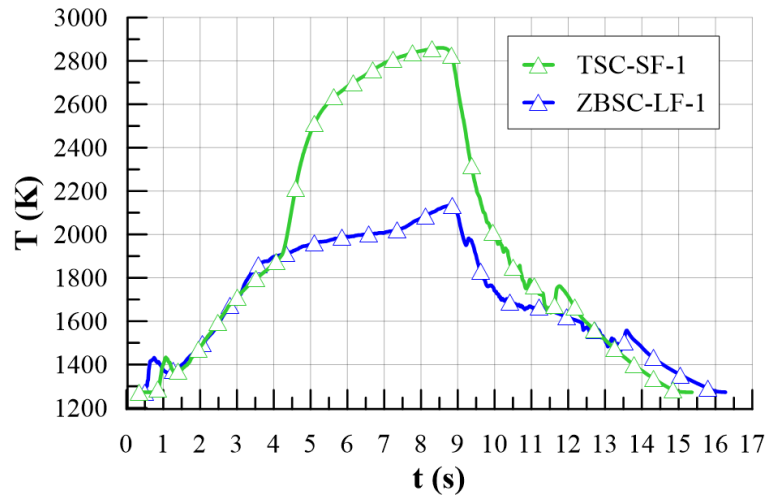


Figure 6.13. Thermal histories of the samples TSC-SF-1 and ZBSC-LF-1 tested in Test condition 1FJ.

The sudden temperature jump was associated to a change in the shape of the flame surrounding the sample, as clearly shown by comparison between Figure 6.14 and Figure 6.15, which depict images taken during test on TSC-SF and ZBSC-LF-1 respectively, at the beginning and at the end of the test. In particular, starting from the instant corresponding to the jump, a very bright halo developed in front of the TSC-SF sample, from which a considerable amount of material was removed, probably due to the extremely high shear stresses. As said before, this resulted in a consistent erosion, while, on the contrary, the stable behavior exhibited by sample ZBSC-LF-1 was associated to a near-zero erosion rate.

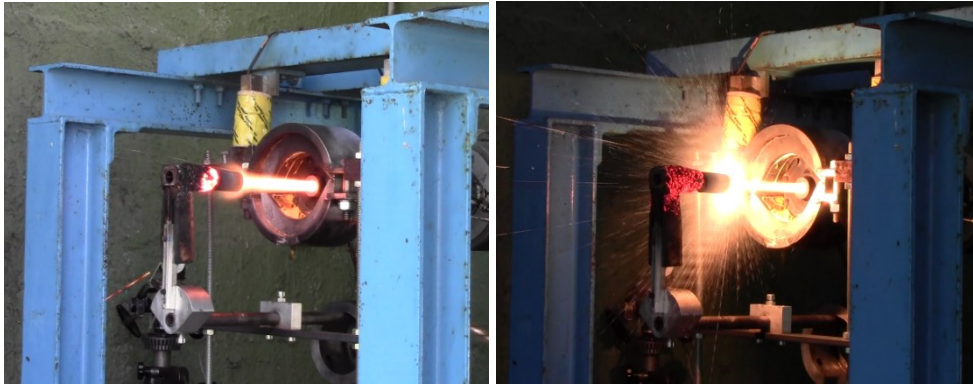


Figure 6.14. Pictures of test on TSC-SF-1 sample, at beginning (left) and end (right) of the test (Test Condition 1FJ).

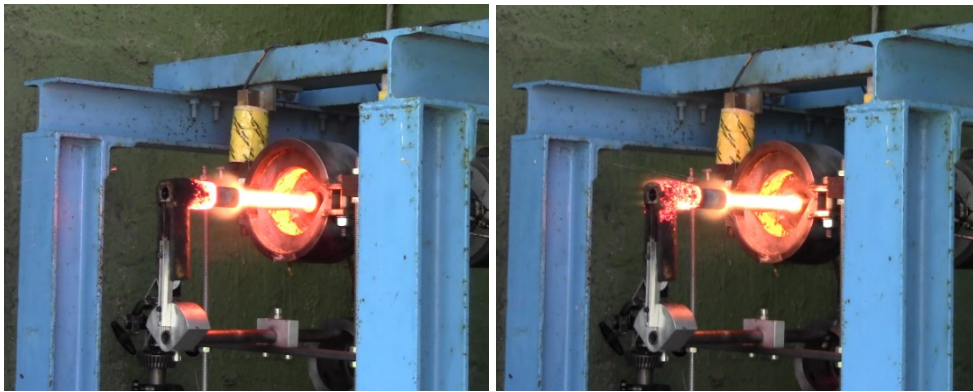


Figure 6.15. Pictures of test on ZBSC-LF-1 sample, at beginning (left) and end (right) of the test (Test Condition 1FJ).

Figure 6.16 shows four pictures taken by the infrared thermo-camera before and after the temperature jump occurred on sample TSC-SF-1. Immediately before the jump, the temperature on the front surface of the sample was relatively uniform. The temperature jump corresponds to a steep increase in temperature by almost 300 K in 0.5 s, localized in the central region of the surface. This also appears in Figure 6.17, showing the temperature radial profiles on the sample surface at different time instants. This is the area where the heat flux is most intense and the concentration of molecular oxygen is expected to be higher, so the jump might be associated to triggering, at high temperature, of chemical reactions involving the species contained in the ceramic matrix and/or the carbon fibers; the exothermic release of gaseous products might also justify the change in shape and brightness of the flame surrounding the sample, which was also detected by the thermo-camera, as noticeable in the last two pictures of Figure 6.16.

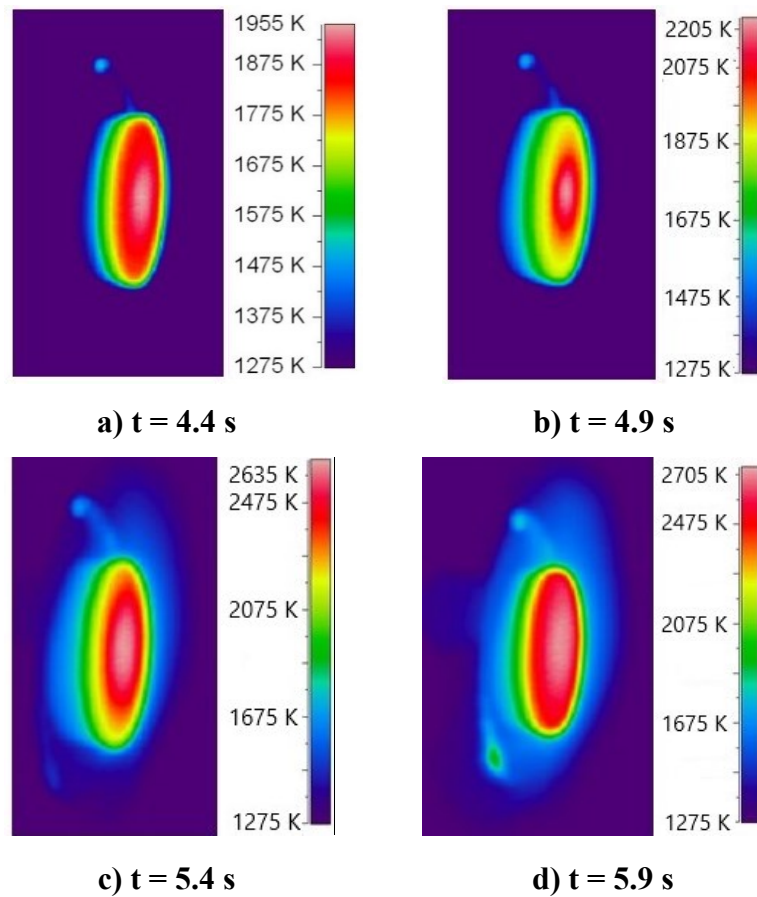


Figure 6.16. IR thermal images of TSC-SF-1 sample, taken every 0.5 s, starting from immediately before the temperature jump.

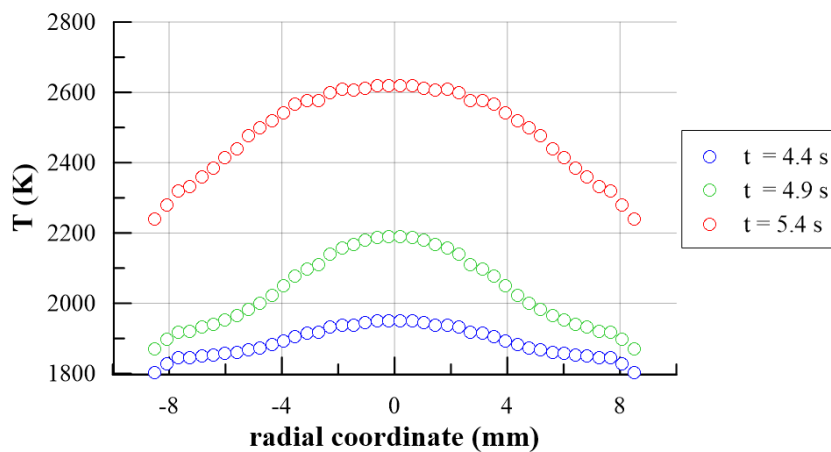


Figure 6.17. Temperature radial profiles, measured by the thermo-camera, on sample TSC-SF-1 front surface at different time instants, around the temperature jump.

Figure 6.18 shows the thermal histories of the samples tested in Test condition 2FJ. In this case, both specimens were subjected to the thermal jump and a consequently consistent erosion, as testified also from Figure 6.19, which shows two thermographic images taken during test on sample ZBSC-LF-2, highlighting the progressive thinning of the sample and the extremely high temperature distribution on the front surface.

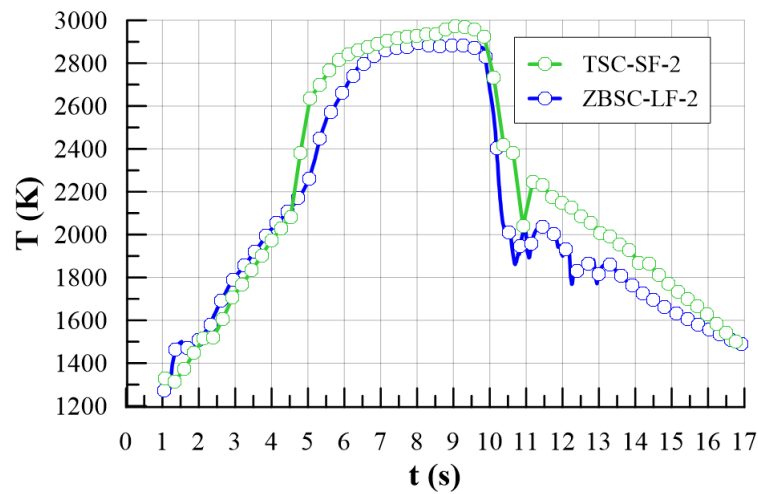


Figure 6.18. Thermal histories of the TSC-SF-2 and ZBSC-LF-2 samples tested in Test condition 2FJ.

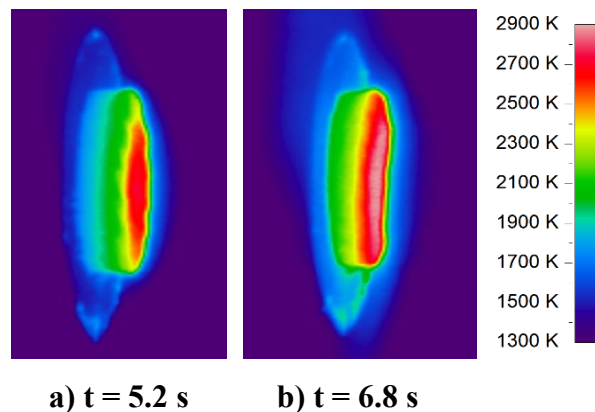


Figure 6.19. Thermographic images of sample ZBSC-LF-2.

6.3.3.2 Comparison between short-fibers-based and long-fibers-based UHTCMCs

In order to have a comparison between UHTCMC samples with the same matrix ($\text{ZrB}_2\text{-SiC}$ -based) and either short or long fibers, ZBSC-SF-1 sample has been tested at Test condition 2FJ and its behaviour has been confronted with the one of ZBSC-LF-2 sample tested at the same conditions.

Figure 6.20 graphically represents the measured erosion rates of the above-mentioned specimens, highlighting a very similar behaviour in the two cases. Also the histories of the maximum temperatures detected by the two-colour pyrometer on the front surface of the two specimens, shown in Figure 6.21, are very similar, with the presence in both cases of the temperature jump up to values over 2800 K.

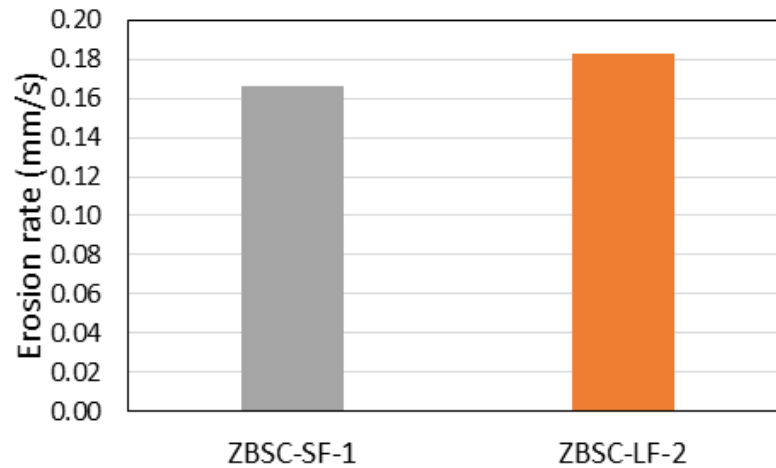


Figure 6.20. Erosion rates of UHTCMC samples in free jet test: comparison between short-fibers-based and long-fibers-based samples.

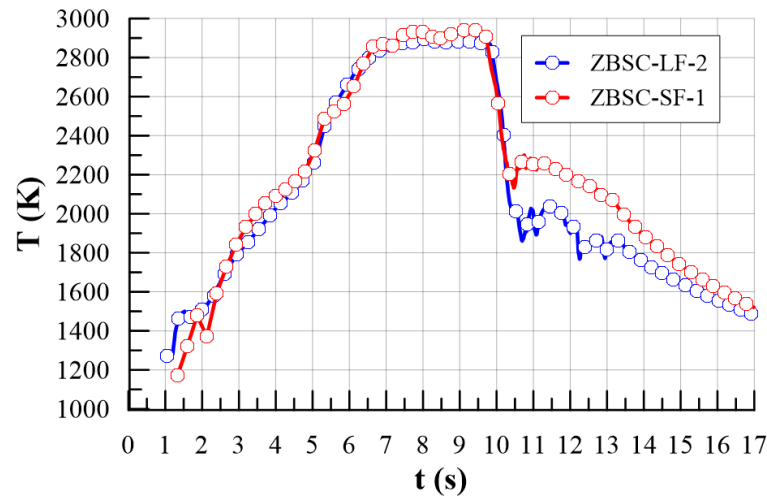


Figure 6.21. Thermal histories of the ZBSC-LF-2 and ZBSC-SF-1 samples tested in Test condition 2FJ.

6.4 Experimental characterization of UHTCMC nozzle throat insert

On the basis of the results shown above, ZrB_2/SiC -matrix based UHTCMC nozzle throat inserts have been manufactured and tested to characterize the materials in actual operating conditions and to compare their behaviour to that of a classical graphite nozzle. In this section, the tested prototypes, the test condition and the experimental results, in terms of the erosion behaviour and of the effect on the rocket performance, will be presented and discussed.

6.4.1 UHTCMC samples

Two UHTCMC nozzle throat inserts were manufactured and tested, which are summarized in Table 6.2. All of them were based on a UHTC matrix with Carbon fibers.

The two inserts had both a ZrB_2/SiC matrix, one with short (chopped) carbon fibers, uniformly dispersed into the matrix (i.e. with the same composition of ZBSC-

SF-1 sample), and the other with long continuous carbon fibers (i.e. with the same composition of ZBSC-LF-1/2 samples).

Table 6.5. UHTCMC nozzle throat inserts.

UHTCMC sample ID	Matrix composition	Carbon fibers
ZBSC-SF-TI	ZrB ₂ /SiC	Chopped
ZBSC-LF-TI	ZrB ₂ /SiC	Continuous Unidirectional

As mentioned before, besides the UHTCMC throat inserts, a nozzle completely made of a classical commercial graphite has been tested in the same conditions as reference.

6.4.2 Test conditions

For the experimental characterization of the nozzle inserts, two subsequent test have been performed, again with an oxygen mass flow rate equal first to 25 g/s and then to 40 g/s. Again, all tests had a nominal duration of 10 s. Cylindrical 220mm-long HDPE grains were employed as fuel and gaseous oxygen as oxidizer. In this case, for the estimation of the nominal test conditions the nominal value of the throat diameter, equal to 9.6 mm, has been considered in both cases, so in this case the most severe test condition foresees also a higher value of the chamber pressure. Table 6.6 summarizes the main nominal operating parameters of the test conditions, as estimated by means of the one-dimensional tool described in Section 6.2.1.

Table 6.6. Nominal test conditions throat insert testing.

	Test condition 1TI	Test condition 2TI
Oxidizer mass flow rate [g/s]	25	40
Oxidizer-to-Fuel ratio	5.13	6.50
Chamber pressure [bar]	6.49	9.63
Combustion temperature [K]	~ 3200	~ 3200
Nozzle inlet CO ₂ mass fraction	0.32	0.32
Nozzle inlet H ₂ O mass fraction	0.16	0.14
Nozzle inlet O ₂ mass fraction	0.30	0.41

Also in this case, CFD simulations of the flow field through the nozzle have been performed to collect additional significant information on the operating conditions around the prototypes.

Figure 6.22 and Figure 6.23 show the distributions of temperature and molecular oxygen mass fraction, respectively, in the flow field through the rocket nozzle, for the two considered test conditions (for a better comparison, the contours of the same quantities are plotted in the same scale for the two conditions). Again it can be observed that the temperature distributions are similar, while Test condition 2TI is characterized by a more oxidizing chemical environment.

Finally, Table 6.7 summarizes the other significant quantities which characterize the test conditions at on the throat insert as estimated by the CFD simulations shown above.

Table 6.7. Conditions at nozzle throat estimated with the CFD simulations.

	Test condition 1TI	Test condition 2TI
Pressure [bar]	3.2	4.8
Shear stress [hPa]	30.5	42.3
Average CO ₂ mass fraction	0.51	0.42
Average H ₂ O mass fraction	0.22	0.18
Average O ₂ mass fraction	0.27	0.40
Average cold-wall surface heat flux [MW/m ²]	17.0	20.0

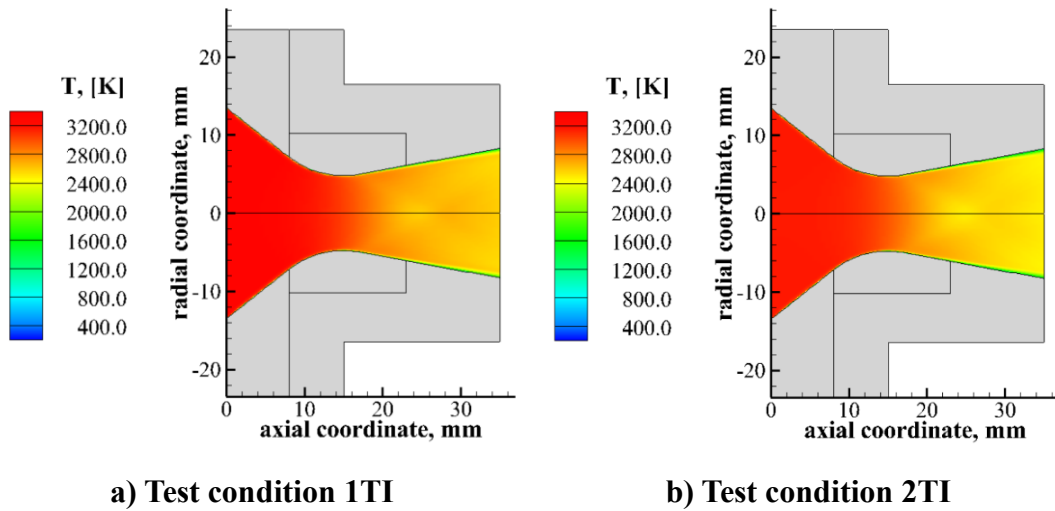


Figure 6.22. Temperature distribution through rocket nozzle.

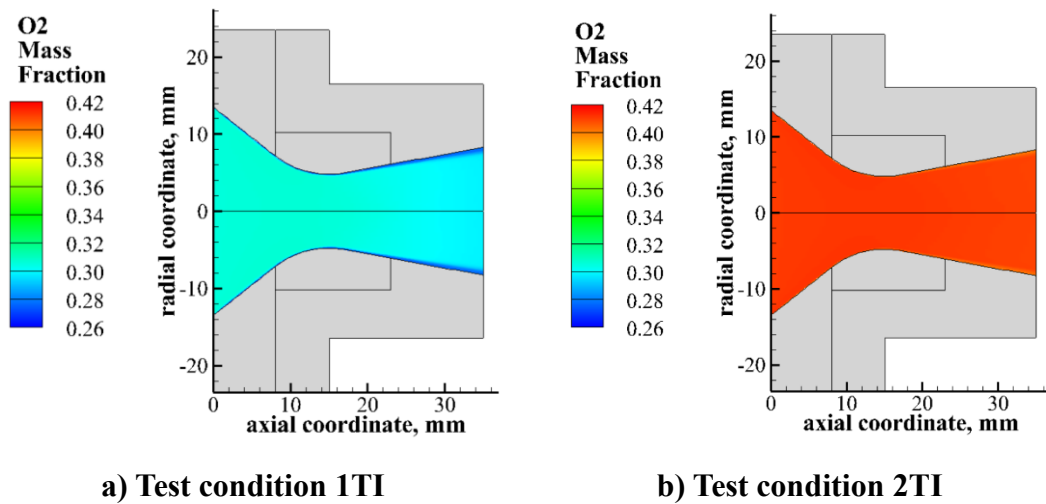


Figure 6.23. O₂ mass fraction distributions through rocket nozzle.

6.4.3 Experimental results

As anticipated before, each throat insert has been tested subsequently in Test condition 1TI and 2TI, to experimentally characterize its erosion resistance for rocket nozzle application, and the material behaviour has been compared to that of a reference graphite nozzle tested in the same test conditions.

After the first test in condition 1TI, it was detected that the throat diameter of the graphite nozzle increased from the nominal value of 9.6 mm to 9.9 mm, while no significant erosion occurred with the two UHTCMC throat inserts. After firing test in conditions 2TI, further considerable erosion occurred in the case of graphite nozzle, whose throat diameter increased up to around 11.4 mm. In the most severe conditions, also the ZBSC-LF-TI has been subjected to a perceptible erosion, which however was smaller than the former case, with an increase of the throat diameter up to 10.4 mm. On the other side, ZBSC-SF-TI showed a good resistance, with negligible erosion rate also at Test condition 2TI. The diagram in Figure 6.24 graphically represents the corresponding average erosion rates, from which the improved resistance of the UHTCMC materials appears clear.

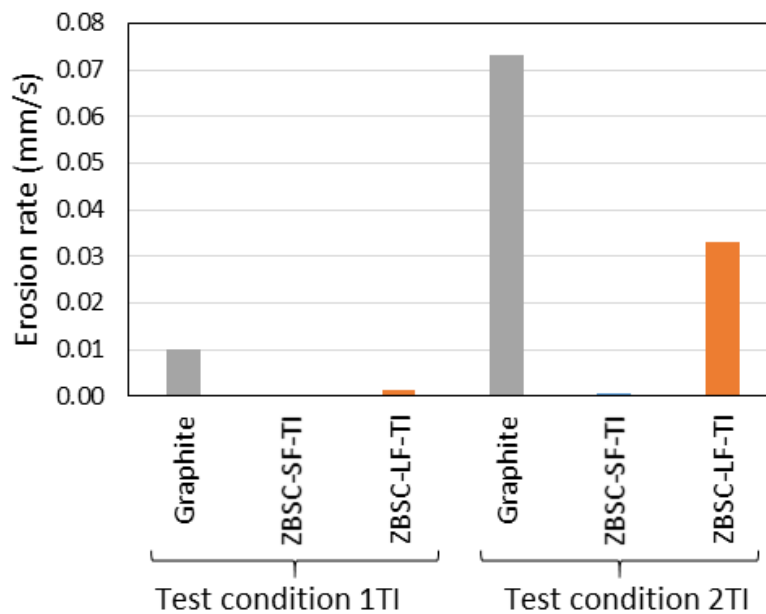


Figure 6.24. Nozzle throat erosion rates.

Figure 6.25, Figure 6.26 and Figure 6.27 show the microscopic pictures of the zone around the throat section before tests and after both firing tests for the graphite nozzle, the ZBSC-SF-TI and ZBSC-LF-TI, respectively, from which the different growth of the throat section area can be observed. Furthermore, in the latter case also an increase of the surface roughness can be noticed, probably due to the erosion of the carbon fibers which are less resistant than the ceramic matrix.

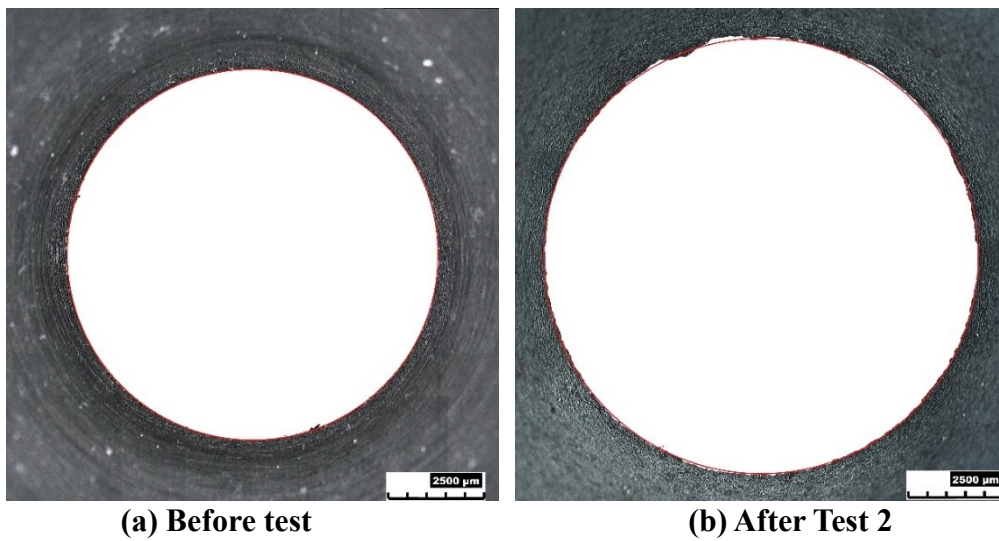


Figure 6.25. Microscopic pictures of graphite nozzle throat.

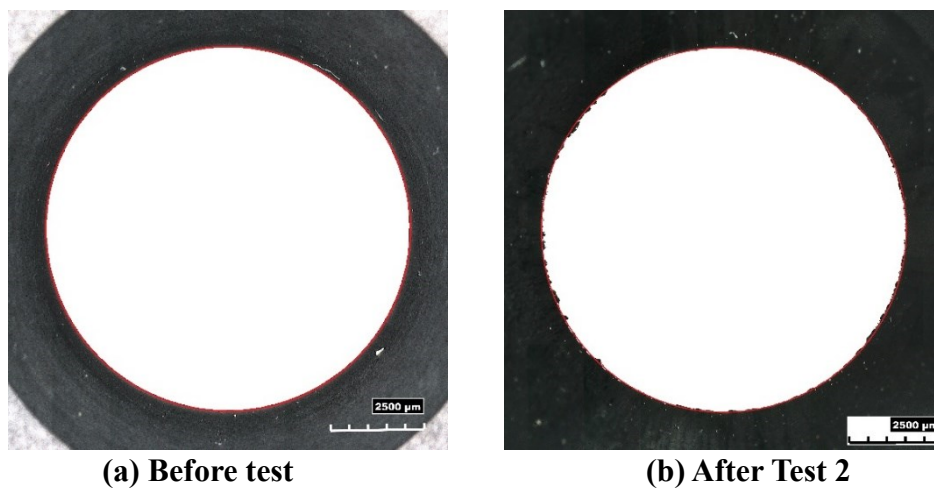


Figure 6.26. Microscopic pictures of ZBSC-SF-TI.

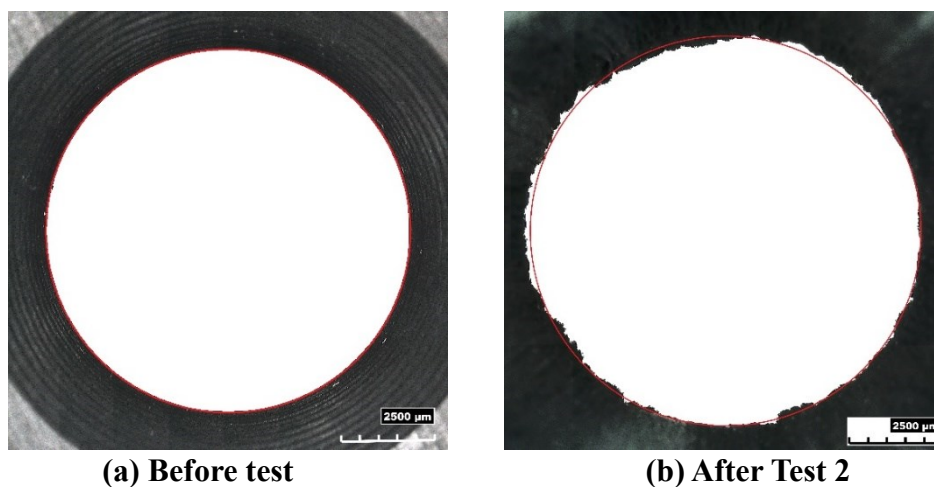


Figure 6.27. Microscopic pictures of ZBSC-LF-TI.

The different erosion behaviour highlighted above affects directly the rocket performance. shows the profiles of the measured chamber pressure during the operating time and the comparison with the corresponding theoretical pressure profile estimated with the tool described in Section 6.2.1, for the three firings performed in Test conditions 2TI, in which the difference in the behaviours is more evident. In fact, in the test performed with the graphite nozzle the pressure trace shows a significantly decreasing trend due to the strong throat erosion. On the other side, in the test performed with the ZBSC-SF-TI, the chamber pressure is stable during the all engine operation, while, in the test performed with the ZBSC-LF-TI, the pressure trace is only slightly decreasing with respect the numerically calculated one.

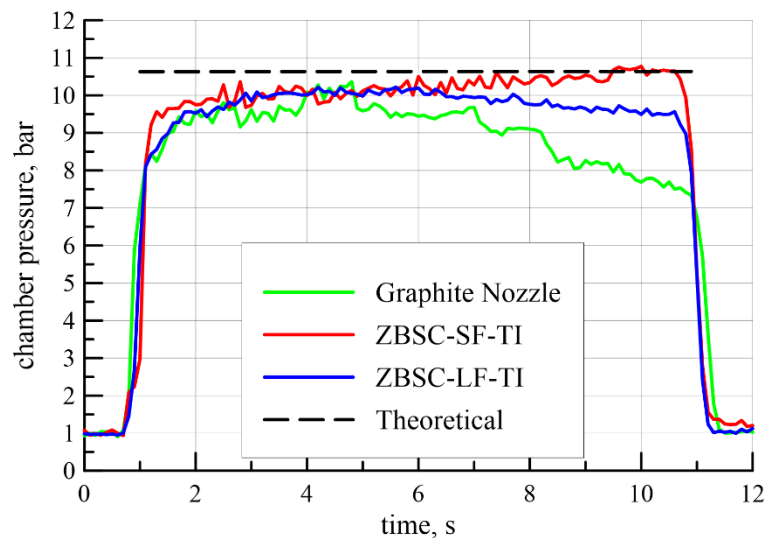


Figure 6.28. Theoretical and measured chamber pressures vs operating time for tests in conditions 2TI.

CONCLUSIONS

The present dissertation dealt with two of the major issue in hybrid rocket propulsion technology development: first the definition of proper numerical models for the engine internal ballistics simulation, with the capability to predict the fuel consumption behaviour and the corresponding rocket performance, and second the characterization of high-performance UHTCMCs for near-zero erosion rocket nozzle application.

For the first task, a CFD approach to the simulation of internal ballistics of hybrid rocket engines have been presented. The RANS equations, with two additional transport equations for the average mixture fraction and its variance combined to the probability density function combustion model and thermochemical equilibrium were solved. Two different integrated sub-model suitable to describe the interaction between the gaseous flow and the grain surface for the prediction of the fuel regression rate was defined and implemented for either the case of conventional polymeric fuels and the case of liquefying paraffin-based fuels. The gas/surface interaction modelling is based on the local mass, energy and mixture fraction balances, but a different treatment has been identified to model the different consumption mechanism of the two abovementioned class of fuels, including either an additional equation for the fuel surface pyrolysis modelling in the case of polymeric fuels, or an equation for the estimation of the additional component of the regression rate due to the droplets entrainment phenomenon for the case of paraffin fuels. A number of experimental test cases, consisting in the combustion of gaseous oxygen with different fuel grains in laboratory scale hybrid rockets, were numerically reproduced in order to asses the validation of the numerical models. A good agreement between the calculated regression rate and the measured data is obtained in the different considered cases. However, the comparison between numerical results and experimental data highlighted the need of some improvements of the presented numerical method for the application to liquefying fuels aimed at overcoming the simplified modelling of the

entrainment fuel mass addition in the computational domain, which could be the subject of future studies.

For what concern the second issue, an experimental campaign was carried out to characterize new-class of UHTCMCs in relevant environment for nozzle rocket application. In particular, small sized samples were exposed to the supersonic flow of the exhaust gases coming from the nozzle of a 200N-class hybrid rocket at two different test conditions. These tests allowed to identify the first potential candidate compositions for the final application, based on ZrB_2 -SiC matrix and either chopped or long continuous carbon fibers. Consequently, two nozzle inserts made of UHTCMC with the same compositions, were manufactured and tested. The material behaviors and the corresponding rocket performance were then analyzed and compared with those of a classical graphite nozzle, showing that the UHTCMC provides a better and more stable engine operation thanks to its improved erosion resistance.

ACKNOWLEDGMENTS

A significant part of the PhD research activities have been supported by the European Commission, through the C³HARME research project, which has received funding in the framework of Horizon2020 research and innovation programme under the Grant Agreement n° 685594.

The experimental activities and the firing tests carried out at the Aerospace Propulsion Laboratory located in the military airport “F. Baracca” of Grazzanise (CE) have been possible thanks to the cooperation agreement between the University of Naples “Federico II” and the Italian Air Force.

The microscopic pictures presented in this work have been realized thanks to the courtesy of CIRTIBS Research Centre.

Then, at the end of this important experience, I would like to acknowledge all the people who contributed to my scientific and personal growth.

Firstly, I would like to express my sincere gratitude to my supervisor Prof. Raffaele Savino for the continuous support in my PhD activities, for his immense knowledge, the motivation in hardworking and the countless teachings.

I would like to thank my advisor Dr Carmine Carmicino who helped me during my PhD with his enviable passion and willingness to continuous improvement.

A special thank goes to Stefano, a very good friend who I was lucky to work with during these three years sharing a lot of fun as well as the occasional concerns and troubles. I wish also to thank Anselmo and Giandomenico, Dr Antonio Esposito and all the professors, research fellows and engineers who helped me during my research activities with their precious experience. Many thanks to Mr Antonio Alfano, for his availability and infinite patience in all the manufacturing works I needed for my activities, and to all the technical and administrative staff for their valuable support.

Last but not the least, I would like to thank my parents, my sister and all my family for their priceless, never-ending support, and all my friends for all the fun, the cheerful moments, the precious advices and encouragements they always gave to me.

BIBLIOGRAPHY

- [1] D. Altman and R. Humble, "Hybrid Rocket Propulsion Systems," in *Space Propulsion Analysis and Design*, 1st ed., R. Humble, G. Henry and W. Larson, Eds., New York, McGraw-Hill, 1995, pp. 365-370.
- [2] D. Altman and A. Holzman, "Overview and History of Hybrid Rocket Propulsion," in *Fundamentals of Hybrid Rocket Combustion and Propulsion*, vol. 218, K. Kuo and M. Chiaverini, Eds., Progress in Astronautics and Aeronautics, AIAA, 2007, pp. 1-36.
- [3] C. Oikine, "New Perspectives for Hybrid Propulsion," in *42nd AIAA/ASME/SAE/ASEE Joint Propulsion Conference & Exhibit*, Sacramento, California, 2006.
- [4] J. Ronningen and J. Husdal, "Nammo Hybrid Rocket Propulsion TRL Improvement Program," in *48th AIAA/ASME/SAE/ASEE Joint Propulsion Conference & Exhibit*, Atlanta, Georgia, 2012.
- [5] L. Casalino and D. Pastrone, "Optimal Design of Hybrid Rocket Motors for a Microgravity Platform," *Journal of Propulsion and Power*, vol. 24, no. 3, pp. 491-498, 2008.
- [6] A. Chandler, B. Cantwell, G. Hubbard and A. Karabeyoglu, "A Two-Stage, Single Port Hybrid Propulsion System for a Mars Ascent Vehicle," in *46th AIAA/ASME/SAE/ASEE Joint Propulsion Conference & Exhibit*, Nashville, TN, 2010.
- [7] L. Casalino, F. Letizia and D. Pastrone, "Optimization of Hybrid Upper Stage Motor with Coupled Evolutionary/Indirect Procedure," *Journal of Propulsion and Power*, vol. 30, no. 5, pp. 1390-1398, 2014.
- [8] G. Crouch, "The market for space tourism: early indications," *Journal of Travel Research*, vol. 40, no. 2, pp. 213-219, 2001.

- [9] D. Webber, "Space tourism: its history, future and importance," *Acta Astronautica*, vol. 92, pp. 138-143, 2013.
- [10] The Tauri Group, "Suborbital reusable vehicles: a 10-year forecast of market demand," Federal Aviation Administration (FAA) - Office of Commercial Space Transportation and Space, Washington, DC, 2012.
- [11] A. Snow, E. Buchen and J. Olds, "Global launch vehicle market assessment - A study of launch services for nano/microsatellites in 2013," SpaceWorks, Atlanta, GA, 1999.
- [12] S. Burke and E. Schumann, "Diffusion flames," *Industrial and Engineering Chemistry*, vol. 20, no. 10, pp. 998-1004, 1928.
- [13] L. J. Green, "Introductory considerations on hybrid rocket combustion," *Progress in Astronautics and Rocketry*, vol. 15, pp. 451-484, 1964.
- [14] T. Houser and M. Peck, "Research in hybrid combustion," *Progress in Astronautics and Rocketry*, vol. 15, pp. 559-581, 1964.
- [15] G. Marxman and M. Gilbert, "Turbulent boundary layer combustion in the hybrid rocket," *Symposium (International) on Combustion*, vol. 9, no. 1, pp. 371-383, 1963.
- [16] G. Marxmann, "Combustion in the turbulent boundary layer on a vaporizing surface," *Symposium (International) on Combustion*, vol. 10, no. 1, pp. 1337-1349, 1965.
- [17] C. Carmicino and A. Russo Sorge, "Role of injection in hybrid rockets regression rate behavior," *Journal of Propulsion and Power*, vol. 21, no. 4, pp. 606-612, 2005.
- [18] C. Carmicino and A. Russo Sorge, "Influence of a conical axial injector on hybrid rocket performance," *Journal of Propulsion and Power*, vol. 22, no. 5, pp. 984-995, 2006.
- [19] M. Motoe and T. Shimada, "Numerical simulation of combustive flows in a swirling-oxidizer-flow-type hybrid rocket," in *52nd Aerospace Sciences Meeting*, National Harbor, Maryland, 2014.

- [20] C. Kumar and A. Kumar, "A numerical study on the regression rate of hybrid rocket motors using a combination of enhancement techniques," in *48th AIAA/ASME/SAE/ASEE Joint Propulsion Conference & Exhibit*, Atlanta, Georgia, 2012.
- [21] C. Carmicino and A. Russo Sorge, "Experimental investigation into the effect of solid-fuel additives on hybrid rocket performance," *Journal of Propulsion and Power*, vol. 31, no. 2, pp. 699-713, 2015.
- [22] M. Karabeyoglu, B. Cantwell and D. Altman, "Development and testing of paraffin-based hybrid rocket fuels," in *37th Joint Propulsion Conference and Exhibit*, Salt Lake City, Utah, 2001.
- [23] M. Karabeyoglu, D. Altman and B. Cantwell, "Combustion of liquefying hybrid propellants: Part 1, general theory," *Journal of Propulsion and Power*, vol. 18, no. 3, pp. 610-620, 2002.
- [24] A. Mazzetti, L. Merotto and G. Pinarello, "Paraffin-based hybrid rocket engines applications: a review and a market perspective," *Acta Astronautica*, vol. 126, pp. 286-297, September-October 2016.
- [25] M. A. Karabeyoglu and B. J. Cantwell, "Combustion of liquefying hybrid propellants: part 2, stability of liquid films," *Journal of Propulsion and Power*, vol. 18, no. 3, pp. 621-630, 2002.
- [26] A. Petrarolo, M. Kobald and S. Schleichriem, "Understanding Kelvin-Helmholtz instability in paraffin-based hybrid rocket fuels," *Experiments in Fluids*, pp. 59-62, 2018.
- [27] A. A. Chandler, E. T. Jens, B. J. Cantwell and G. S. Hubbard, "Visualization of the liquid layer combustion of paraffin fuel for hybrid rocket applications," in *48th AIAA/ASME/SAE/ASEE Joint Propulsion Conference & Exhibit*, Atlanta, Georgia, 2012.
- [28] B. Cantwell, A. Karabeyoglu and D. Altman, "Recent advances in hybrid propulsion," *International Journal of Energetic Materials and Chemical Propulsion*, vol. 9, no. 4, pp. 305-326, 2010.

- [29] M. Kobald, C. Schmierer, H. Ciezki, S. Schlechtriem, E. Toson and L. De Luca, "Viscosity and regression rate of liquefying hybrid rocket fuels," *Journal of Propulsion and Power*, vol. 33, no. 5, pp. 1245-1251, 2017.
- [30] Y. Chen, T. Chou, B. Gu, J. Wu, B. Wu, Y. Lian and L. Yang, "Multiphysics simulations of rocket engine combustion," *Computers & Fluids*, vol. 45, no. 1, pp. 29-36, 2011.
- [31] A. Coronetti and W. Sirignano, "Numerical analysis of hybrid rocket combustion," *Journal of Propulsion and Power*, vol. 29, no. 2, pp. 371-384, 2013.
- [32] M. Lazzarin, F. Barato, A. Bettella and D. Pavarin, "Computational fluid dynamics simulation of regression rate in hybrid rockets," *Journal of Propulsion and Power*, vol. 29, no. 6, pp. 1445-1452, 2013.
- [33] D. Bianchi and F. Nasuti, "Numerical analysis of nozzle material thermochemical erosion in hybrid rocket engines," *Journal of Propulsion and Power*, vol. 29, no. 3, pp. 547-558, 2013.
- [34] G. Leccese, D. Bianchi and F. Nasuti, "Simulation of hybrid rocket flowfields including modeling of fuel pyrolysis and thermal radiation," in *5th Space Propulsion Conference*, Rome, Italy, 2016.
- [35] V. Sankaran, "Computational fluid dynamic modeling of hybrid rocket flowfields," in *Fundamentals of hybrid rocket combustion and propulsion*, vol. 218, K. Kuo and M. Chiaverini, Eds., Progress in Astronautics and Aeronautics, AIAA, 2007, pp. 323-349.
- [36] D. Bianchi, F. Nasuti and C. Carmicino, "Hybrid rockets with axial injector: port diameter effect on fuel regression rate," *Journal of Propulsion and Power*, vol. 32, no. 4, pp. 984-996, 2016.
- [37] D. Bianchi, B. Betti, F. Nasuti and C. Carmicino, "Simulation of gaseous oxygen/hydroxyl-terminated polybutadiene hybrid rocket flowfields and comparison with experiments," *Journal of Propulsion and Power*, vol. 31, no. 3, pp. 919-929, 2015.

- [38] M. Lazzarin, M. Faenza, F. Barato, N. Bellomo, A. Bettella and D. Pavarin, "Computational fluid dynamics simulation of hybrid rockets of different scales," *Journal of Propulsion and Power*, vol. 31, no. 5, pp. 1458-1469, 2015.
- [39] G. Ranuzzi, D. Cardillo and M. Invigorito, "Numerical investigation of a N₂O-Paraffin hybrid rocket engine combusting flowfield," in *6th European Conference for Aeronautics and Space Sciences (EUCASS)*, Krakow, Poland, 2015.
- [40] J. Y. Lestrade, J. Anthoine and G. Lavergne, "Liquefying fuel regression rate modeling in hybrid propulsion," *Aerospace Science and Technology*, vol. 42, pp. 80-87, 2015.
- [41] G. Leccese, D. Bianchi, F. Nasuti, K. Stober, N. Pavan and B. Cantwell, "Simulations of paraffin-based hybrid rocket engines and comparison with experiments," in *53rd AIAA/SAE/ASEE Joint Propulsion Conference*, Atlanta, Georgia, 2017.
- [42] G. Di Martino, P. Malgieri, C. Carmicino and R. Savino, "A simplified computational fluid-dynamic approach to the oxidizer injector design in hybrid rockets," *Acta Astronautica*, vol. 129, pp. 8-21, December 2016.
- [43] G. Di Martino, S. Mungiguerra, C. Carmicino and R. Savino, "Computational fluid-dynamic simulations of hybrid rocket internal flow including discharge nozzle," in *53rd AIAA/SAE/ASEE Joint Propulsion Conference*, Atlanta, Georgia, 2017.
- [44] AVIO, UNINA, DLR, ISTEC, "C3HARME D1.1 - User requirements and technical goals for Near Zero-erosion nozzles," 2016.
- [45] R. Savino, G. Festa, A. Cecere, L. Pienti and D. Sciti, "Experimental set up for characterization of carbide-based materials in propulsion environment," *Journal of the European Ceramic Society*, vol. 35, no. 6, pp. 1715-1723, 2015.

- [46] R. Hickman, T. Mc Kechnie and A. Agarwal, "Net shape fabrication of high temperature materials for rocket engine components," in *37th Joint Propulsion Conference and Exhibit*, Salt Lake City, Utah, 2001.
- [47] J. Johnston, R. Signorelli and J. Freche, "Performances of rocket nozzle material with several solid propellants," NASA Technical note 3428.3, 1966.
- [48] P. Thakre and V. Yang, "Chemical erosion of carbon-carbon/graphite nozzles in solid-propellant rocket motors," *Journal of Propulsion and Power*, vol. 24, no. 4, pp. 822-833, 2008.
- [49] J. Murugan, T. Kurian, J. Jayaprakash and J. T., "Design and Thermo-Structural Analysis of the Interface between Subscale Versions of Carbon-Carbon (C-C) Nozzle Divergent to Metallic flange hardware for a Ground Simulation Test," in *68th International Astronautical Congress*, Adelaide, Australia, 2017.
- [50] L. Kamps, S. Hirai, Y. Ahmimache, R. Guan and H. Nagata, "Investigation of Graphite Nozzle-Throat-Erosion in a Laboratory-Scale Hybrid Rocket Using GOX and HDPE," in *53rd AIAA/SAE/ASEE Joint Propulsion Conference*, Atlanta, Georgia, 2017.
- [51] M. Natali, J. Kenny and L. Torre, "Science and technology of polymeric ablative materials for thermal protection systems and propulsion devices: A review," *Progress in Materials Science*, vol. 84, pp. 192-275, 2016.
- [52] G. Harrington and G. Hilmas, "Thermal conductivity of ZrB₂ and HfB₂," in *Ultra-High Temperature Ceramics: Materials for Extreme Environment Applications*, 1st ed., W. Fahrenholtz, E. Wuchina, W. Lee and Y. Zhou, Eds., John Wiley & Sons, Inc., 2014, pp. 197-235.
- [53] J. Koo, H. Stretz, J. Weispfenning, Z. Luo and W. Wootan, "Nanocomposite rocket ablative materials: processing, microstructure, and performance," in *45th AIAA/ASME/ASCE/AHS/ASC Structures, Structural Dynamics & Materials Conference*, Palm Springs, California, 2004.
- [54] D. Sciti, L. Zoli, L. Silvestroni, A. Cecere, G. Di Martino and R. Savino, "Design, fabrication and high velocity oxy-fuel torch tests of a Cf-ZrB₂-

- fiber nozzle to evaluate its potential in rocket motors,” *Materials & Design*, vol. 109, pp. 709-717, 2016.
- [55] Y. Wang, Z. Chen and S. Yu, “Ablation behaviour and mechanism of C/SiC Composites,” *Journal of Materials Research and Technology*, vol. 5, no. 2, pp. 170-182, 2016.
- [56] L. Zoli and D. Sciti, “Efficacy of a ZrB₂-SiC matrix in protecting C fibres from oxidation in novel UHTCMC materials,” *Materials & Design*, vol. 113, pp. 207-213, 2017.
- [57] L. Zoli, V. Medri, C. Melandri and D. Sciti, “Continuous SiC fibers-ZrB₂ composites,” *Journal of the European Ceramic Society*, vol. 35, no. 16, pp. 4371-4376, 2015.
- [58] L. Zoli, A. Vinci, P. Galizia, C. Melandri and D. Sciti, “On the thermal shock resistance and mechanical properties of novel unidirectional UHTCMCs for extreme environments,” *Scientific Reports*, vol. 8, 2018.
- [59] UNINA, AVIO, DLR, ISTEC, “C3HARME D1.4 - Design of prototypes & Test conditions for applications 1, 2”.
- [60] C. Carmicino, F. Scaramuzzino and A. Russo Sorge, “Trade-off between paraffin-based and aluminium-loaded HTPB fuels to improve performance of hybrid rocket fed with N₂O,” *Aerospace Science and Technology*, vol. 37, pp. 81-92, August 2014.
- [61] C. Carmicino, “Acoustics, vortex shedding, and low-frequency dynamics interaction in an unstable hybrid rocket,” *Journal of Propulsion and Power*, vol. 25, no. 6, pp. 1322-1335, 2009.
- [62] A. Russo Sorge, C. Carmicino and A. Nocito, “Design of a lab-scale cooled two-dimensional plug nozzle for experimental tests,” in *38th AIAA/ASME/SAE/ASEE Joint Propulsion Conference & Exhibit*, Indianapolis, Indiana, 2002.
- [63] S. Bonifacio, G. Festa and A. Russo Sorge, “Novel structured catalysts for hydrogen peroxide decomposition in monopropellant and hybrid

- rockets,” *Journal of Propulsion and Power*, vol. 29, no. 5, pp. 1130-1137, 2013.
- [64] L. Galfetti, F. Nasuti, D. Pastrone and A. Russo, “An Italian network to improve hybrid rocket performance: strategy and results,” *Acta Astronautica*, vol. 96, pp. 246-260, March-April 2014.
- [65] S. Gordon and B. McBride, “Computer program of complex chemical equilibrium compositions and applications,” Nasa Reference Publication 1311, 1994.
- [66] G. Di Martino, S. Mungiguerra, C. Carmicino, R. Savino, D. Cardillo, F. Battista, M. Invigorito and G. Elia, “200-N laboratory scale hybrid rocket testing for paraffin fuel performance characterization,” *Journal of Propulsion and Power*, 2018.
- [67] A. Chorin, “Numerical solution of the Navier-Stokes equations,” *Mathematics of Computation*, vol. 22, no. 104, pp. 745-762, 1968.
- [68] T. Cebeci, *Analysis of Turbulent Flows*, Kidlington, Oxfordshire: Elsevier Ltd, 2004.
- [69] F. Menter, “Two-equation Eddy-viscosity turbulence models for engineering applications,” *AIAA Journal*, vol. 32, no. 8, pp. 1598-1605, 1994.
- [70] D. Wilcox, “Turbulence Energy Equation Models,” in *Turbulence Modeling for CFD*, La Canada, California, DCW Industries, 1998, pp. 73-170.
- [71] C. Wooldridge, G. Marxman and R. Kier, “Investigation of combustion instability in hybrid rockets,” NASA contract NAS 1-7310, 1969.
- [72] Y. Sivathanu and G. Faeth, “Generalized state relationship for scalar properties in non-premixed hydrocarbon/air flames,” *Combustion and Flame*, vol. 82, no. 2, pp. 211-230, 1990.
- [73] W. Jones and J. Whitelaw, “Calculation methods for reacting turbulent flows: a review,” *Combustion and Flame*, vol. 48, pp. 1-26, 1982.

- [74] M. Hazewinkel, "Beta-distribution," in *Encyclopedia of Mathematics*, Springer, 2001.
- [75] P. Roache, *Verification and validation in computational science and engineering*, Albuquerque, New Mexico: Hermosa Publishers, 1998.
- [76] M. Chiaverini, "Review of solid fuel regression," in *Fundamentals of hybrid rocket combustion and propulsion*, vol. 218, K. Kuo and M. Chiaverini, Eds., Progress in Astronautics and Aeronautics, AIAA, 2007, pp. 49-93.
- [77] G. Lengellé, "Solid-Fuel Pyrolysis Phenomena and Regression Rate, Part 1: Mechanisms," in *Fundamentals of hybrid rocket combustion and propulsion*, vol. 218, K. Kuo and M. Chiaverini, Eds., Progress in Astronautics and Aeronautics, AIAA, 2007, pp. 127-163.
- [78] J. de Wilde, "The heat of gasification of polyethylene and polymethylmethacrylate," Rept. PML 1988-C42, Delft, 1988.
- [79] A. Karabeyoglu, B. Cantwell and J. Stevens, "Evaluation of homologous series of normal-alkanes as hybrid rocket fuels," in *41st AIAA/ASME/SAE/ASEE Joint Propulsion Conference & Exhibit*, Tucson, Arizona, 2005.
- [80] S. Whitmore, J. Wilson, M. Ritter and L. Williams, "Estimating the enthalpy of gasification of Acrylonitrile-Butadiene-Styrene hybrid rocket fuels," *Journal of Propulsion and Power*, vol. 31, no. 4, pp. 1033-1040, 2015.
- [81] M. Karabeyoglu, B. Cantwell and G. Zilliac, "Development of scalable space-time averaged regression rate expressions for hybrid rockets," *Journal of Propulsion and Power*, vol. 23, no. 4, pp. 737-747, 2007.
- [82] G. Abramovich, *The Theory of Turbulent Jets*, Cambridge, MA: Massachusetts Inst. of Technology Press, 1963.
- [83] D. Pastrone, L. Casalino and C. Carmicino, "Analysis of acoustics and vortex shedding interactions in hybrid rocket motors," *Journal of Propulsion and Power*, vol. 30, no. 6, pp. 1613-1619, 2014.

- [84] D. Singh and C. Jachimowski, "Quasiglobal Reaction Model for Ethylene Combustion," *AIAA Journal*, vol. 32, no. 1, pp. 213-216, 1994.
- [85] M. Karabeyoglu and D. Altman, "Dynamic modeling of hybrid rocket combustion," *Journal of Propulsion and Power*, vol. 15, no. 4, pp. 562-571, 1999.